USING FLUORESCENT CARBON DOTS FOR BIOSENSING APPLICATIONS OF AMINO ACIDS

A Thesis Submitted to the Committee on Graduate Studies

in Partial Fulfillment of the Requirements for the Degree of Master

Science in the Faculty of Arts and Science

TRENT UNIVERSITY

Peterborough, Ontario, Canada

Environmental and Life Sciences M.Sc. Graduate Program

September 2022

ABSTRACT

Using Fluorescent Carbon Dots for Biosensing Applications of Amino Acids

Nayomi S. Camilus

Amino acids make up proteins, which are the building blocks of life. A balance of amino acids is needed to maintain a healthy state. Tyrosine (Tyr) is synthesized from the metabolism of phenylalanine, which is an essential amino acid, meaning it can only be obtained from the diet. It is related to many metabolic and neurodegenerative diseases. Tyr can undergo post-translational modifications such as phosphorylation and nitration, which are implicated in cancer and nitrative stress, respectively. Although there are many methods to detect Tyr and its analogues, phosphotyrosine (pTyr) and nitrotyrosine (nTyr), these methods are time-consuming, involve expensive instruments and involve tedious process. This research proposes a new type of nanomaterials, carbon dots (CDs), to detect these amnio acids. Data indicate that CDs can be used to detect nTyr with a limit of detection of 34 μM in the linear range of 20 - 105 μM. The amenability of CD-nTyr assay was also tested in various biological matrices and biological molecules and was shown to be sensitive to nTyr. Nitration of Tyr was carried out in the presence of sodium nitrite and hydrogen peroxide catalyzed by either Cu(II) or Fe(III) to mimic biological reactions and CDs were tested as both inhibitors and indicators of Tyr nitration. Although CDs did not inhibit the nitration reaction of Tyr, they did not serve as indicators of Tyr nitration due to the quenching of CDs by the nitrating agents. This shows the importance of using CDs to detect nTyr and further use it for biological applications to detect diseased states.

Acknowledgements

The completion of my thesis would not have been possible without the immense support and guidance I received from those around me.

First off, I would like to thank my supervisor, Dr. Sanela Martic, for giving me the opportunity to conduct research under her supervision and for her tremendous support throughout this process. Her dedication to providing her students with both knowledge, experience and constructive feedback is greatly appreciated.

Next, I would like to acknowledge and thank my supervisory committee members, Dr. Andrew Vreugdenhil and Dr. Janet Yee, for their support and valuable feedback in accomplishing the research objectives of my thesis. I would like to thank them for their time and effort in reviewing my work.

I would also like to thank Dr. Rafik Naccache for providing us with carbon dots and for the Naccache Lab at Concordia University for their collaboration in this project.

I would also like to thank the members of the Martic Lab for their valuable comments and suggestions on my work during lab meetings.

Lastly, I would like to thank my family and friends for encouraging me along the way.

Table of Contents

List of Figures

List of Tables

List of Abbreviations

2-AET 2-aminoethanethiol

AAs Amino acids

AB acetylene black

ACN acetonitrile

AD Alzheimer's Disease

Al-CuSe-NPs Aluminium doped copper selenide nanoparticles

ALS amyotrophic lateral sclerosis

AMWCNT@GONRs multiwall carbon nanotube at graphene oxide nanoribbons

AMP Adenosine monophosphate

ATP Adenosine 5′-triphosphate

ATR attenuated total reflection

AuNCs gold nanoclusters

AuNPs gold nanoparticles

AuNPs/PEBT/GCE gold-nanoparticles/poly-eriochrome black T film modified glassy carbon electrode

AuNPs/poly-TrB/GCE gold-nanoparticles/poly-Trypan Blue modified glassy carbon electrode

BI-Fe/Pd imprinted bimetallic Fe/Pd

Bpy Bipyridine (bpy)

BMIP@CDs bio-inspired molecularly imprinted polymer as a receptor and green emitting CDs as a signal transducer

c-Abl non-receptor tyrosine kinase Abelson

CAD coronary artery disease

cAuNPs cubic gold nanoparticles

$CdWO_4$ cadmium tungstate nanodots decorated with reduced graphene oxide

$CdWO_4$ ND@RGO cadmium tungstate nanodots decorated with reduced graphene oxide

nanocomposite

CCE carbon ceramic electrode

CDs carbon dots

CNDs carbon nanodots

CO_2 carbon dioxide

COOH carboxyl group

$CuFe_2O_4$ copper ferrite nanodots

CuO-NPs copper oxide nanoparticles

CuO/β-CD cupric oxide decorated on β-cyclodextrin

CV cyclic voltammetry

CQDs carbon quantum dots

DAD diode array detection

Di-ePAD dual-imprinted electrochemical paper-based analytical device

DPID 2-(3,4-dihydroxyphenethyl)isoindoline-1,3-dione

DNA Deoxyribonucleic acid

DOX doxorubicin

ECD electrochemical detection

EDTA Ethylenediamine tetraacetic acid

E_g energy gap

ELISA enzyme-linked immunosorbent assay

Fe$_3$O$_4$NP-ZnO/ZnHCF magnetic nanoparticles-zinc oxide/zinc hexacyanoferrate

FEs filtered electrodes

FT-IR Fourier-transform infrared spectroscopy

FRET fluorescence resonance energy transfer

GC gas chromatography

GCE glassy carbon electrode

GC-MS Gas Chromatography Mass Spectrometry

GC-MS/MS gas chromatography-tandem mass spectrometry

G-CQDs green carbon quantum dots

GQDs graphene quantum dots

HD Huntington's disease

HGN hemin modified graphene nanosheet

HOMO highest occupied molecular orbital

HPLC high performance liquid chromatography

HPLC-EC High Performance Liquid Chromatography with Electrochemical Detection

HPLC-UV high performance liquid chromatography with ultraviolet detection

ICT intermolecular charge transfer

K$_b$ binding constant

K$_d$ dynamic constant

K$_q$ quenching rate constant

K$_s$ static constant

K$_{sv}$ Stern-Volmer constant

LC-MS liquid chromatography-mass spectrometry

LC-MS/MS liquid chromatography-tandem mass spectrometry

L-Cys/CdTe QDs L-cysteine-capped CdTe quantum dots

LED light-emitting diode

LOD limit of detection

LOQ limit of quantitation

LUMO lowest unoccupied molecular orbital

MES 2-(N-morpholino)ethanesulfonic acid

MIPs molecularly imprinted polymers

MS mass spectrometry

MSPE multi-conventional screen-printed carbon electrode

MSPs mesoporous silica nanoparticles

MW-FEs filtered multi-walled carbon nanotubes

MWNTs multiwall carbon nanotubes

n-CPE nanoparticle-modified carbon paste electrode

NH$_2$ amino group

NO$_2$ nitro group

nTyr Nitrotyrosine

PAMAM/MWCNT immobilization of hemin onto the poly (amidoamine)/multi-walled carbon nanotube

PCNA proliferating cell nuclear antigen

PD Parkinson's disease

Pea pyrazinecarboxylic acid

PEI poly-ethylenimine

PET photoinduced electron transfer

pTyr phosphotyrosine

RGO reduced graphene oxide

RNA ribonucleic acid

SiO$_2$@AgNPs silica nanosphere decorated with silver nanoparticles

SPCE screen printed carbon electrode

SWCNT single-walled carbon nanotubes

SWSV square wave stripping voltammetry

TEM Transmission electron microscopy

TBAF tetrabutylammonium hexafluorophosphate

TiO$_2$-GR TiO2-graphene

Tyr Tyrosine

UCNPs upconversion nanoparticles

UT Ultrathin

UV/VIS ultraviolet-visible

Wt% weight percent

XRD powder X-ray diffraction

XTT xurography-enabled thermally transferred

ZIF-8 zeolitic imidazolate framework

ZrO$_2$ zirconium dioxide

ZrO$_2$@rGO NCs zirconium dioxide sheathed reduced graphene oxide nanocomposites

Chapter 1 - Introduction

1.1 Importance of studying amino acids

Amino acids (AAs) are made up of three functional groups: amino group (NH_2), carboxylic group (COOH), and a variable side chain. The variable side chain gives unique properties to the amino acid making it either charged, hydrophobic, or polar but uncharged. Through the formation of the peptide bonds, AAs make up proteins, which are the building blocks of life, and the side chains provide the protein its tertiary structure (Figure 1.1) [1]. There are 20 AAs found in the human body, with 9 of them being essential ones. Essential amino acids are those that cannot be synthesized endogenously and must be obtained in the diet whereas non-essential amino acids are synthesized endogenously. The availability of AAs play an important role in the synthesis and catabolism of proteins which has an influence on the functions of the cell like in regulation of cell signaling, gene expression, transport and the metabolism of the AAs [2]. An increase in AAs leads to increased protein synthesis and prevents the degradation of proteins while a decrease in AAs leads to the breakdown of proteins and in extreme cases of starvation, conversion into glucose and ketone bodies [2].

1.1.1 Tyrosine (Tyr)

Tyrosine (Tyr) is a semi-essential aromatic amino acid that is synthesized from phenylalanine and can easily pass through the blood brain barrier. Semi-essential amino acids are those that are synthesized by an essential amino acid; tyrosine is considered a semi-essential amino acid because it is synthesized by the metabolism of phenylalanine, which is an essential amino acid. It comprises 1-6% of the weight of most proteins [3].

Precursors of dopamine are epinephrine and norepinephrine, which are dependent on dietary tyrosine [4,5]. Tyr is found in low concentrations in the body because of its high metabolization rate. In addition, Tyr is a significant amino acid, meaning that it is involved in the biosynthesis of peptides, proteins, and painkillers and is a precursor of hormones and melanin (Figure 1.1). Since Tyr is involved in many important systems in the body, an imbalance of this amino acid leads to metabolic disorders such as tyrosinemia [6,7], alkaptonuria, and albinism and mental disorders like depression. Tyrosinemeia affects 1 in 100,000 people and is a rare autosomal recessive disorder as a result of the deficiency of the enzyme, fumarylacetoacetate hydrolase [8]. The role of Tyr in biological systems makes its detection and quantification one of importance.
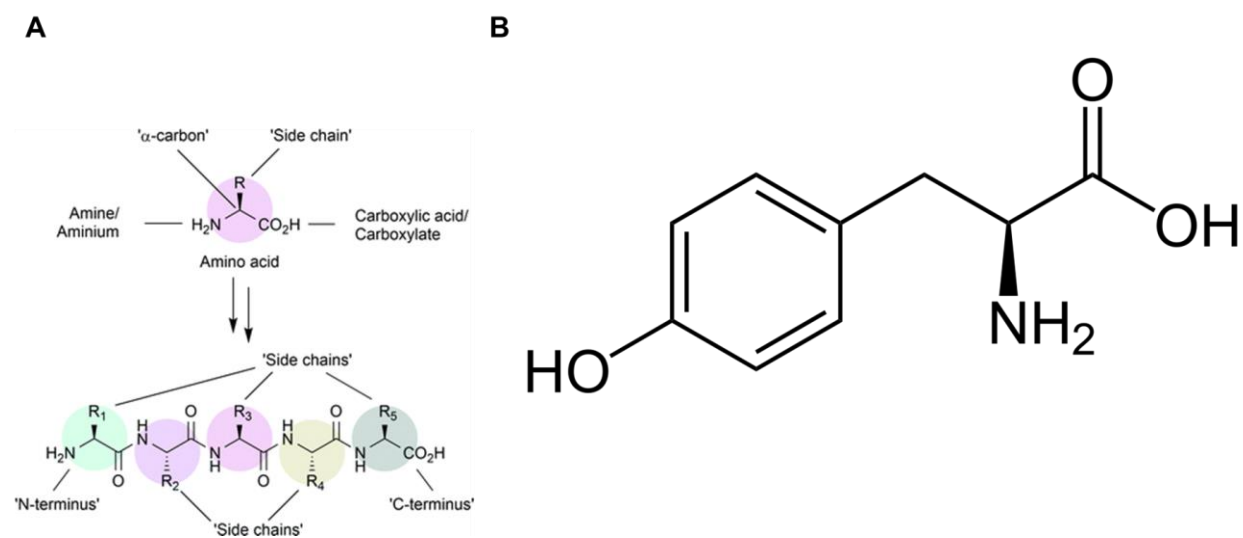
Figure 1.1. (A) Basic structure of amino acid and peptide [9]; (B) Structure of Tyr.

1.2 Post-translational modifications of Tyr

Post-translational modifications such as phosphorylation and nitration of proteins play an important role in cell signaling and are the pathway of diseases. There are two types of post-translational modifications; the first type consists of proteolytic processes like the cleavage of peptide fragments while the second type consists of modifications to the side

chains of AA [10]. Tyr residues undergo various post-translational modifications with the three major ones being phosphorylation, nitration and sulfation (Figure 1.2) [10].The other modifications of Tyr include oxidation, halogenation, AMPlyation, and glycosylation [11]. These modifications result in a variety of different types of biological molecules from tri-peptides (Met-Tyr-Trp) to quinones (topaquinone) [11]. Consequently, these modifications play a significant role in physiological and pathological processes.
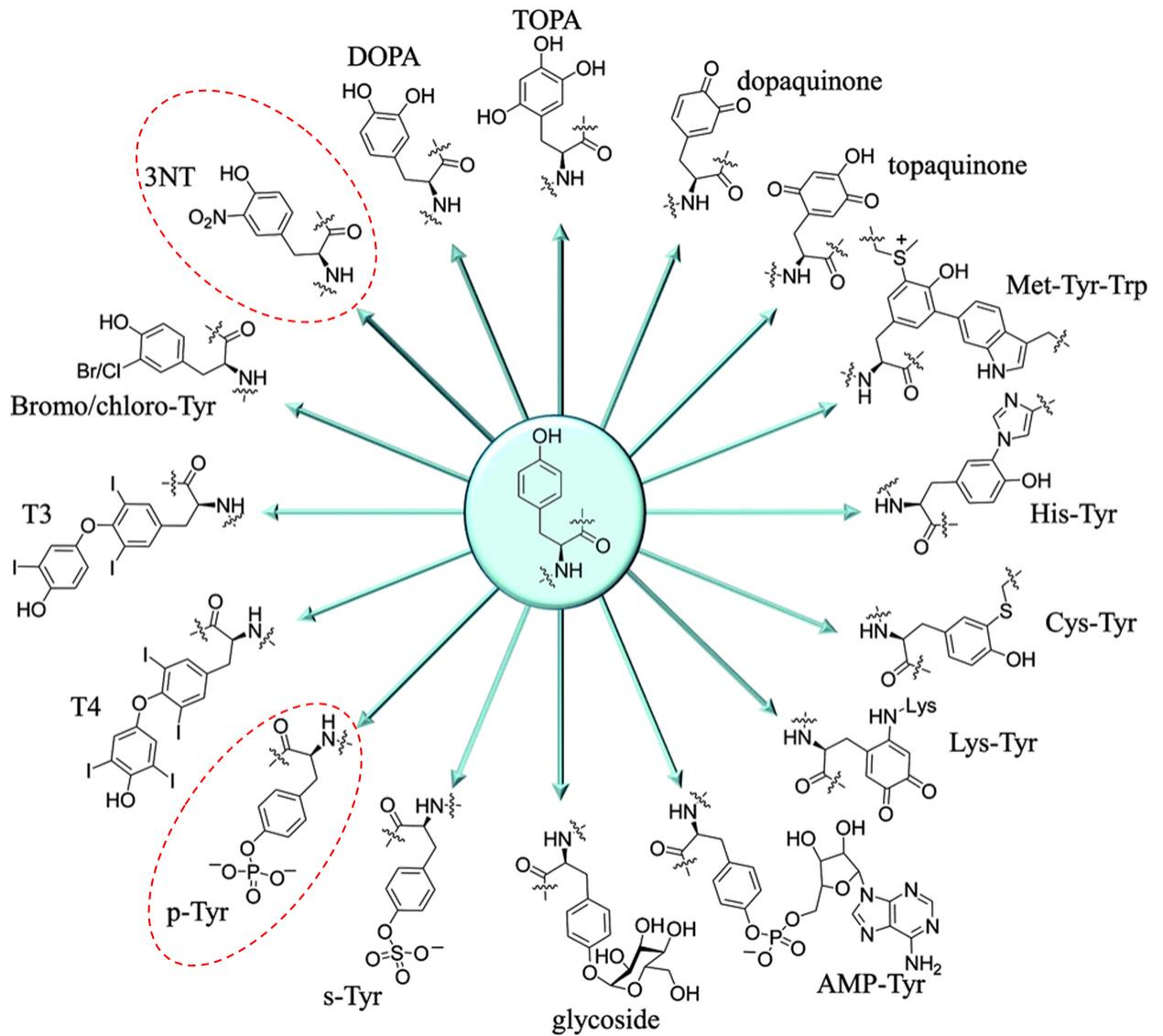
Figure 1.2. Post-translational modifications of Tyr [11].

1.2.1 Phosphorylation of Tyr

Phosphorylation, a post-translational modification, is a reversible process in which Adenosine 5′-triphosphate (ATP) donates a phosphate group to the polar group of amino acids through ATP hydrolysis. Phosphorylation of hydroxyl containing amino acids, including tyrosine, play an important role in cell signaling [12]. Specifically, proliferating cell nuclear antigen (PCNA), a protein involved in cell proliferation, gets phosphorylated at Tyr 211 through Ron, a tyrosine kinase that activates non-receptor tyrosine kinase Abelson (c-Abl) [13]. In addition, phosphorylation of tau protein makes it harder for neuronal transport as it is harder for tau to attach to the microtubules [14]. The phosphorylation of tau at Tyr 394 changes the shape of the protein. Moreover, phosphorylation of tyr18 in tau by fyn, a tyrosine kinase, is implicated in Alzheimer's diseases [15].

1.2.2 Nitration of Tyr

Nitration of tyrosine is a covalent modification that adds a nitro group ($-NO_2$) to one of the *ortho* groups of benzene by nitrating species like nitrogen dioxide [16]. Nitration of tyrosine residues such as 3-nitrotyrosine (nTyr), are known to play a role in neurodegenerative disease like Alzheimer's disease where the protein, amyloid beta, is nitrated at tyrosine 10, resulting in both *in vivo* and *in vitro* aggregation [17,18]. The presence of nTyr is also indicative of oxidative stress and tissue damage, being implicated in cardiovascular diseases like coronary artery disease (CAD). Specifically, the plasma of individuals with CAD were found to have elevated nTyr compared to normal patients [19]. Moreover, nTyr is shown to be elevated in patients with mild asthma who are not

undergoing corticosteroid therapy but nTyr levels are reduced in those receiving therapy [20].

1.3 Detection methods for Tyr and its analogues

There are many methods of detecting free Tyr and its analogues, pTyr and nTyr with each method having its drawbacks. To detect Tyr, most studies have used electrochemical methods [21]. The use of electrochemistry to detect Tyr dates back to the 1980s, when the electro-oxidizable property of Tyr residues at carbon electrodes was discovered[22] [23]. This involves both two electron and two proton transfers [24]. The other methods of detecting Tyr are high performance liquid chromatography (HPLC), fluorescence [25], fluorimetry and liquid chromatography-mass spectrometry (LC-MS) [26]. These methods have provided good results but have several limitations such as a complex treatment process, a time-consuming process and the consumption of reagents. Only a few studies have detected pTyr but in peptides and not as a free amino acid [27–29].

For the detection of nTyr, a variety of methods have been used from immunochemical methods to mass spectroscopic methods (Figure 1.3) [30,31]. The study of protein tyrosine nitration dates back to 1992 by Joseph Beckman who developed antibodies that recognized nitrated proteins [30]. Then in 1995, the first analytical technique, high performance liquid chromatography with ultraviolet detection (HPLC-UV), to quantify levels of free nTyr in serum and synovial fluid of patients with rheumatoid arthritis was developed by Barry Halliwell's group. A review of 285 references for detecting nTyr, published in 2001, found that 66% of studies used immunohistochemistry and 4% used a combination of both immunological and analytical methods [30]. Out of the

5

66% of studies that used immunohistochemistry, 13% used western blot, 3% enzyme-linked immunosorbent assay (ELISA), 2% immunoprecipitation followed by western blot, 11% High Performance Liquid Chromatography with Electrochemical Detection (HPLC-EC), 3% HPLC-UV and 2% Gas Chromatography Mass Spectrometry (GC-MS). This review found that there were discrepancies between the reported values of nitrated protein in studies using a combination of both techniques. However, the best strategy is still to use a combination of both methods as they provide information on the location, specific protein and magnitude of nitration [30].
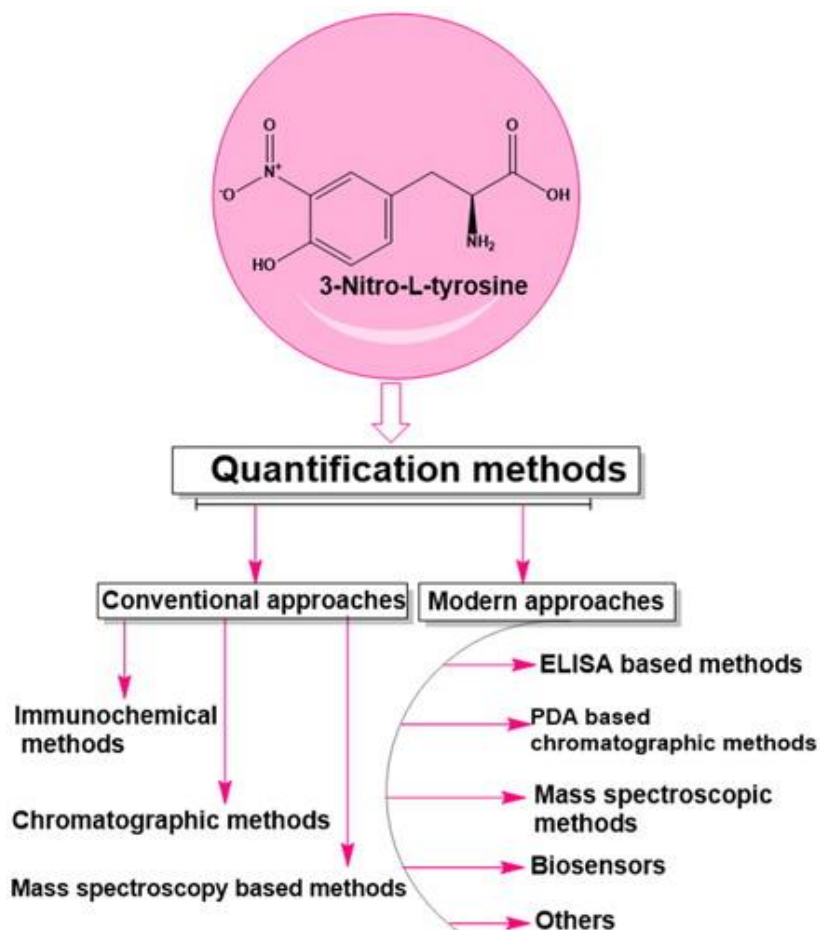
Figure 1.3. Scheme of detection methods for nTyr [31].

1.3.1 Traditional analytical methods

The traditional methods of detecting nTyr can be separated into three groups: (1) immunological methods; (2) liquid chromatography, such as HPLC-based methods that use ultraviolet-visible (UV/VIS) absorption, electrochemical (ECD) and diode array (DAD) detection, LC-MS and liquid chromatography-tandem mass spectrometry (LC-MS/MS); and (3) gas chromatography, such as GC-MS and gas chromatography-tandem mass spectrometry (GC-MS/MS) [32]. The traditional method of detecting nTyr in biological samples was LC-MS/MS, which was believed to provide greater specificity and sensitivity when compared to GC-MS/MS, which requires volatilization [31]. Over time, MS has become the analytical method of choice for the mapping of peptides and nitropeptides [31]. Immunological methods like ELISA are straight-forward and are the least time-consuming; however, they do not provide accurate results [32]. HPLC methods do not require a derivatization step due to nTyr's chemical properties whereas GC-based methods require it before analysis, which becomes a time-consuming method [32]. However, GC-based methods provide the highest sensibility while HPLC is not considered to provide accurate results [32]. Although these methods of detection were able to quantify Tyr and its analogues, an alternative method is required in order to overcome the challenges of costly instruments, time constraints, and low sensitivity.

1.3.2 Alternative method of detection: use of nanomaterials

Nanomaterials have received great attention over the last century in many different fields (Figure 1.4). They can range from zero-dimensional to three-dimensional and measure less than 100 nm in size [33]. Nanomaterials are categorized into different types based on how they are made, their size and their make-up: carbon-based nanomaterials,

7

metal-based nanomaterials, lipid-based nanomaterials, semiconductor nanomaterials and polymeric nanomaterials [33]. They are synthesized using biological, chemical or physical methods with the biological method being the most convenient and eco-friendly one [34]. The synthesis of nanomaterial uses two different approaches: top-down and bottom-up. The top-down approach involves using the bulk material to divide it into nanomaterials whereas the bottom up involves starting with the molecular and atomic level and working towards the production of nanoparticles [35].

There are many advantageous applications of nanomaterials in sensors, catalysis, and environmental monitoring (Figure 1.1) [36]. Graphdiyne, a two-dimensional material, has been used to detect amino acids (glycine, glutamic acid, histidine and phenylalanine) through the changes in electronic conductivity of the material, making it useful as biosensors [37].
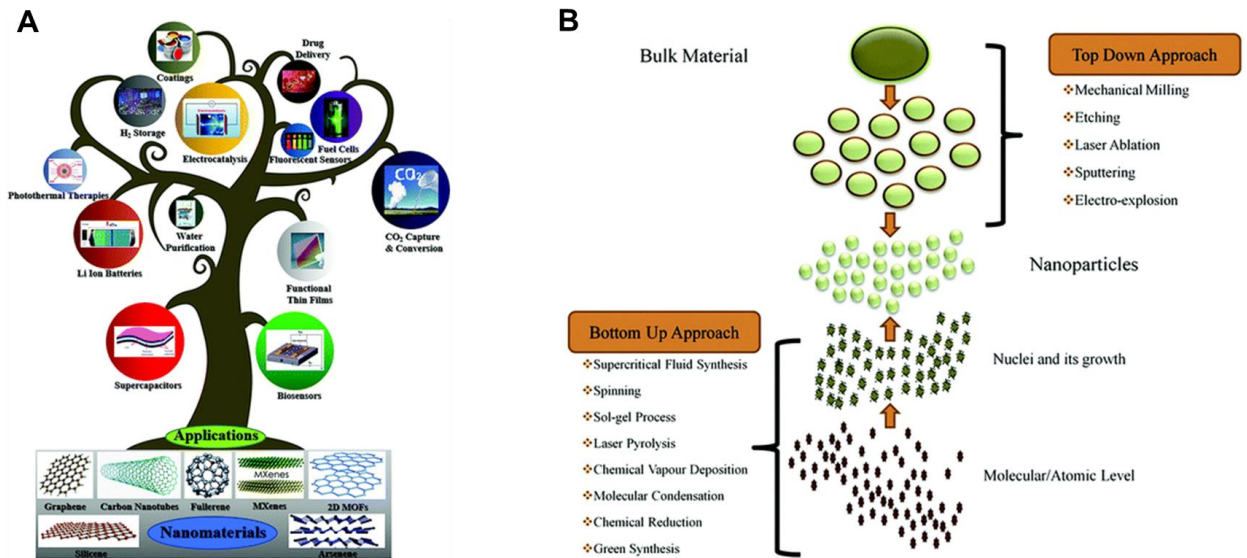
Figure 1.4. (A) Diagram of the application of nanomaterials; (B) diagram outlining the synthesis of nanomaterials using either the top down or bottom-up approach [35].

1.3.2.1 Carbon dots (CDs)

CDs are a new class of carbon-based nanomaterials that are zero-dimensional, and they measure below 10 nm in size. Xu et al. discovered CDs by chance when they were purifying single-walled carbon nanotubes (SWCNT) by electrophoresis [38]. The synthesis and characterization of CDs has been greatly explored in the last decade [39]. Since 2008 to 2018, the number of publications related to CDs and their advantageous properties have rapidly increased from only 528 in 2008 to more than 5000 in 2018. CDs have gotten attention due to the low cost associated with their synthesis and their easy preparation. These fluorescent nanoparticles are synthesized either by the breakdown of large carbon raw materials (carbon soot [40], carbon fiber [41], activated carbon [42], carbon black [43] and graphene [44]) or by the synthesis of materials containing carbon (citric acid [45–47], polyols [48] and amino acids [49]) (Figure 1.5). CDs are composed of sp^2 hybridized carbon atoms along with oxygen, nitrogen and other heteroatoms [50,51] and do not have a perfect crystal structure [40,52–54]. There are three different types of CDs: graphene quantum dots (GQDs), carbon nanodots (CNDs), and carbon quantum dots (CQDs). These three types of CDs differ in their structure. GQDs are disc-shaped; CNDs are amorphous quasi-sphere; and lastly CQDs are spherical and crystal in structure [55]. There are inter sp^2-hybridized carbon atoms in the core of CDs, with many functional groups on their surface such as amino, epoxy, ether, carbonyl, hydroxyl, and carboxylate [56]. The conjugated π bonds and surface defects of CDs influence their conductivity, optical properties, and catalytic activity [57]. In addition, CDs have excitation-wavelength-dependent emission properties in which the emission wavelength redshifts and the emission intensity decreases as excitation wavelength increases. CDs are water soluble due to the

rich hydrophilic groups on their surfaces. They can be easily functionalized through derivatization with recognition molecules like antibodies and aptamers due to their surface residues of carboxyl and amino groups. When compared to metal fluorescent nanomaterials like gold nanodots, CDs possess a greater brightness and stability [58]. CDs are more biocompatible as they can be synthesized from wealthy organic compounds whereas quantum dots are prepared from semiconductor materials [59]. Quantum dots made from semiconductor materials are known to photoblinking and photobleaching but this is not seen in CDs [39]. Moreover, CDs can be modified in their synthesis to get desirable optical properties like an enhancement of their red emission intensity and quantum yields [60]. The tuning of CDs can be achieved through control of their core and surface structures and doping with heterogeneous atoms like nitrogen [60]. CDs are also catalytic and are able to catalyze many reactions like water-splitting [61–63], cyclohexane oxidation [64], and CO_2 reduction [65]. These unique properties of CDs allow them to be used in biological applications.

Due to the advantageous properties of CDs, they have been widely used in sensing applications, drug delivery and bioimaging. They have desirable properties such as optical properties, low toxicity, and high biocompatibility [66]. They are used in sensing applications for the detection of ions, biological pH value, protein and enzymes, vitamins, and nucleic acid, etc. [67].The use of CDs in quantifying metals provides a better approach than the traditional methods of atomic absorption and emission, auger-electron, absorption in the ultraviolet-visible region [68]. Mercury ions were detected using CDs synthesized by household flour with a low LOD of 0.5 nM in the linear range of 0.0005–0.01 μM [68]. In the presence of mercury ions, the fluorescence of the CDs was quenched [68]. Not only

have CDs been used to detect metal ions, but they have also been used to sense chemical compounds like flavonoids. One type of flavonoid, quercetin, was detected using CDs made from 1-butyl-3-methylimidazolium tetrafluoroborate with a LOD of 9.88×10^{-8} mol L^{-1} in the linear range of 2.87×10^{-6} to 31.57×10^{-6} mol L^{-1} [69]. CDs made from a one-step microwave assisted-reaction using formamide and glutathione have been used to monitor temperatures in the range of 5–60 °C with a thermal resolution of 0.048 K^{-1} and thermal sensitivity of 1.97% C^{-1} [69]. These CDs were also able to sense pH changes in living cells in a ratiometric manner [69].

In addition to applications in sensing, CDs are used in drug delivery. One particular study used CDs synthesized by harmful cyanobacteria for cell imaging and anticancer drug delivery [70]. The use of CDs as tags for this application was able to deliver doxorubicin (DOX) to the targeted cancer cells and allow for the sensing of the cells through the fluorescence activation of the cells for imaging [70]. Another study used luminescent CDs as caps on the surface of mesoporous silica nanoparticles (MSPs) to deliver drugs on-demand and image cells both *in vitro* and *in vivo* [71]. The CDs contained many carboxylic acid groups on the surface which allowed them to serve as gates for the release of DOX, incorporated into MSP, when the pH changes [71]. The use of CDs in drug applications provide incredible advantages in cancer and have been widely used.

Lastly, CDs have been used for bioimaging, which allow for the visualization of different cellular components pf cells. One particular study used near-infrared emissive CDs made from glutathione and formamide to visualize human breast cancer cell lines under a confocal imaging technique. Once the CDs were incubated with the cells, deep-red emission was observed [72]. Thus, the CDs are considered to be both one-photon and two-

11

photon bioimaging agents [72]. In conclusion, the properties of CDs make them suitable for use in biosensing, drug delivery and bioimaging.
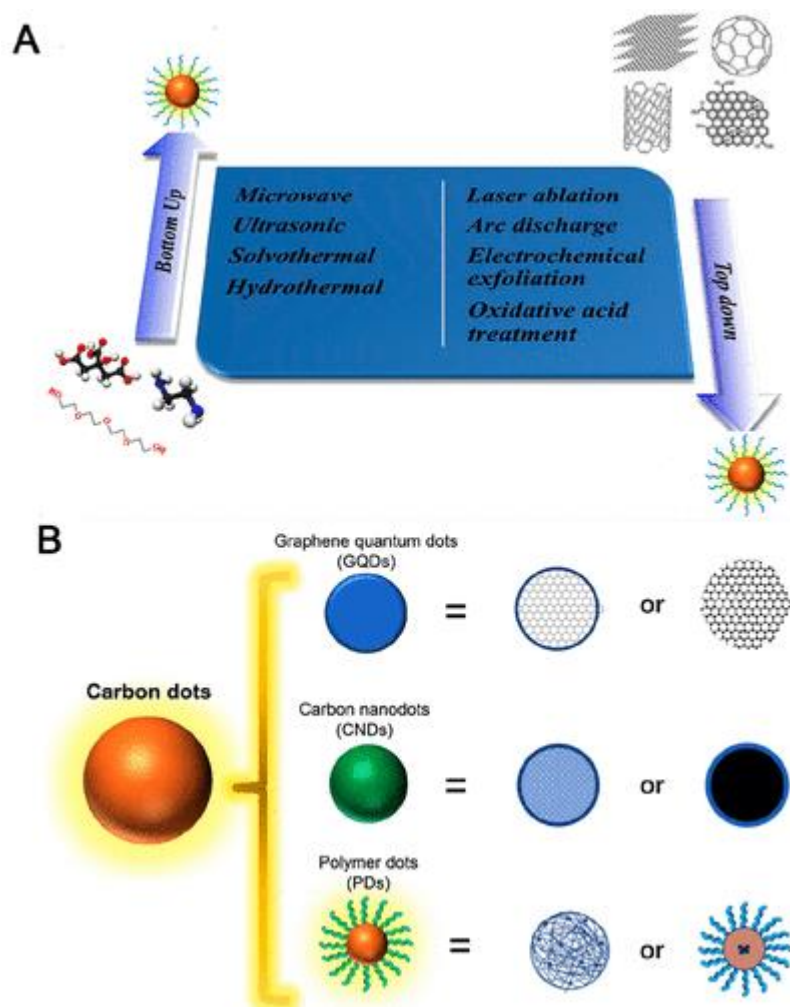
Figure 1.5. (A) Scheme of CD synthesis; (B) scheme of the three types of CDs [55].

1.3.3.2 Detection of Tyr and its analogues using nanomaterials

Various methods have incorporated the use of nanomaterials in sensing Tyr and its analogues, pTyr and nTyr. These methods can be divided into two main groups: electrochemical methods and optical methods.

1.3.3.3 Nanomaterial-based electrochemical sensors

Since Tyr is an electroactive amino acid, electrochemistry has been widely used for its detection [73]. Electrochemical sensors use voltammetric or amperometric techniques to detect small metabolites like Tyr and its analogues. They can be divided into two categories of sensors using the method: direct or indirect (Figure 1.6) [74]. The direct method involves using the redox reactions of the analyte of interest at a given applied potential without any receptors on the electrode [74]. This allows for a simple method of determining the concentration of the analyte. However, this method has its disadvantages because it is only limited to analytes that can carry out oxidation and reduction and when it comes to selectivity, there is interference by other redox molecules. The indirect method involves the use of receptors on the electrode and can be further classified into three groups: electrocatalytic, aptamer, and molecularly imprinted polymers (MIPs) [74]. Electrocatalytic biosensors use the electrocatalytic activity between the enzyme and substrate to detect the resulting electroactive species, quantifying through amperometric or voltammetric techniques [75]. Aptamers are single stranded DNA or RNA molecules; aptamer-based sensors use their unique ability to bind the analytes and are placed on the receptors, increasing its sensitivity [76]. Lastly, MIPs are artificial receptors created by polymerizing a monomer with its template (analyte) and then extracting the template. This creates binding spots that are available for the analyte to bind on the receptor [77].
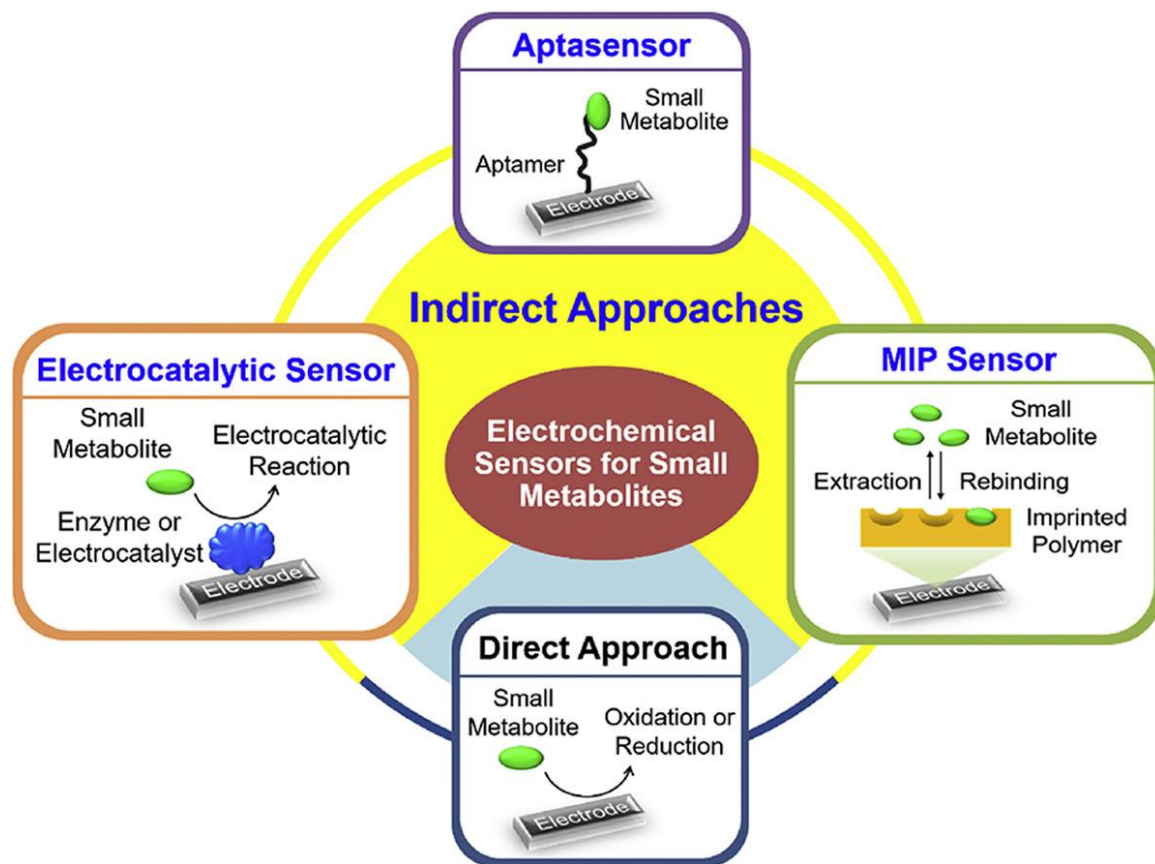
Figure 1.6. Scheme of electrochemical sensors for detection of small metabolites like Tyr and its analogues [74].

Incorporating nanomaterials into these different types of electrochemical sensors have greatly influenced the sensitivity of detecting Tyr and its analogues and provided many advantages. Table 1.1 shows the different nanomaterial-based electrochemical sensors used to detect Tyr and its analogues. There are many different combinations of nanomaterials that are used with low detection limits. The use of MIP provides a high surface-to-volume ratio, increasing the number of binding sites available for the analyte to bind. One study used MIP/reduced graphene oxide (RGO) composite in order to detect tyrosine and uric acid at the same time with a limit of detection of $0.046\,\mu M$ and $0.0032\,\mu M$, respectively [78]. This sensor was also selective to the two analytes as tested

in human serum and urine [78]. The use of MIP along with the RGO nanosheet as an electrode increased electron transfer rate, increased the available binding sites on the sensor and increased the specific surface area [78]. Similarly, MIPs have also been used in combination with gold nanoparticles to detect nTyr, One study used an electropolymerized pyrrole MIP doped with gold nanoparticles (AuNPs) on a glassy carbon electrode (GCE), modified with activated multiwall carbon nanotube at graphene oxide nanoribbons (AMWCNT@GONRs) to detect nTyr with a limit of detection of 50.0 nM [79]. The use of MIP with nanosheets allowed for selective binding sites with greater catalytic and electron migration ability. This sensor used square wave stripping voltammetry (SWSV) techniques to quantify nTyr and was able to detect nTyr in human blood serum and urine samples. The MIP sensor was also more advantageous than using HPLC as it was very time efficient (only 4 min compared to 50 min with HPLC), low costs and reproducible. The use of AuNPs into the polymer composite mediated the charge transfer process effectively. The polymer composite allowed for sensitive detection, selective behaviour towards nTyr, and good stability.

Another common technique of sensing Tyr and its analogues is to modify the commonly used electrode, glassy carbon electrode with nanoparticles like carbon nanotubes. This modification of the bare carbon electrode by nanomaterials allows for improved sensitivity due to its unique electronic and mechanical properties [74]. Many studies have modified electrodes, either the glassy carbon electrode, graphite pencil electrode, carbon paste electrode, carbon ceramic electrode or screen-printed carbon electrodes with either graphene, carbon nanofibers, nanoparticles or carbon nanotubes in order to detect Tyr [80–105]. These studies have shown improved sensitivity in detecting

Tyr down to the nM range. Similarly, electrodes have been modified by nanomaterials in order to detect nTyr (Figure 1.7). One study modified the electrode with copper ferrite nanodots ($CuFe_2O_4$) entrapped by porous RGO nanosheets (Figure 1.4D) [106]. The use of this multi-conventional screen-printed carbon electrode (MSPE) with nanomaterials provided great sensitivity (LOD = 25.14 pM) and high selectivity in detecting nTyr in neutral pH solutions and was also applied to human serum and urine samples [106]. The methods used were cyclic voltammetry (CV) and amperometry. The nanocomposite ($CuFe_2O_4$ and RGO) was able to improve the electrocatalytic activity of nTyr, provided good conductivity and increased surface area [106]. Another study used a dual-imprinted electrochemical paper-based analytical device (Di-ePAD), modified by MIP consisting of silica nanosphere decorated with silver nanoparticles (SiO_2@AgNPs) as a core covered with dual-analyte imprinted sites on the polymer to detect nTyr and 8-hydroxy-2′-deoxyguanosine; the limit of detection was 0.0027 μM in the linear range of 0.01–500 μM [107]. SiO_2@AgNPs were used to imprint the target molecules in order to increase surface/mass ratios, to have better solubilities, to increase easily accessible recognition sites and to improve binding capabilities of the target [107]. Using this nanomaterial-based electrochemical sensor provided the lowest detection limit for nTyr than other studies that have used zirconium dioxide (ZrO_2) sheathed reduced graphene oxide nanocomposites (ZrO_2@rGO NCs), imprinted bimetallic Fe/Pd (BI-Fe/Pd) nanoparticle modified pencil graphite electrode [108], AuNPs/MIP/AMWCNT@GONRs [79], and cadmium tungstate ($CdWO_4$) nanodots decorated with reduced graphene oxide nanocomposite ($CdWO_4$ ND@RGO) modified screen-printed electrode [109]. Modifying electrodes using

nanomaterials has greatly influenced the ability to detect Tyr and its analogues leading to improved sensitivity and high selectivity.
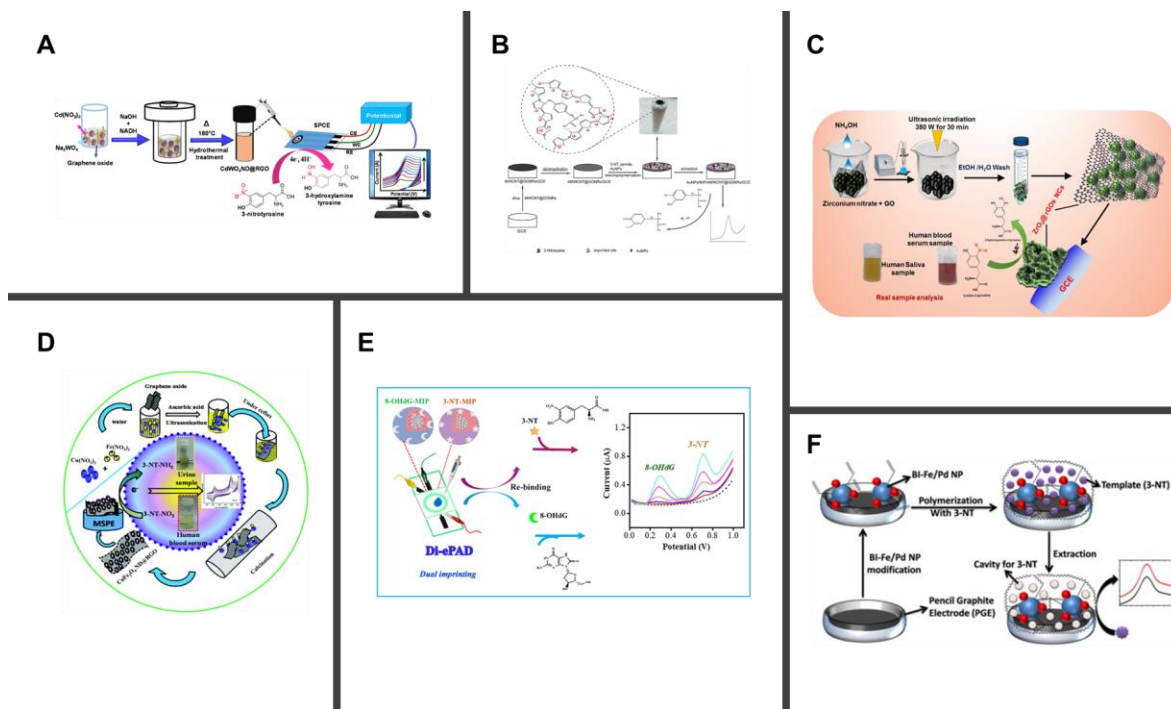
Figure 1.7. Scheme of nanomaterial-based electrochemical sensors for the detection of nTyr: (A) [109], (B) [79], (C) [110], (D) [106], (E) [107], (F) [108].

In addition, nanomaterials have been used as the electrode to measure Tyr. One study used carbon nanomaterial-based Teflon filtered electrodes (FEs) to detect Tyr with only 50 μL of sample in less than 1 min [111]. This was useful in detecting Tyr in the linear range of 25 to 750 μM with a LOD of 8 μM and in real life samples of blood and plasma. Similarly, electrochemical cells made from nanomaterials have been used to detect Tyr. One study used xurography-enabled thermally transferred (XTT) carbon nanomaterial-based electrochemical sensors to detect Tyr with a LOD of 0.1 μM in the linear range of 0.5–100 μM [112]. This sensor provided accurate quantification of Tyr in clinical samples with low errors [112]. A SWCNT-arrayed microelectrode chip was used to detect Tyr in

the linear range of 0.1 to 1 µM with a LOD 100 µM [113]. When compared to using a bare Pt microelectrode, the peak intensities with the SWCNT-arrayed microelectrode were 100 times higher [113]. In conclusion, the use of nanomaterials in electrochemical sensors has greatly improved the sensitivity of detecting Tyr.

Table 1.1. Nanomaterial-based electrochemical sensors for detecting Tyr and nTyr using electrochemistry.

Type of Nanomaterial	Analyte	Limit of detection (LOD)	Reference
polyoxometalate functionalized reduced graphene oxide (rGO) modified glassy carbon electrode (GCE)	Tyr	2.0×10^{-12} M	[88]
carboxylic acid functionalized multi-walled carbon nanotubes modified carbon paste electrode	Tyr	14.0 ± 1.36 nM	[80]
single-walled carbon nanotube (SWCNT)-arrayed microelectrode chip	Tyr	100 nM	[113]
carbon paste electrode modified with multi-walled carbon nanotubes	Tyr	1×10^{-7} M	[81]
xurography-enabled thermally transferred (XTT) carbon nanomaterial	Tyr	0.1 µM	[112]
molecularly imprinted polymer (MIP)/reduced graphene oxide (RGO) composite	Tyr	0.046 µM	[78]
glassy carbon electrode (GCE) modified with a film composed of Nafion and TiO_2-graphene (TiO_2-GR) nanocomposite	Tyr	2.3 µM	[82]
graphene-modified graphite pencil electrode	Tyr	0.07 µM	[87]
multiwall carbon nanotubes (MWNTs) film modified electrode	Tyr	3.5×10^{-7} mol L^{-1}	[90]
glassy carbon electrode that was modified with a composite made from graphene oxide (GO) and multiwalled carbon nanotubes (MWCNT)	Tyr	4.4 nM and 14.7 nM	[83]
a simple electroanalytical device based on filtered multi-walled carbon nanotubes (MW-FEs)	Tyr	8 µM	[111]
1D morphology (single walled CNTs)	Tyr	0.61 nM	[101]

Table 1.1 continued

along with tyrosinase as the bioreceptor			
multi-walled carbon nanotubes and poly (Bromocresol purple) modified carbon paste electrode	Tyr	1.91×10^{-7} M	[93]
copper oxide nanoparticles (CuO-NPs) at a carbon ceramic electrode (CCE)	Tyr	160 nM	[86]
Aluminium doped copper selenide nanoparticles (Al-CuSe-NPs), were used to modify screen printed carbon electrode (SPCE)	Tyr	0.04 μM	[89]
cubic gold nanoparticles (cAuNPs) involved in 2-aminoethanethiol (2-AET) functionalized graphene oxide (GO) modified glassy carbon (GC) electrode	Tyr	1.5×10^{-10} M	[84]
cupric oxide decorated on β-cyclodextrin (CuO/β-CD) nanocomposite modified glassy carbon electrode	Tyr	0.0082 μM	[102]
Au-nanoparticles/poly-eriochrome black T film modified glassy carbon electrode (AuNPs/PEBT/GCE)	Tyr	10 nM	[94]
Au-nanoparticles/poly-Trypan Blue modified glassy carbon electrode (AuNPs/poly-TrB/GCE)	Tyr	$0.008 \; \mu mol \; L^{-1}$	[96]
surface modification of a glassy carbon electrode (GCE) with Nafion and cerium dioxide nanoparticles	Tyr	~90 nM	[97]
magnetic nanoparticles-zinc oxide/zinc hexacyanoferrate (Fe3O4NP-ZnO/ZnHCF) hybrid film electrodeposited on the surface of a Pt electrode as working electrode	Tyr	4 μM	[98]
immobilization of hemin onto the poly (amidoamine)/multi-walled carbon nanotube (PAMAM/MWCNT) nanocomposite film modified glassy carbon electrode (GCE)	Tyr	0.01 μM	[99]

Table 1.1 continued

NiO/CNTs and (2-(3,4-dihydroxyphenethyl)isoindoline-1,3-dione) (DPID) modified carbon paste electrode	Tyr	1.0 μM	[103]
Fe-doped hydroxyapatite (Fe-HA) nanoparticles and tyrosinase modified glassy carbon electrode	Tyr	245 nM	[104]
hemin modified graphene nanosheet (HGN)	Tyr	7.5×10^{-8} M	[114]
single-walled carbon nanotubes (SWCNTs) modified glassy carbon electrode (GCE/SWCNTs)	Tyr	9.3×10^{-8} mol/L	[91]
cerium doped hydroxyapatite (Ce-HA) nanoparticles modified glassy carbon electrode	Tyr	0.072 μM	[115]
immobilization of tyrosine hydroxylase onto palladium-platinum bimetallic alloy nanoparticles/chitosan-1-ethyl-3-methylimidazolium bis(trifluoromethylsulfonyl) imide/graphene-multiwalled carbon nanotubes-IL/glassy carbon electrode	Tyr	0.009×10^{-9} mol L^{-1}	[100]
Ultrathin (UT) g-C_3N_4/Ag hybrids	Tyr	1.40×10^{-7} mol L^{-1}	[95]
Carbon nanofibers (CNFs) modified carbon paste electrode	Tyr	0.1 μM	[85]
copper nanoparticle-modified carbon paste electrode (n-CPE)	Tyr	0.77 μM	[92]
reduced graphene oxide (rGO) and acetylene black (AB)	Tyr	0.06 μM	[105]
electropolymerized pyrrole molecularly imprinted polymer (MIP) doped with gold nanoparticles (AuNPs) on a glassy carbon electrode (GCE) modified with activated multiwall carbon nanotube @ graphene oxide nanoribbons (AMWCNT@GONRs)	nTyr	50.0 nM	[79]

Table 1.1 continued

cadmium tungstate (CdWO$_4$) nanodots decorated reduced graphene oxide nanocomposite (CdWO$_4$ ND@RGO) modified screen-printed electrode	nTyr	3.24 nM	[109]
imprinted bimetallic Fe/Pd (BI-Fe/Pd) nanoparticle	nTyr	1.20 µg L^{-1} and 3.25 µg L^{-1}	[108]
silica nanosphere decorated with silver nanoparticles (SiO$_2$@AgNPs) as a core covered with dual-analyte imprinted sites	nTyr	0.0027 µM	[107]
zirconium dioxide (ZrO$_2$) sheathed reduced graphene oxide (ZrO$_2$@rGO NCs) nanocomposites	nTyr	9 nM	[110]
copper ferrite nanodots (CuFe$_2$O$_4$) entrapped by porous RGO nanosheets	nTyr	25.14 pM	[106]

1.3.3.2 Nanomaterial-based optical sensors

Extensive research has been done with nanomaterials-based electrochemical sensors to detect Tyr and nTyr. However, only a very limited number of studies have used nanomaterial-based optical sensors to detect Tyr and its analogues (Table 1.2). Optical sensors for detecting Tyr and its analogues involve the use of colour change or change of intensity of emitted light to quantify the analyte of interest through colourmetric and fluorescence readouts [116]. Nanomaterial-based optical sensors have mainly used fluorescence spectroscopy to detect Tyr and nTyr. Fluorescence spectroscopy provides an easy to use, most used and inexpensive technique in sensing applications. Carbon dots made from waste coconut coir (C-dots) have been used to detect Tyr at room temperature in the linear range of 1-100 nM with a LOD of 0.96 nM [117]. Compared to the twenty amino acids (aspartic acid, serine, alanine, glycine, leucine, isoleucine, proline, valine, phenylalanine, Tyr, tryptophan, histidine, glutamic acid, cysteine, asparagine, glutamine,

22

lysine, arginine, methionine, and threonine) tested, only Tyr exhibited fluorescence quenching at excitation and emission wavelengths of 295 nm and 530 nm, respectively [117]. The mechanism of quenching is attributed to the capability of the phenol group of Tyr to conduct an extreme charge transfer process between the C-dots. In addition, hydrogen bonding between the functionalized groups of the C-dots and Tyr are present as indicated by the shift in the fluorescence emission spectrum (inter-hydrogen bonding) [117]. This indicated that a binding interaction occurred and was calculated to be 296.38 nM^{-1} [117]. Another study used Tm upconversion nanoparticles (UCNPs) and melanin-like polymers to detect Tyr in the linear range of 0.8–100 μM and with a LOD of 1.1 μM [118]. Tyrosinase was added to the UCNPs and it formed melanin-like polymers in the presence of Tyr that quenched the fluorescence through photoinduced electron transfer (PET) process [118]. This sensor is based on the help of tyrosinase, which oxidizes Tyr and helps to form melanin and melanin-like polymers, which are efficient quenchers [118]. An amino-modified capillary in combination with metal organic framework and near-infrared quantum dots silicon were used to detect Tyr in the linear range of 1.0×10^{-10} to 2.5×10^{-8} M, with a LOD of 8.0×10^{-11} M using a dual-emission approach [119]. In the presence of Tyr, the blue fluorescence at 424 nm was quenched while the red fluorescence at 688 nm did not and served as the reference signal [119]. The mechanism of quenching is due to the inner filter effects between the metal organic framework and Tyr [119]. Both circular dichroism (CD) spectroscopy and fluorescence spectroscopy were used to detect enantiomers of Tyr. L-cysteine-capped CdTe quantum dots (L-Cys/CdTe QDs) were used to detect both L-Tyr and D-Tyr in the linear range of 10–80 μM with LODs of 1.5 and 1.6 μM, respectively with CD spectroscopy [120]. CD spectroscopy provided lower LODs for

the detection of Tyr enantiomers compared to fluorescence spectroscopy, which only provided a LOD of 2.9 µM for L-Tyr and 4.8 µM for D-Tyr in the linear range of 5–90 µM [120]. In the presence of 200 µM of L-Tyr and D-Tyr, 82% and 74% quenching was observed [120]. Energy band gaps of 2.59 eV and 2.10 eV were calculated for the interaction between the QDs and Tyr enantiomers, L-Tyr and DTyr, respectively [120]. The high binding gap for QD and L-Tyr provides a stronger interaction leading to more quenching that was observed [120].[171] Luminescence has also been used to detect Tyr. One particular study used Eu-Ciprofloxacin complex doped in sol-gel matrix to detect Tyr in acetonitrile at pH 9.1 and at an excitation wavelength of 380 nm [121]. In the presence of increasing concentrations of Tyr, the luminescence intensity of the Eu-Ciprofloxacin complex decreases [121]. This nano optical sensor had a LOD of 1.0×10^{-10} mol L^{-1} in the linear range of 1.2×10^{-6} to 1.0×10^{-9} mol L^{-1} [121]. Colorimetric assays using gold nanoparticles have also been used to detect Tyr [122–125].

Similarly, fluorescence spectroscopy and luminescence were used to detect nTyr with the help of nanomaterials like bio-inspired molecularly imprinted polymer as a receptor and green emitting carbon dots (CDs) as a signal transducer (BMIP@CDs) [126], hybrid material (AuNCs@ZIF-8) synthesized by encapsulating gold nanoclusters (AuNCs) into the zeolitic imidazolate framework (ZIF-8) [127], and binuclear Pt-2-pyrazinecarboxylic acid (pca)-Bipyridine (bpy) complex doped in sol-gel matrix (Figure 1.8) [128]. In all three systems, the fluorescence intensity decreased as nTyr concentration increased as plotted by the fluorescence emission spectrum. The sensor using BMIP@CDs are quenched through a photoinduced electron process from the excited CDs to nTyr (Figure 1.8A) [126]. The sensor using AuNCs@ZIF-8 were most likely quenched through

an electron transfer process from the amino group to the aromatic ring of nTyr (Figure 1.8B) [127]. Lastly, the sensor using the zeolitic imidazolate framework were quenched at the 528 nm emission band due to nTyr oxidizing Pt complexes (Figure 1.8C) [128]. These studies had LODs in the nanomolar range. Thus, the use of nanomaterial-based optical sensors provides a great tool for the detection of Tyr and its analogues as demonstrated by these studies.
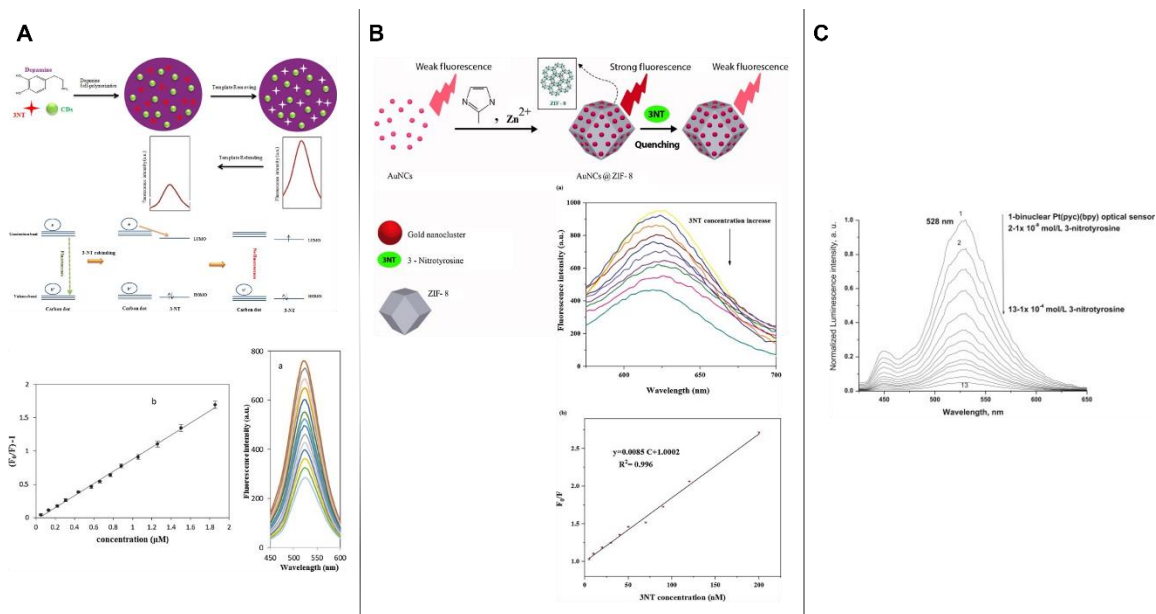
Figure 1.8. Scheme of nanomaterial-based optical sensors for detecting nTyr using bio-inspired molecularly imprinted polymer as a receptor and green emitting carbon dots (CDs) as a signal transducer [126], hybrid material (AuNCs@ZIF-8) synthesized by encapsulating gold nanoclusters (AuNCs) into the zeolitic imidazolate framework (ZIF-8) [127], and binuclear Pt-2-pyrazinecarboxylic acid (pca)-Bipyridine (bpy) complex doped in sol-gel matrix [128].

Table 1.2. Nanomaterial-based optical sensors for detecting Tyr and nTyr.

Method Used	Material	Analyte	Linear range	Limit of Detection (LOD)	Reference
Fluorescence spectroscopy	Carbon dots prepared using waste coconut coir	Tyr	1-100 nM	0.96 nM	[117]
Fluorescence spectroscopy	Nitrogen doped carbon dots mixed with potassium triiodide	Tyr	0.931 –5.35 µM	950 nM	[129]
Fluorescence spectroscopy	fluorescent green carbon quantum dots (G-CQDs) from the latex of Ficus benghalensis as the carbon source and polyethyleneimine as the nitrogen source	Tyr	0 to 100 µM	0.13 µM	[123]
Fluorescence spectroscopy	graphene quantum dots	Tyr	1.0–160 µmol L^{-1}	0.5 µmol L^{-1}	[130]
Fluorescence spectroscopy	NaYF4:Yb, Tm upconversion nanoparticles (UCNPs) and melanin-like polymers	Tyr	0.8–100 µM	1.1 µM	[118]
Fluorescence spectroscopy	luminescence metal organic framework and near-infrared quantum dots	Tyr	1.0×10^{-10} - 2.5×10^{-8} M	8.0×10^{-11} M	[119]

Table 1.2 continued

	silicon embedded into the imprinted layer, grown up on the inner surface of amino-modified capillary					
Circular Dichroism spectroscopy and Fluorescence spectroscopy	L-cysteine-capped CdTe quantum dots (L-Cys/CdTe QDs)	Tyr	5×10^{-6} to 9×10^{-5} M	2.9×10^{-6}	[120]
Luminescence	nano optical sensor Eu–ciprofloxacin doped in a sol–gel matrix	Tyr	1.2×10^{-6} - 1.0×10^{-9} mol L^{-1}	1.0×10^{-10} mol L^{-1}	[121]
Colourimetric assay, UV-vis spectroscopy and vibrational spectroscopy	aggregated Au nanoparticles upon N-hydroxysuccinimide ester bioconjugations	Tyr	N/A	$\sim 10^{-6}$ M	[125]
Liquid crystal	gold nanoparticles (AuNPs)	Tyr	1–100 μM	0.2 μM	[131]
Colourimetric assay	tetrachloroaurate and gold nanoparticles	Tyr	2–200 μM	8×10^{-7} mol L^{-1}	[124]
Colourimetric assay	gold nanoparticles	Tyr	20–200 μM	2.5 μM	[122]
Fluorescence spectroscopy	bio-inspired molecularly imprinted polymer as a receptor and green emitting carbon dots (CDs) as a signal transducer	nTyr	0.050–1.85 μM	17 nM	[126]

Table 1.2 continued

Fluorescence spectroscopy	hybrid material (AuNCs@ZIF-8) synthesized by encapsulating gold nanoclusters (AuNCs) into the zeolitic imidazolate framework (ZIF-8)	nTyr	5−200 nM	1.8 nM	[127]
Luminescence	binuclear Pt-2-pyrazinecarboxylic acid (pca)-Bipyridine (bpy) complex doped in sol-gel matrix	nTyr	0.795-18500 nM	0.47 nM	[128]

1.4 Thesis experimental rationale

Given the desirable and tunable optical properties of CDs, they are valuable probes for biosensors. This thesis will seek to gain a fundamental understanding of the interactions between CDs and biological molecules like amino acids. For example, understanding how such nanomaterials interact with specifically, Tyr and its analogues, is lacking and hinders progress in biomaterials research. In addition, recent discoveries of catalytic properties of CDs indicate their ability to drive biologically relevant transformations and could potentially be used as indicators of such transformations, which is of interest. This thesis focuses on the application of nanomaterials, specifically, CDs as biosensors. The objectives of this thesis are the following: firstly, to explore the photophysical properties of CDs using fluorescence spectroscopy and UV-vis spectroscopy; secondly, to investigate CDs as a function of Tyr and its analogues pTyr and nTyr using fluorescence and UV-vis spectroscopy; and thirdly, to monitor *in vitro* nitration of tyrosine using CDs. Chapter 2 of

this thesis outlines the interactions between Tyr, its analogues and CDs using UV-vis spectroscopy and fluorescence spectroscopy and provides insight into the mechanism of quenching by nTyr. Chapter 3 outlines the use of copper(II) and iron(III) as catalysts of Tyr nitration and explores the use of CDs to monitor nTyr formation. Lastly, Chapter 4 provides conclusions and future work of this project.

1.5 References

[1]   T.A. King, J. Mandrup Kandemir, S.J. Walsh, D.R. Spring, Photocatalytic methods for amino acid modification, Chemical Society Reviews. 50 (2021) 39–57. https://doi.org/10.1039/d0cs00344a.

[2]   S. Dato, E. Hoxha, P. Crocco, F. Iannone, G. Passarino, G. Rose, Amino acids and amino acid sensing: implication for aging and diseases. Biogerontology. 20 (2019) 17-31

[3]   S.M. Ghoreishi, M. Behpour, M. Delshad, A. Khoobi, Electrochemical determination of tyrosine in the presence of uric acid at a carbon paste electrode modified with multi-walled carbon nanotubes enhanced by sodium dodecyl sulfate, Central European Journal of Chemistry. 10 (2012) 1824–1829. https://doi.org/10.2478/s11532-012-0119-x.

[4]   J.P. Greenstein, M. Winitz, Chemistry of the amino acids., (1961).

[5]   F. Vella, The metabolic and molecular bases of inherited disease seventh edition: Edited by C R Sriver, A L Beaudet, W S Sly and D Valle. P 4605. McGraw-Hill, New York. 1995. ISBN 0-07-909826-6., Biochemical Education. 24 (1996) 65. https://doi.org/https://doi.org/10.1016/S0307-4412(96)80019-7.

[6]   R.J. Levine, H. 0 Conn, Tyrosine Metabolism in Patients with Liver Disease *, 1967.

[7]   P.A. Russo, G.A. Mitchell, R.M. Tanguay, Tyrosinemia: A review, Pediatric and Developmental Pathology. 4 (2001) 212–221. https://doi.org/10.1007/s100240010146.

[8]   L. Fiore, B. de Lellis, V. Mazzaracchio, E. Suprun, R. Massoud, B.M. Goffredo, D. Moscone, F. Arduini, Smartphone-assisted electrochemical sensor for reliable detection of tyrosine in serum, Talanta. 237 (2022). https://doi.org/10.1016/j.talanta.2021.122869.

[9]   A. Slominski, M.A. Zmijewski, J. Pawelek, L-tyrosine and L-dihydroxyphenylalanine as hormone-like regulators of melanocyte functions, Pigment Cell and Melanoma Research. 25 (2012) 14–27. https://doi.org/10.1111/j.1755-148X.2011.00898.x.

[10]   D.G. Knorre, N. v Kudryashova, T.S. Godovikova, Chemical and Functional Aspects of Posttranslational Modification of Proteins, n.d.

[11]   L.H. Jones, A. Narayanan, E.C. Hett, Understanding and applying tyrosine biochemical diversity, Molecular BioSystems. 10 (2014) 952–969. https://doi.org/10.1039/c4mb00018h.

[12]   T. Hunter, Tyrosine phosphorylation: thirty years and counting, Current Opinion in Cell Biology. 21 (2009) 140–146. https://doi.org/10.1016/j.ceb.2009.01.028.

[13]   K.E. Tifft, K.A. Bradbury, K.L. Wilson, Tyrosine phosphorylation of nuclear-membrane protein emerin by Src, Abl and other kinases, Journal of Cell Science. 122 (2009) 3780–3790. https://doi.org/10.1242/jcs.048397.

[14]   G.V.W. Johnson, W.H. Stoothoff, Tau phosphorylation in neuronal cell function and dysfunction, Journal of Cell Science. 117 (2004) 5721–5729. https://doi.org/10.1242/jcs.01558.

[15]   G. Lee, R. Thangavel, V.M. Sharma, J.M. Litersky, K. Bhaskar, S.M. Fang, L.H. Do, A. Andreadis, G. van Hoesen, H. Ksiezak-Reding, Phosphorylation of Tau by Fyn: Implications for Alzheimer's Disease, Journal of Neuroscience. 24 (2004) 2304–2312. https://doi.org/10.1523/JNEUROSCI.4162-03.2004.

[16]   R. Radi, Protein tyrosine nitration: Biochemical mechanisms and structural basis of functional effects, Accounts of Chemical Research. 46 (2013) 550–559. https://doi.org/10.1021/ar300234c.

[17]   M.P. Kummer, M. Hermes, A. Delekarte, T. Hammerschmidt, S. Kumar, D. Terwel, J. Walter, H.C. Pape, S. König, S. Roeber, F. Jessen, T. Klockgether, M. Korte, M.T. Heneka, Nitration of tyrosine 10 critically enhances amyloid β aggregation and plaque formation, Neuron. 71 (2011) 833–844. https://doi.org/10.1016/j.neuron.2011.07.001.

[18]   J.F. Reyes, Y. Fu, L. Vana, N.M. Kanaan, L.I. Binder, Tyrosine nitration within the proline-rich region of tau in Alzheimer's disease, American Journal of Pathology. 178 (2011) 2275–2285. https://doi.org/10.1016/j.ajpath.2011.01.030.

[19]   M.H. Shishehbor, R.J. Aviles, M.-L. Brennan, X. Fu, M. Goormastic, G.L. Pearce, N. Gokce, J.F. Keaney, M.S. Penn, D.L. Sprecher, J.A. Vita, S.L. Hazen, Association of Nitrotyrosine Levels With Cardiovascular Disease and Modulation by Statin Therapy, n.d. https://jamanetwork.com/.

[20]   T. Hanazawa, S.A. Kharitonov, P.J. Barnes, Increased Nitrotyrosine in Exhaled Breath Condensate of Patients with Asthma, 2000. www.atsjournals.org.

[21]   C.C. Negut, R.-I. Stefan-van Staden, Review—Recent Trends in Supramolecular Recognition of Dopamine, Tyrosine, and Tryptophan, Using Electrochemical Sensors, Journal of The Electrochemical Society. 168 (2021) 067517. https://doi.org/10.1149/1945-7111/ac0a22.

[22] V. Brabec, V. Mornstein, ELECTI%GCHEMICA_L BEHAVIOUR OF
      PROTEINS AT GRAPHITE ELECTRODES. II. ELECTROOXIDATION OF
      AMINO ACIDS, n.d.

[23] J.A. Reynaud, B. Malfoy, A. Bere, 359-The Electrochemical Oxidation of Three
      Proteins: ltNAasc A, Bovine Serum Albumin and Concanavalin A at Solid
      Electrodes *, Elsevier Sequoia S.A, n.d.

[24]   delanji Vestergaard, K. Kerman, E. Tamiya, An Overview of Label-free
      Electrochemical Protein Sensors, Sensors. 7 (2007) 3442–3458.
      www.mdpi.org/sensors.

[25] G. Neurauter, S. Scholl-Bürgi, A. Haara, S. Geisler, P. Mayersbach, H. Schennach,
      D. Fuchs, Simultaneous measurement of phenylalanine and tyrosine by high
      performance liquid chromatography (HPLC) with fluorescence detection, Clinical
      Biochemistry. 46 (2013) 1848–1851.
      https://doi.org/10.1016/j.clinbiochem.2013.10.015.

[26] E. Waraksa, K. Kowalski, R. Rola, E. Kłodzińska, T. Bieńkowski, J. Namieśnik,
      Determination of free tyrosine in equestrian supplements by LC–MS/MS and
      comparison of its quantity with total free amino acids content in view of doping
      control, Microchemical Journal. 146 (2019) 56–65.
      https://doi.org/10.1016/j.microc.2018.12.033.

[27] M.S. Tremblay, M. Lee, D. Sames, A luminescent sensor for tyrosine
      phosphorylation, Organic Letters. 10 (2008) 5–8.
      https://doi.org/10.1021/ol701920x.

[28] D.S. Lawrence, Q. Wang, Seeing is believing: Peptide-based fluorescent sensors of
      protein tyrosine kinase activity, ChemBioChem. 8 (2007) 373–378.
      https://doi.org/10.1002/cbic.200600473.

[29] J. Sumaoka, H. Akiba, M. Komiyama, Selective Sensing of Tyrosine
      Phosphorylation in Peptides Using Terbium(III) Complexes, International Journal
      of Analytical Chemistry. 2016 (2016). https://doi.org/10.1155/2016/3216523.

[30] S. Greenacre, H. Ischiropoulos, Tyrosine nitration: Localisation, quantification,
      consequences for protein function and signal transduction, Free Radical Research.
      34 (2001) 541–581. https://doi.org/10.1080/10715760100300471.

[31] M. Bandookwala, D. Thakkar, P. Sengupta, Advancements in the Analytical
      Quantification of Nitroxidative Stress Biomarker 3-Nitrotyrosine in Biological
      Matrices, Critical Reviews in Analytical Chemistry. 50 (2020) 265–289.
      https://doi.org/10.1080/10408347.2019.1623010.

[32] D. Teixeira, R. Fernandes, C. Prudêncio, M. Vieira, 3-Nitrotyrosine quantification
      methods: Current concepts and future challenges, Biochimie. 125 (2016) 1–11.
      https://doi.org/10.1016/j.biochi.2016.02.011.

[33] L.A. Kolahalam, I. v. Kasi Viswanath, B.S. Diwakar, B. Govindh, V. Reddy,
      Y.L.N. Murthy, Review on nanomaterials: Synthesis and applications, in:

Materials Today: Proceedings, Elsevier Ltd, 2019: pp. 2182–2190.
https://doi.org/10.1016/j.matpr.2019.07.371.

[34] S. Roy, C.K. Ghosh, C.K. Sarkar, Nanotechnology: Synthesis to applications, CRC Press. (2017)

[35] N. Baig, I. Kammakakam, W. Falath, I. Kammakakam, Nanomaterials: A review of synthesis methods, properties, recent progress, and challenges, Materials Advances. 2 (2021) 1821–1871. https://doi.org/10.1039/d0ma00807a.

[36] F.R. Baptista, S.A. Belhout, S. Giordani, S.J. Quinn, Recent developments in carbon nanomaterial sensors, Chemical Society Reviews. 44 (2015) 4433–4453. https://doi.org/10.1039/c4cs00379a.

[37] X. Chen, P. Gao, L. Guo, S. Zhang, Graphdiyne as a promising material for detecting amino acids, Scientific Reports. 5 (2015). https://doi.org/10.1038/srep16720.

[38] X. Xu, R. Ray, Y. Gu, H.J. Ploehn, L. Gearheart, K. Raker, W.A. Scrivens, Electrophoretic analysis and purification of fluorescent single-walled carbon nanotube fragments, J Am Chem Soc. 126 (2004) 12736–12737. https://doi.org/10.1021/ja040082h.

[39] H. Li, X. Yan, D. Kong, R. Jin, C. Sun, D. Du, Y. Lin, G. Lu, Recent advances in carbon dots for bioimaging applications, Nanoscale Horizons. 5 (2020) 218–234. https://doi.org/10.1039/c9nh00476a.

[40] L. Han, D. Ghosh, W. Chen, S. Pradhan, X. Chang, S. Chen, Nanosized carbon particles from natural gas soot, Chemistry of Materials. 21 (2009) 2803–2809. https://doi.org/10.1021/cm900709w.

[41] J. Peng, W. Gao, B.K. Gupta, Z. Liu, R. Romero-Aburto, L. Ge, L. Song, L.B. Alemany, X. Zhan, G. Gao, S.A. Vithayathil, B.A. Kaipparettu, A.A. Marti, T. Hayashi, J.J. Zhu, P.M. Ajayan, Graphene quantum dots derived from carbon fibers, Nano Letters. 12 (2012) 844–849. https://doi.org/10.1021/nl2038979.

[42] Z.A. Qiao, Y. Wang, Y. Gao, H. Li, T. Dai, Y. Liu, Q. Huo, Commercially activated carbon as the source for producing multicolor photoluminescent carbon dots by chemical oxidation, Chemical Communications. 46 (2010) 8812–8814. https://doi.org/10.1039/c0cc02724c.

[43] Y. Dong, C. Chen, X. Zheng, L. Gao, Z. Cui, H. Yang, C. Guo, Y. Chi, C.M. Li, One-step and high yield simultaneous preparation of single- and multi-layer graphene quantum dots from CX-72 carbon black, Journal of Materials Chemistry. 22 (2012) 8764–8766. https://doi.org/10.1039/c2jm30658a.

[44] D. Pan, J. Zhang, Z. Li, M. Wu, Hydrothermal route for cutting graphene sheets into blue-luminescent graphene quantum dots, Advanced Materials. 22 (2010) 734–738. https://doi.org/10.1002/adma.200902825.

[45] Z. Peng, Y. Zhou, C. Ji, J. Pardo, K.J. Mintz, R.R. Pandey, C.C. Chusuei, R.M. Graham, G. Yan, R.M. Leblanc, Facile synthesis of "boron-doped" carbon dots

and their application in visible-light-driven photocatalytic degradation of organic dyes, Nanomaterials. 10 (2020) 1–17. https://doi.org/10.3390/nano10081560.

[46]   H. Li, Z. Zheng, M. Liu, H. Jiang, D. Hu, X. Zhang, L. Xia, X. Geng, J. Lu, X. Cheng, Y. Wan, P. Yang, Visible light photo-treatment of simulated wastewater activated by high-efficient photocatalyst: A novel heterojunction of Bi2MoO6 balls and Pd nanoskeletons, Applied Surface Science. 510 (2020). https://doi.org/10.1016/j.apsusc.2020.145468.

[47]   J. Schneider, C.J. Reckmeier, Y. Xiong, M. von Seckendorff, A.S. Susha, P. Kasak, A.L. Rogach, Molecular fluorescence in citric acid-based carbon dots, Journal of Physical Chemistry C. 121 (2017) 2014–2022. https://doi.org/10.1021/acs.jpcc.6b12519.

[48]   Y. Liu, N. Xiao, N. Gong, H. Wang, X. Shi, W. Gu, L. Ye, One-step microwave-assisted polyol synthesis of green luminescent carbon dots as optical nanoprobes, Carbon N Y. 68 (2014) 258–264. https://doi.org/10.1016/j.carbon.2013.10.086.

[49]   N. Sahiner, S.S. Suner, M. Sahiner, C. Silan, Nitrogen and Sulfur Doped Carbon Dots from Amino Acids for Potential Biomedical Applications, (n.d.). https://doi.org/10.1007/s10895-019-02431-y/Published.

[50]   L. Cao, X. Wang, M.J. Meziani, F. Lu, H. Wang, P.G. Luo, Y. Lin, B.A. Harruff, L.M. Veca, D. Murray, S.Y. Xie, Y.P. Sun, Carbon dots for multiphoton bioimaging, J Am Chem Soc. 129 (2007) 11318–11319. https://doi.org/10.1021/ja073527l.

[51]   S.T. Yang, L. Cao, P.G. Luo, F. Lu, X. Wang, H. Wang, M.J. Meziani, Y. Liu, G. Qi, Y.P. Sun, Carbon dots for optical imaging in vivo, J Am Chem Soc. 131 (2009) 11308–11309. https://doi.org/10.1021/ja904843x.

[52]   Q.L. Zhao, Z.L. Zhang, B.H. Huang, J. Peng, M. Zhang, D.W. Pang, Facile preparation of low cytotoxicity fluorescent carbon nanocrystals by electrooxidation of graphite, Chemical Communications. (2008) 5116–5118. https://doi.org/10.1039/b812420e.

[53]   S.C. Ray, A. Saha, N.R. Jana, R. Sarkar, Fluorescent carbon nanoparticles: Synthesis, characterization, and bioimaging application, Journal of Physical Chemistry C. 113 (2009) 18546–18551. https://doi.org/10.1021/jp905912n.

[54]   J. Zhou, X. Zhou, R. Li, X. Sun, Z. Ding, J. Cutler, T.K. Sham, Electronic structure and luminescence center of blue luminescent carbon nanocrystals, Chemical Physics Letters. 474 (2009) 320–324. https://doi.org/10.1016/j.cplett.2009.04.075.

[55]   C. Ji, Y. Zhou, R.M. Leblanc, Z. Peng, Recent Developments of Carbon Dots in Biosensing: A Review, ACS Sensors. 5 (2020) 2724–2741. https://doi.org/10.1021/acssensors.0c01556.

[56]   L. Bao, Z.L. Zhang, Z.Q. Tian, L. Zhang, C. Liu, Y. Lin, B. Qi, D.W. Pang, Electrochemical tuning of luminescent carbon nanodots: From preparation to

luminescence mechanism, Advanced Materials. 23 (2011) 5801–5806. https://doi.org/10.1002/adma.201102866.

[57] D. Xu, Q. Lin, H.T. Chang, Recent Advances and Sensing Applications of Carbon Dots, Small Methods. 4 (2020). https://doi.org/10.1002/smtd.201900387.

[58] S. Yang, J. Sun, X. Li, W. Zhou, Z. Wang, P. He, G. Ding, X. Xie, Z. Kang, M. Jiang, Large-scale fabrication of heavy doped carbon quantum dots with tunable-photoluminescence and sensitive fluorescence detection, Journal of Materials Chemistry A. 2 (2014) 8660–8667. https://doi.org/10.1039/c4ta00860j.

[59] F. Li, D. Yang, H. Xu, Non-Metal-Heteroatom-Doped Carbon Dots: Synthesis and Properties, Chemistry - A European Journal. 25 (2019) 1165–1176. https://doi.org/10.1002/chem.201802793.

[60] H. Ding, J.S. Wei, N. Zhong, Q.Y. Gao, H.M. Xiong, Highly Efficient Red-Emitting Carbon Dots with Gram-Scale Yield for Bioimaging, Langmuir. 33 (2017) 12635–12642. https://doi.org/10.1021/acs.langmuir.7b02385.

[61] C. Zhu, C. Liu, Y. Zhou, Y. Fu, S. Guo, H. Li, S. Zhao, H. Huang, Y. Liu, Z. Kang, Carbon dots enhance the stability of CdS for visible-light-driven overall water splitting, Applied Catalysis B: Environmental. 216 (2017) 114–121. https://doi.org/10.1016/j.apcatb.2017.05.049.

[62] X. Wu, C. Zhu, L. Wang, S. Guo, Y. Zhang, H. Li, H. Huang, Y. Liu, J. Tang, Z. Kang, Control Strategy on Two-/Four-Electron Pathway of Water Splitting by Multidoped Carbon Based Catalysts, ACS Catalysis. 7 (2017) 1637–1645. https://doi.org/10.1021/acscatal.6b03244.

[63] C. Zhu, M. Zhu, Y. Sun, Y. Zhou, H. Huang, Y. Lifshitz, S.T. Lee, J. Zhong, Y. Liu, Z. Kang, Defects induced efficient overall water splitting on a carbon-based metal-free photocatalyst, Applied Catalysis B: Environmental. 237 (2018) 166–174. https://doi.org/10.1016/j.apcatb.2018.05.071.

[64] R. Liu, H. Huang, H. Li, Y. Liu, J. Zhong, Y. Li, S. Zhang, Z. Kang, Metal nanoparticle/carbon quantum dot composite as a photocatalyst for high-efficiency cyclohexane oxidation, ACS Catalysis. 4 (2014) 328–336. https://doi.org/10.1021/cs400913h.

[65] S. Zhao, Z. Tang, S. Guo, M. Han, C. Zhu, Y. Zhou, L. Bai, J. Gao, H. Huang, Y. Li, Y. Liu, Z. Kang, Enhanced Activity for CO2 Electroreduction on a Highly Active and Stable Ternary Au-CDots-C3N4 Electrocatalyst, ACS Catalysis. 8 (2018) 188–197. https://doi.org/10.1021/acscatal.7b01551.

[66] M. Tuerhong, Y. XU, X.B. YIN, Review on Carbon Dots and Their Applications, Chinese Journal of Analytical Chemistry. 45 (2017) 139–150. https://doi.org/10.1016/S1872-2040(16)60990-8.

[67] J. Wang, J. Qiu, A review of carbon dots in biological applications, Journal of Materials Science. 51 (2016) 4728–4738. https://doi.org/10.1007/s10853-016-9797-7.

[68] T. v. de Medeiros, J. Manioudakis, F. Noun, J.R. Macairan, F. Victoria, R. Naccache, Microwave-assisted synthesis of carbon dots and their applications, Journal of Materials Chemistry C. 7 (2019) 7175–7195. https://doi.org/10.1039/c9tc01640f.

[69] J.R. Macairan, D.B. Jaunky, A. Piekny, R. Naccache, Intracellular ratiometric temperature sensing using fluorescent carbon dots, Nanoscale Advances. 1 (2019) 105–113. https://doi.org/10.1039/c8na00255j.

[70] H.U. Lee, S.Y. Park, E.S. Park, B. Son, S.C. Lee, J.W. Lee, Y.C. Lee, K.S. Kang, M. il Kim, H.G. Park, S. Choi, Y.S. Huh, S.Y. Lee, K.B. Lee, Y.K. Oh, J. Lee, Photoluminescent carbon nanotags from harmful cyanobacteria for drug delivery and imaging in cancer cells, Scientific Reports. 4 (2014). https://doi.org/10.1038/srep04665.

[71] L. Zhou, Z. Li, Z. Liu, J. Ren, X. Qu, Luminescent carbon dot-gated nanovehicles for ph-triggered intracellular controlled release and imaging, Langmuir. 29 (2013) 6396–6403. https://doi.org/10.1021/la400479n.

[72] L. Pan, S. Sun, L. Zhang, K. Jiang, H. Lin, Near-infrared emissive carbon dots for two-photon fluorescence bioimaging, Nanoscale. 8 (2016) 17350–17356. https://doi.org/10.1039/c6nr05878g.

[73] A.M. Oliveira-Brett, V.C. Diculescu, T.A. Enache, I.P.G. Fernandes, A.M. Chiorcea-Paquim, S.C.B. Oliveira, Bioelectrochemistry for sensing amino acids, peptides, proteins and DNA interactions, Current Opinion in Electrochemistry. 14 (2019) 173–179. https://doi.org/10.1016/j.coelec.2019.03.008.

[74] Y. Si, H.J. Lee, Carbon nanomaterials and metallic nanoparticles-incorporated electrochemical sensors for small metabolites: Detection methodologies and applications, Current Opinion in Electrochemistry. 22 (2020) 234–243. https://doi.org/10.1016/j.coelec.2020.08.007.

[75] I.S. Kucherenko, O.O. Soldatkin, D.Y. Kucherenko, O. v. Soldatkina, S. v. Dzyadevych, Advances in nanomaterial application in enzyme-based electrochemical biosensors: a review, Nanoscale Advances. 1 (2019) 4560–4577. https://doi.org/10.1039/c9na00491b.

[76] S. Song, L. Wang, J. Li, C. Fan, J. Zhao, Aptamer-based biosensors, TrAC - Trends in Analytical Chemistry. 27 (2008) 108–117. https://doi.org/10.1016/j.trac.2007.12.004.

[77] M.A. Beluomini, J.L. da Silva, A.C. de Sá, E. Buffon, T.C. Pereira, N.R. Stradiotto, Electrochemical sensors based on molecularly imprinted polymer on nanostructured carbon materials: A review, Journal of Electroanalytical Chemistry. 840 (2019) 343–366. https://doi.org/10.1016/j.jelechem.2019.04.005.

[78] W. Zheng, M. Zhao, W. Liu, S. Yu, L. Niu, G. Li, H. Li, W. Liu, Electrochemical sensor based on molecularly imprinted polymer/reduced graphene oxide composite for simultaneous determination of uric acid and tyrosine, Journal of

Electroanalytical Chemistry. 813 (2018) 75–82.
https://doi.org/10.1016/j.jelechem.2018.02.022.

[79]   S. Wang, G. Sun, Z. Chen, Y. Liang, Q. Zhou, Y. Pan, H. Zhai, Constructing a
       novel composite of molecularly imprinted polymer-coated AuNPs electrochemical
       sensor for the determination of 3-nitrotyrosine, Electrochimica Acta. 259 (2018)
       893–902. https://doi.org/10.1016/j.electacta.2017.11.033.

[80]   O.J. D'Souza, R.J. Mascarenhas, A.K. Satpati, L. v. Aiman, Z. Mekhalif,
       Electrocatalytic oxidation of L-tyrosine at carboxylic acid functionalized multi-
       walled carbon nanotubes modified carbon paste electrode, Ionics (Kiel). 22 (2016)
       405–414. https://doi.org/10.1007/s11581-015-1552-6.

[81]   S.M. Ghoreishi, M. Behpour, M. Delshad, A. Khoobi, Electrochemical
       determination of tyrosine in the presence of uric acid at a carbon paste electrode
       modified with multi-walled carbon nanotubes enhanced by sodium dodecyl sulfate,
       Central European Journal of Chemistry. 10 (2012) 1824–1829.
       https://doi.org/10.2478/s11532-012-0119-x.

[82]   Y. Fan, J.H. Liu, H.T. Lu, Q. Zhang, Electrochemistry and voltammetric
       determination of L-tryptophan and L-tyrosine using a glassy carbon electrode
       modified with a Nafion/TiO2-graphene composite film, Microchimica Acta. 173
       (2011) 241–247. https://doi.org/10.1007/s00604-011-0556-9.

[83]   J. Li, D. Kuang, Y. Feng, F. Zhang, Z. Xu, M. Liu, D. Wang, Electrochemical
       tyrosine sensor based on a glassy carbon electrode modified with a nanohybrid
       made from graphene oxide and multiwalled carbon nanotubes, Microchimica Acta.
       180 (2013) 49–58. https://doi.org/10.1007/s00604-012-0905-3.

[84]   M.L. Yola, T. Eren, N. Atar, A sensitive molecular imprinted electrochemical
       sensor based on gold nanoparticles decorated graphene oxide: Application to
       selective determination of tyrosine in milk, Sensors and Actuators, B: Chemical.
       210 (2015) 149–157. https://doi.org/10.1016/j.snb.2014.12.098.

[85]   X. Tang, Y. Liu, H. Hou, T. You, Electrochemical determination of L-Tryptophan,
       L-Tyrosine and L-Cysteine using electrospun carbon nanofibers modified
       electrode, Talanta. 80 (2010) 2182–2186.
       https://doi.org/10.1016/j.talanta.2009.11.027.

[86]   H. Razmi, H. Nasiri, R. Mohammad-Rezaei, Amperometric determination of L-
       tyrosine by an enzymeless sensor based on a carbon ceramic electrode modified
       with copper oxide nanoparticles, Microchimica Acta. 173 (2011) 59–64.
       https://doi.org/10.1007/s00604-010-0527-6.

[87]   N. Baig, A.N. Kawde, A novel, fast and cost effective graphene-modified graphite
       pencil electrode for trace quantification of l-tyrosine, Analytical Methods. 7 (2015)
       9535–9541. https://doi.org/10.1039/c5ay01753j.

[88]   Ö.A. Yokuş, F. Kardaş, O. Akyildirim, T. Eren, N. Atar, M.L. Yola, Sensitive
       voltammetric sensor based on polyoxometalate/reduced graphene oxide

nanomaterial: Application to the simultaneous determination of l-tyrosine and l-tryptophan, Sensors and Actuators, B: Chemical. 233 (2016) 47–54. https://doi.org/10.1016/j.snb.2016.04.050.

[89]   K. Murtada, R. Salghi, A. Ríos, M. Zougagh, A sensitive electrochemical sensor based on aluminium doped copper selenide nanoparticles-modified screen printed carbon electrode for determination of L-tyrosine in pharmaceutical samples, Journal of Electroanalytical Chemistry. 874 (2020). https://doi.org/10.1016/j.jelechem.2020.114466.

[90]   J. Xu, Y. Wang, Y. Xian, L. Jin, K. Tanaka, Preparation of multiwall carbon nanotubes film modified electrode and its application to simultaneous determination of oxidizable amino acids in ion chromatography, Talanta. 60 (2003) 1123–1130. https://doi.org/10.1016/S0039-9140(03)00214-5.

[91]   X. Yu, Z. Mai, Y. Xiao, X. Zou, Electrochemical behavior and determination of L-tyrosine at single-walled carbon nanotubes modified glassy carbon electrode, Electroanalysis. 20 (2008) 1246–1251. https://doi.org/10.1002/elan.200704179.

[92]   H. Heli, M. Hajjizadeh, A. Jabbari, A.A. Moosavi-Movahedi, Fine steps of electrocatalytic oxidation and sensitive detection of some amino acids on copper nanoparticles, Analytical Biochemistry. 388 (2009) 81–90. https://doi.org/10.1016/j.ab.2009.02.021.

[93]   S. Shrestha, R.J. Mascarenhas, O.J. D'Souza, A.K. Satpati, Z. Mekhalif, A. Dhason, P. Martis, Amperometric sensor based on multi-walled carbon nanotube and poly (Bromocresol purple) modified carbon paste electrode for the sensitive determination of L-tyrosine in food and biological samples, Journal of Electroanalytical Chemistry. 778 (2016) 32–40. https://doi.org/10.1016/j.jelechem.2016.08.010.

[94]   X. Liu, L. Luo, Y. Ding, Z. Kang, D. Ye, Simultaneous determination of L-cysteine and L-tyrosine using Au-nanoparticles/poly-eriochrome black T film modified glassy carbon electrode, Bioelectrochemistry. 86 (2012) 38–45. https://doi.org/10.1016/j.bioelechem.2012.01.008.

[95]   J. Zou, D. Mao, A.T.S. Wee, J. Jiang, Micro/nano-structured ultrathin g-C 3 N 4 /Ag nanoparticle hybrids as efficient electrochemical biosensors for L-tyrosine, Applied Surface Science. 467–468 (2019) 608–618. https://doi.org/10.1016/j.apsusc.2018.10.187.

[96]   M. Taei, F. Hasanpour, S. Habibollahi, L. Shahidi, Simultaneous electrochemical sensing of cysteine, uric acid and tyrosine using a novel Au-nanoparticles/poly-Trypan Blue modified glassy carbon electrode, Journal of Electroanalytical Chemistry. 789 (2017) 140–147. https://doi.org/10.1016/j.jelechem.2017.02.035.

[97]   A.S. Razavian, S.M. Ghoreishi, A.S. Esmaeily, M. Behpour, L.M.A. Monzon, J.M.D. Coey, Simultaneous sensing of L-tyrosine and epinephrine using a glassy

carbon electrode modified with nafion and CeO2 nanoparticles, Microchimica Acta. 181 (2014) 1947–1955. https://doi.org/10.1007/s00604-014-1284-8.

[98] J. Narang, N. Chauhan, S. Pundir, C.S. Pundir, A magnetic nanoparticles-zinc oxide/zinc hexacyanoferrate hybrid film for amperometric determination of tyrosine, Bioprocess and Biosystems Engineering. 36 (2013) 1545–1554. https://doi.org/10.1007/s00449-013-0916-4.

[99] Q. Ma, S. Ai, H. Yin, Q. Chen, T. Tang, Towards the conception of an amperometric sensor of l-tyrosine based on Hemin/PAMAM/MWCNT modified glassy carbon electrode, Electrochimica Acta. 55 (2010) 6687–6694. https://doi.org/10.1016/j.electacta.2010.06.003.

[100] K. Varmira, G. Mohammadi, M. Mahmoudi, R. Khodarahmi, K. Rashidi, M. Hedayati, H.C. Goicoechea, A.R. Jalalvand, Fabrication of a novel enzymatic electrochemical biosensor for determination of tyrosine in some food samples, Talanta. 183 (2018) 1–10. https://doi.org/10.1016/j.talanta.2018.02.053.

[101] S. Roy, S. Sain, S. Wadhwa, A. Mathur, S. Dubey, S.S. Roy, Electrochemical impedimetric analysis of different dimensional (0D-2D) carbon nanomaterials for effective biosensing of L-tyrosine, Measurement Science and Technology. 33 (2022). https://doi.org/10.1088/1361-6501/ac2cf3.

[102] A. Karthika, D.R. Rosaline, S.S.R. Inbanathan, A. Suganthi, M. Rajarajan, Fabrication of Cupric oxide decorated β-cyclodextrin nanocomposite solubilized Nafion as a high performance electrochemical sensor for L-tyrosine detection, Journal of Physics and Chemistry of Solids. 136 (2020). https://doi.org/10.1016/j.jpcs.2019.109145.

[103] H. Karimi-Maleh, M.R. Ganjali, P. Norouzi, A. Bananezhad, Amplified nanostructure electrochemical sensor for simultaneous determination of captopril, acetaminophen, tyrosine and hydrochlorothiazide, Materials Science and Engineering C. 73 (2017) 472–477. https://doi.org/10.1016/j.msec.2016.12.094.

[104] P. Kanchana, N. Lavanya, C. Sekar, Development of amperometric l-tyrosine sensor based on Fe-doped hydroxyapatite nanoparticles, Materials Science and Engineering C. 35 (2014) 85–91. https://doi.org/10.1016/j.msec.2013.10.013.

[105] P. Deng, J. Xiao, J. Feng, Y. Tian, Y. Wu, J. Li, Q. He, Highly sensitive electrochemical sensor for tyrosine detection using a sub-millimeter electrode, Microchemical Journal. 165 (2021). https://doi.org/10.1016/j.microc.2021.106106.

[106] S.M. Chen, R. Umamaheswari, G. Mani, T.W. Chen, M.A. Ali, A.H. Fahad, M.S. Elshikh, M.A. Farah, Hierarchically structured CuFe2O4 ND@RGO composite for the detection of oxidative stress biomarker in biological fluids, Inorganic Chemistry Frontiers. 5 (2018) 944–950. https://doi.org/10.1039/c7qi00799j.

[107] N. Nontawong, P. Ngaosri, S. Chunta, P. Jarujamrus, D. Nacapricha, P.A. Lieberzeit, M. Amatatongchai, Smart sensor for assessment of oxidative/nitrative stress biomarkers using a dual-imprinted electrochemical paper-based analytical

device, Analytica Chimica Acta. 1191 (2022).
https://doi.org/10.1016/j.aca.2021.339363.

[108] E. Roy, S. Patra, R. Madhuri, P.K. Sharma, Developing electrochemical sensor for point-of-care diagnostics of oxidative stress marker using imprinted bimetallic Fe/Pd nanoparticle, Talanta. 132 (2015) 406–415. https://doi.org/10.1016/j.talanta.2014.09.033.

[109] M. Govindasamy, S. Manavalan, S.M. Chen, R. Umamaheswari, T.W. Chen, Determination of oxidative stress biomarker 3-nitro-L-tyrosine using CdWO4 nanodots decorated reduced graphene oxide, Sensors and Actuators, B: Chemical. 272 (2018) 274–281. https://doi.org/10.1016/j.snb.2018.05.138.

[110] S. Maheshwaran, M. Akilarasan, S.-M. Chen, T.-W. Chen, E. Tamilalagan, C.Y. Tzu, B.-S. Lou, An Ultra-sensitive Electrochemical Sensor for the Detection of Oxidative Stress Biomarker 3-Nitro-l-tyrosine in Human Blood Serum and Saliva Samples Based on Reduced Graphene Oxide Entrapped Zirconium (IV) Oxide, Journal of The Electrochemical Society. 167 (2020) 066517. https://doi.org/10.1149/1945-7111/ab847d.

[111] L. García-Carmona, M. Moreno-Guzmán, T. Sierra, M.C. González, A. Escarpa, Filtered carbon nanotubes-based electrodes for rapid sensing and monitoring of L-tyrosine in plasma and whole blood samples, Sensors and Actuators, B: Chemical. 259 (2018) 762–767. https://doi.org/10.1016/j.snb.2017.12.090.

[112] J.F. Hernández-Rodríguez, F. della Pelle, D. Rojas, D. Compagnone, A. Escarpa, Xurography-Enabled Thermally Transferred Carbon Nanomaterial-Based Electrochemical Sensors on Polyethylene Terephthalate-Ethylene Vinyl Acetate Films, Analytical Chemistry. 92 (2020) 13565–13572. https://doi.org/10.1021/acs.analchem.0c03240.

[113] J. Okuno, K. Maehashi, K. Matsumoto, K. Kerman, Y. Takamura, E. Tamiya, Single-walled carbon nanotube-arrayed microelectrode chip for electrochemical analysis, Electrochemistry Communications. 9 (2007) 13–18. https://doi.org/10.1016/j.elecom.2006.07.046.

[114] J. Wei, J. Qiu, L. Li, L. Ren, X. Zhang, J. Chaudhuri, S. Wang, A reduced graphene oxide based electrochemical biosensor for tyrosine detection, Nanotechnology. 23 (2012). https://doi.org/10.1088/0957-4484/23/33/335707.

[115] P. Kanchana, M. Navaneethan, C. Sekar, Fabrication of Ce doped hydroxyapatite nanoparticles based non-enzymatic electrochemical sensor for the simultaneous determination of norepinephrine, uric acid and tyrosine, Materials Science and Engineering B: Solid-State Materials for Advanced Technology. 226 (2017) 132–140. https://doi.org/10.1016/j.mseb.2017.09.015.

[116] Z.A. Khan, P.J.S. Hong, C.H. Lee, Y. Hong, Recent advances in electrochemical and optical sensors for detecting tryptophan and melatonin, International Journal of Nanomedicine. 16 (2021) 6861–6888. https://doi.org/10.2147/IJN.S325099.

[117] P. Chauhan, D. Mundekkad, A. Mukherjee, S. Chaudhary, A. Umar, S. Baskoutas, Coconut Carbon Dots: Progressive Large-Scale Synthesis, Detailed Biological Activities and Smart Sensing Aptitudes towards Tyrosine, Nanomaterials. 12 (2022). https://doi.org/10.3390/nano12010162.

[118] Q. Wu, A. Fang, H. Li, Y. Zhang, S. Yao, Enzymatic-induced upconversion photoinduced electron transfer for sensing tyrosine in human serum, Biosensors and Bioelectronics. 77 (2016) 957–962. https://doi.org/10.1016/j.bios.2015.10.084.

[119] S. Tang, P. Zhao, X. Wu, Y. Chen, K. Tang, S. Zhou, J. Fu, H. Lei, Z. Yang, Z. Zhang, A dual-emission ratiometric fluorescence capillary imprinted sensor based on metal-organic frameworks for sensitive detection of L-tyrosine, Sensors and Actuators B: Chemical. 367 (2022). https://doi.org/10.1016/j.snb.2022.132058.

[120] F. Feizi, M. Shamsipur, A. Barati, M.B. Gholivand, F. Mousavi, Chiral recognition and quantitative analysis of tyrosine enantiomers using L-cysteine capped CdTe quantum dots: Circular dichroism, fluorescence, and theoretical calculation studies, Microchemical Journal. 158 (2020). https://doi.org/10.1016/j.microc.2020.105168.

[121] M.S. Attia, A.A. Yakout, Novel Method For Tyrosine Assessment in vitro by Using Luminescence Quenching of The Nano Optical Sensor Eu-Ciprofloxacin Complex Doped in Sol-Gel Matrix, n.d. www.rsc.org/advances.

[122] R. Baron, M. Zayats, I. Willner, Dopamine-, L-DOPA-, adrenaline-, and noradrenaline-induced growth of Au nanoparticles: Assays for the detection of neurotransmitters and of tyrosinase activity, Analytical Chemistry. 77 (2005) 1566–1571. https://doi.org/10.1021/ac048691v.

[123] P.K. Yadav, R.K. Upadhyay, D. Kumar, D. Bano, S. Chandra, S. Jit, S.H. Hasan, Synthesis of green fluorescent carbon quantum dots from the latex ofFicus benghalensisfor the detection of tyrosine and fabrication of Schottky barrier diode, New Journal of Chemistry. 45 (2021) 12549–12556. https://doi.org/10.1039/d1nj01655e.

[124] G. Li, M. Yang, L.C. Chen, B. Gao, X.L. Xiong, Colorimetric and visual detection of tyrosine based on its copper-catalyzed enzymatic oxidation to dopamine and subsequent reductive formation of colored gold nanoparticles using copper ions, Microchimica Acta. 182 (2015) 113–117. https://doi.org/10.1007/s00604-014-1278-6.

[125] J.H. Park, E.O. Ganbold, D. Uuriintuya, K. Lee, S.W. Joo, Hydrogen bonding-induced color recovery of gold nanoparticles upon conjugation of amino acids, Chemical Communications. (2009) 7354–7356. https://doi.org/10.1039/b918687e.

[126] R. Jalili, M. Amjadi, Bio-inspired molecularly imprinted polymer–green emitting carbon dot composite for selective and sensitive detection of 3-nitrotyrosine as a biomarker, Sensors and Actuators, B: Chemical. 255 (2018) 1072–1078. https://doi.org/10.1016/j.snb.2017.08.145.

[127] R. Jalili, M. Dastborhan, S. Chenaghlou, A. Khataee, Incorporating of gold nanoclusters into metal-organic frameworks for highly sensitive detection of 3-nitrotyrosine as an oxidative stress biomarker, Journal of Photochemistry and Photobiology A: Chemistry. 391 (2020). https://doi.org/10.1016/j.jphotochem.2020.112370.

[128] M.S. Attia, N.S. Al-Radadi, Nano optical sensor binuclear Pt-2-pyrazinecarboxylic acid –bipyridine for enhancement of the efficiency of 3-nitrotyrosine biomarker for early diagnosis of liver cirrhosis with minimal hepatic encephalopathy, Biosensors and Bioelectronics. 86 (2016) 406–412. https://doi.org/10.1016/j.bios.2016.06.074.

[129] J. Nebu, K.S. Anu, J.S. Anjali Devi, R.S. Aparna, A.O. Aswathy, G.M. Lekha, G. Sony, Pottasium triiodide enhanced turn-off sensing of tyrosine in carbon dot platform, Microchemical Journal. 146 (2019) 12–19. https://doi.org/10.1016/j.microc.2018.12.021.

[130] Y. Li, N. Cai, M. Wang, W. Na, F. Shi, X. Su, Fluorometric detection of tyrosine and cysteine using graphene quantum dots, RSC Advances. 6 (2016) 33197–33204. https://doi.org/10.1039/c6ra07300j.

[131] X. Li, G. Li, M. Yang, L.C. Chen, X.L. Xiong, Gold nanoparticle based signal enhancement liquid crystal biosensors for tyrosine assays, Sensors and Actuators, B: Chemical. 215 (2015) 152–158. https://doi.org/10.1016/j.snb.2015.03.054.

Chapter 2 - Article in Spectrochimica Acta Part B: Molecular and Biomolecular Spectroscopy - Selective detection of nitrotyrosine using dual-fluorescent carbon dots

Permission was granted by publisher to use this article in the thesis (see Appendix B for permission). Other than thesis-specific formatting, this chapter is presented as the published article.

Supplementary Information of this article can be found in Appendix A.

Nayomi Camilus[1], Stephanie Gao[1], Musonda Mitti,[1] Jun-Ray Macairan[2], Dr. Rafik Naccache[2], Dr. Sanela Martic[1*]

[1]Department of Forensic Science, Environmental and Life Sciences, Trent University, Canada

[2]Department of Chemistry and Biochemistry and Centre for NanoScience Research, Concordia University, Canada

Corresponding author email: sanelamartic@trentu.ca

Author Contributions

The authors confirm contribution to the paper as outlined below. Nayomi Camilus designed, performed, and analyzed all spectroscopical experiments (fluorescence and UV-vis spectroscopy0 in consultation with Dr. Sanela Martic. Stephanie Gao designed, performed, and analyzed all electrochemical experiments in consultation with Dr. Sanela Martic. Dr. Sanela Martic supervised the project. Dr. Rafik Naccache provided the carbon dots. Jun-Ray Macairan performed all experiments and analysis pertaining to the characterization of carbon dots in consultation with Dr. Rafik Naccache. Nayomi Camilus and Dr. Sanela Martic wrote the manuscript with input from all authors. All authors reviewed the results and approved the final version of the manuscript.

Abstract

The post-translational modification of amino acid plays a critical role in normal and diseased biological states. Specifically, nitrotyrosine (nTyr) has been linked to diseases, including neurodegeneration, among others. Hence, alternative methods are required for detection and differentiation of nTyr from other structurally similar analogues, such as Tyrosine (Tyr) or phosphotyrosine (pTyr). Herein, the selective detection of nTyr, over other congeners, was achieved by using dual-fluorescent carbon dots (CDs) in buffered solution, artificial saliva, bovine serum albumin and diluted equine serum. The nTyr induced fluorescence quenching of the blue and red emissions of CDs, in the 20 - 105 µM linear range, and with the limit of detection (LOD) at 34 µM, which was well below the physiological concentration required for detection. The sensor was functional at biological pH values, with optimal quenching efficiency at basic pH. The sensor was highly selective for nTyr even in the presence of common biological interferences (metal cations, organic anions, amino acids, nucleosides and other biologicals). The mechanism of quenching (a combination of static and dynamic) was ascribed to the combination of the nonradiative energy transfer, due to electronic overlap between nTyr absorbance and CDs fluorescence emission, and electron transfer from excited CDs state to nTyr as an electron acceptor. The dual-fluorescent CDs represent viable sensors for key biological modifications, and their selectivity and sensitivity may be further improved through tailored chemical synthesis of CDs, such as tunable surface chemistry to promote selective recognition of analyte of interest.

2.1 Introduction

The nitration of tyrosine (Tyr) plays a critical biological role and has been linked to various diseases, including neurodegeneration, heart disease and cancer, among others [1,2]. The nitration

is a covalent modification of one of the *ortho* groups of benzene ring with a nitro group (-NO_2) from nitrating agents, such as nitrogen dioxide [3]. The nitration of Tyr residue results in the 3-nitrotyrosine (nTyr) which is known to play a role in neurodegenerative disease like Alzheimer's disease, such as the nitration of Tyr 10 in Amyloid beta which promoted aggregation [1]. The higher levels of nTyr are also indicative of oxidative stress and tissue damage, being implicated in cardiovascular diseases [2]. Moreover, nTyr is shown to be elevated in patients with mild asthma who are not undergoing corticosteroid therapy, but nTyr levels are reduced in those receiving therapy [4]. While nTyr is not detected in healthy plasma, it is elevated (10-60 μM) in diseases, such as renal failure [5]. Hence, monitoring nTyr level selectively is of interest, and differentiating this modification from a parent Tyr or from other type of post-translational modification is of importance. For example, the phosphorylation of Tyr (pTyr) involves the transfer of a phosphate group from adenosine triphosphate (ATP) to the hydroxyl group of Tyr by a protein kinase, and is involved in the cell signaling [6]. The overexpression of protein kinases and subsequent aberrant phosphorylation has been linked to cancers and neurodegeneration [7]. Given the distinct role of nTyr, it is crucial to develop effective analytical methods for selective detection and monitoring of nTyr compared to other Tyr analogues.

Current methods of detecting Tyr and its analogues include tandem mass spectrometry [8], chromatography [9], electrochemical methods [10], and spectrophotometry, among others [11,12,13,14]. Specifically, a detection of Tyr and analogues using the fluorescence spectroscopy has been explored using nanomaterials. For example, the detection of nTyr, free amino acid, was reported by using zeolitic imidazolate framework (ZIF-8) [15], and sol-gel optical sensor doped with dinuclear platinum complex [16]. Alternative nanomaterials, such as fluorescent carbon dots (CDs), are easy to synthesize, exhibit low toxicity and offer versatile photophysical properties,

making them useful for a variety of applications [16-19]. Fluorescent CDs have been used for detection of toxic metal ions [20,21], drugs [22,23], and amino acids (aspartic acid, cysteine, and phenylalanine) [24-27]. Of interest are fluorescent CDs capable of detecting and differentiating nTyr from Tyr and pTyr. Tyr was detected with the fluorescent CDs and potassium triiodide, however, nTyr and pTyr were not measured [28]. The green, fluorescent CDs were used for detection of nTyr, however this sensor required the molecularly imprinted polymer and exhibited a long response time [29]. Alternative fluorescent CDs, which exhibit high selectivity, sensitivity, and rapid response, are needed for detection of nTyr and differentiation from other Tyr analogues.

Herein, we evaluated the use of dual-fluorescent CDs, for the selective detection of nTyr against its analogues, Tyr and pTyr, using fluorescence and UV-vis spectroscopy. The aim of this study was three-fold: first, to understand the role of Tyr and its analogues on the photophysical properties of CDs; secondly, to determine the role of pH on the interactions between CDs and Tyr analogues, and lastly to validate the application of CDs for nTyr detection in biologically complex mixture, and in the presence of interferents. The zeta potential, lifetime, and electrochemical measurements were used to evaluate the mechanism of quenching. Data indicate that the dual-fluorescent CDs are promising sensing platforms for selective detection and quantification of nTyr, which holds great promise in disease biomarker detection.

2.2 Experimental section

2.2.1 Synthesis of carbon dots (CDs)

Carbon dots (CDs) were synthesized using a microwave-mediated one-step reaction with glutathione and formamide. Briefly, a 20 mL solution of 0.1 M glutathione in formamide was prepared and sonicated until the solution was clear. The mixture was then transferred to a 35 mL microwave reaction vial and heated to 180 °C for 5 min. Once cooled, the dispersion was dialyzed

using a cellulose ester dialysis membrane (molecular weight cut-off = 3.5-5.0 kDa) to remove unreacted materials and fluorophores. After, the sample was further purified through filtration (0.2 μm nylon filter) to remove any large aggregates. Subsequently, the samples were washed twice with acetone and twice with ethanol (1:10, sample: solvent volume ratio) to remove the remaining impurities). After each wash, the precipitate was collected. The resulting material was then dried in the oven at 70 °C overnight. The CDs were characterized by using Fourier-transform infrared spectroscopy (FT-IR) and powder X-ray diffraction (XRD). FT-IR spectra were collected using a Thermo Scientific Nicolet iS5 equipped with an iD5 ATR accessory. Spectra were collected using 64 scans, with a resolution of 0.4 cm^{-1}, a gain of 1, an optical velocity 0.4747 and an aperture setting of 100. The data was processed using the Omnic 9 software package. The XRD analysis for the carbon dots was carried out using a 2nd Gen D2 Phaser X-ray diffractometer (Bruker AXS). Diffraction patterns were acquired using a Cu Ka source. The scan range was set from 10 to 80º with a step size of 0.05º and an integration time of 2 s.

2.2.2 Amino acid and CDs solution preparation

The 2 mM stock solutions of each amino acid were prepared from solid in deionized water and stored at 5 °C. A 6 mM stock solution of nTyr was prepared from solid in deionized water and stored at 5 °C. The 0.0033 mg/mL CDs solution was made in a buffer freshly from the CDs powder.

2.2.3 Buffer solution preparation

The MES Buffer, pH 6.8 was prepared using 50 mM MES, 0.5 mM EDTA, and 100 mM NaCl. The pH was adjusted to 3, 6.8 or 10 by adding NaOH or HCl.

2.2.4 CDs and amino acid titrations

Prior to titration, 3 mL of 0.0033 mg/mL CDs solution in a buffer was freshly prepared and measured using UV-vis and fluorescence spectroscopy. For titration experiments, 8 μL aliquot,

followed by 9 consecutive 16 µL aliquots of specific amino acid were added to the CDs solution. After each addition, the sample was mixed and then promptly measured. The final concentrations of amino acid were 0.005, 0.015, 0.035, 0.045, 0.055, 0.0065, 0.0075, 0.085, 0.095 and 0.105 mM, unless otherwise mentioned. The final concentration of CDs was 0.0033 mg/mL. For pH dependent measurements, the MES Buffer used was at pH 3, 6.8 and 10. Control solutions were tested including amino acids alone, CDs alone, and the MES buffer only. All solutions were measured using fluorescence and UV-vis in triplicates. The data are reported as average triplicate measurements and error bars represent the standard deviation.

2.2.5 Matrix sample preparation

The equine serum matrix was prepared by diluting the stock solution by 10x in water. Prior to measurements, 100 µL of 0.0033 mg/mL CDs solution in 10x diluted equine serum was freshly prepared and 6.6 µL of 6 mM nTyr was added to 10x diluted equine serum. The control sample was 6.6 µL 10x diluted equine serum without any nTyr.

Bovine serum albumin (BSA) matrix was prepared by dissolving solid in water to a final concentration of 1 mg/mL. Prior to measurements, 100 µL of 0.0033 mg/mL CDs solution in 1 mg/mL BSA was freshly prepared and 6.6 µL of 6 mM nTyr was added. The control sample was 6.6 µL of 1 mg/mL bovine serum albumin without any nTyr.

Artificial saliva was used as undiluted. Prior to measurements, 100 µL of 0.0033 mg/mL CDs in undiluted artificial saliva was freshly prepared and 6.6 µL of 6 mM nTyr was added. The control sample was 6.6 µL of undiluted artificial saliva without any nTyr.

2.2.6 Interference Studies

All interferent solutions were prepared from solids and were dissolved in water; the final concentration of each is listed in Table S1. Prior to measurements, 3 mL of 0.0038 mg/mL CDs

solution in MES buffer, pH 6.8, was freshly prepared and 152 μL of mixture containing the 2 mM of each Tyr, pTyr and nTyr was added. For measurements with interferents, 100 μL of 0.0033 mg/mL CDs solution in MES buffer, pH 6.8 was freshly prepared and various interferents were added to obtain the final concentration listed in Table S1. The mixture was promptly measured. Next, 6.6 μL of 6 mM nTyr was added and the solution mixed and measured promptly.

2.2.7 Fluorescence spectroscopy

The fluorescence spectra of the samples were recorded using the Varian Cary Eclipse Fluorescence Spectrophotometer. The fluorescence emission spectra (430 - 800 nm) were obtained at an excitation wavelength of 420 nm using 1 cm quartz cuvette at a scan rate of 600 nm/min, 1 nm data interval and 5 nm slit. The total volume of the sample was 3000 μL. The fluorescence spectra of the samples were recorded using BioTek Cytation 5 in CORNING 96-well clear microplates. The total volume of the sample was 100 μL. Endpoint measures were obtained at an excitation wavelength of 420 nm and an emission wavelength of 679 nm. Triplicate experiments were carried out.

2.2.8 UV-vis absorbance spectroscopy

The UV-vis absorbance spectra (200 - 800 nm) were recorded using UV-2550 UV-vis spectrophotometer (Shimadzu) in a 1 cm quartz cuvette at a fast speed, 1 sampling interval and 2-nm bandwidth. The total volume of the sample was 3000 μL.

2.2.9 Zeta potential measurements

The zeta potentials were measured in a disposable folded capillary cell using a Zetasizer Nano ZS (Malvern Panalytical). An average of 3 readings were used for analyses, and data were collected in duplicates.

2.2.10 Fluorescence lifetimes measurements

The fluorescence lifetimes were acquired using an EasyLife X fluorescence lifetime system (Optical Building Blocks Corporation). The spectra were collected in a 1-cm quartz cuvette, using a 368-nm pulsed picosecond LED excitation source. An emission slit width of 1.5 mm, 500 channels, 0.25 s integration time and an average of 3 readings were used for analysis. The data were processed and analyzed using the OBB EasyLife X software and collected in duplicates.

2.2.11 Electrochemical measurements

The cyclic voltammetry (CV) measurements were acquired using the Autolab PGSTAT302N by Metrohm AG, and a standard 3-electrode system consisting of a glassy carbon working electrode, a Ag/AgNO$_3$ reference standard electrode, and a platinum wire as the counter electrode. The potential range was set from -1.5 V to 1.5 V at a scan rate of 100 mV/s and swept from a positive direction. A solution of 0.0033 mg/mL CDs in 0.1 M TBAF and ACN was used for electrochemical measurements. The control samples tested include: ACN only, and TBAF only solutions. The nTyr solution (1 mM) was measured in the phosphate buffer saline, pH 7.4, with the glassy carbon electrode, Ag/AgCl reference electrode, and platinum wire as the counter electrode.

2.3 Results and discussion

2.3.1 Synthesis and characterization of dual fluorescent carbon dots

Dual-fluorescent carbon dots (CDs) were prepared in a one-step microwave-assisted reaction using formamide and glutathione as previously reported [21]. Transmission electron microscopy (TEM) images of the CDs (Figure 2.1A) show that the dots are monodispersed with the Gaussian size distribution spanning 3 - 13 nm with an average size distribution of 7.8 ± 2.2 nm (Figure 2.1A inset), and lack crystallinity. As shown in Figure 1B, there is an absence of crystalline reflection

with an amorphous halo spanning 10-80° 2θ in the X-ray diffraction pattern, which is expected in such materials. In addition, the lack of the peak centred at 27° 2θ is characteristic of the (002) diffraction plane of graphitic structures [22-24]. The FT-IR spectrum shows a broad peak at 3000-3500 cm⁻¹, indicative of the O-H and N-H stretching vibrations that stem from the hydroxyl/carboxyl and amine groups (Figure 2.1C).
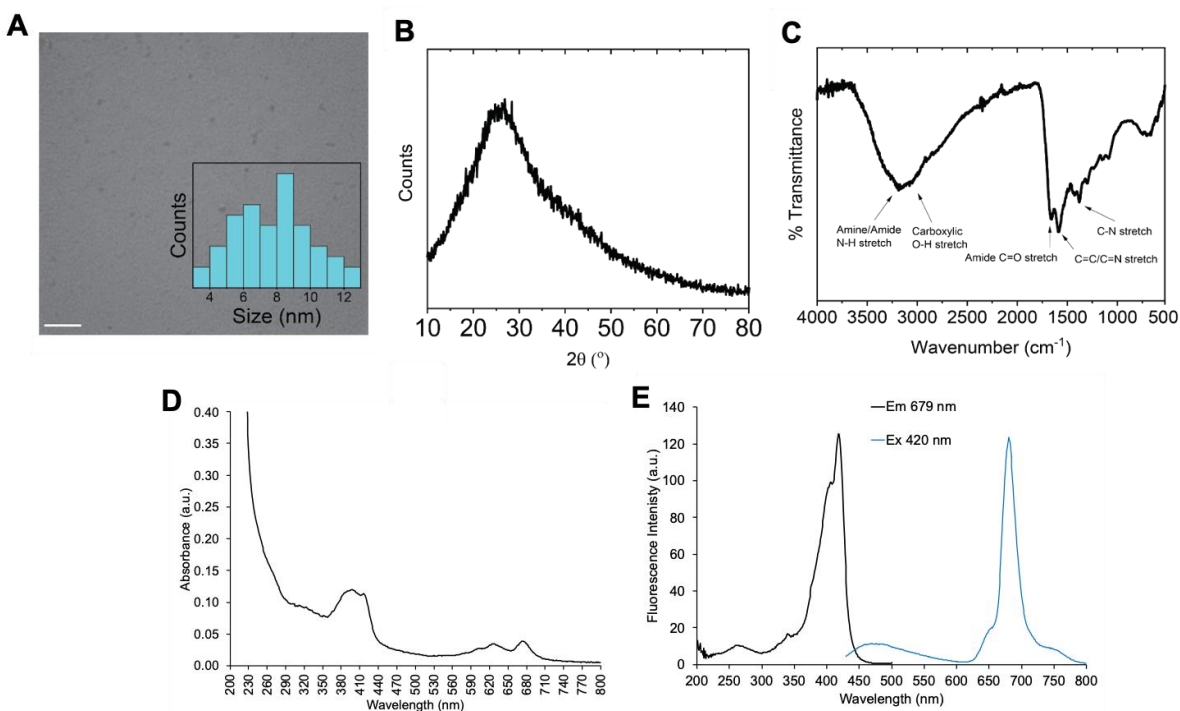
Figure 2.1. (A) TEM image of the CDs dispersion in water. The calculated particle diameter is 7.8 ± 2.2 nm. Inset: Gaussian size distribution spanning 3-13 nm; (B) XRD pattern of the CDs highlighting an amorphous halo in the range of 10-80° 2θ; (C) FTIR spectrum of CDs highlighting the presence of amide and carbonyl functional groups; (D) UV-vis and (E) fluorescence emission and excitation spectra of CDs ([CDs] = 0.033 mg/mL; MES Buffer, pH 6.8).

The presence of amide bonds is confirmed with stretches at 1655 cm^{-1} and 1359 cm^{-1}, which are attributed to the C=O and C-N stretches, respectively. The peak at 1574 cm^{-1} is assigned to the presence of C=C/C=N bonds. To explore the application requirements of CDs in a biological setting, the optical properties were investigated in MES Buffer, pH 6.8, to reflect the pH of neurons. UV-vis absorbance spectroscopy highlighted three distinct absorbance bands for CDs at 290-350 nm, 370-450 nm and 590-690 nm (Figure 2.1D). The first band is ascribed to the π-π* transition of CDs [30], while the second band corresponds to the n-π* transition of C=O/N-H groups in CDs. The bands in the 590 - 690 nm region are assigned to n-π* transitions due to the presence of polar surface groups such as C=N, C=O and C=S groups in CDs [31-33]. Interestingly, following excitation at 420 nm, the dots exhibited two fluorescence emission bands: the first is centered at 480 nm (blue emission) and the second at 679 nm (red emission) with a shoulder at 650 nm (Figure 1E). This unique fluorescence signature is linked to the inner and outer core of the CDs [34-37]. Briefly, the red fluorescence stems from the molecular states, which are predominantly on the surface of CDs. The blue fluorescence stems from the carbogenic core of the dots [34-37]. The excitation spectra (Figure 1E) were also collected for inner and outer core fluorescence emissions. The emission at 480 nm resulted in the excitation spectrum with two major peaks at 239 and 383 nm. The excitation spectrum from the 680 nm was characterized by 262, 405 and 420 nm excitation bands, with the major peak at 420 nm.

2.3.2 Role of Tyr analogues on the photophysical properties of carbon dots

To understand the interactions between CDs and amino acids, nTyr, pTyr and Tyr, and the role that they play on the optical properties of CDs, the UV-vis and fluorescence spectroscopies were used. An excitation wavelength at 420 nm was applied based on the absorbance and excitation spectra of CDs, and fluorescence emission measured in the 430 - 800 nm range. Figure 2 shows

the fluorescence emission spectra of CDs with increasing concentrations of Tyr, pTyr and nTyr from 0 - 0.105 mM. These concentrations were chosen based on the reported biological concentrations of tyrosine analogues [38]. No change in the fluorescence emission intensities of CDs were observed for Tyr (Figure 2.2A) and pTyr (Figure 2.2B).
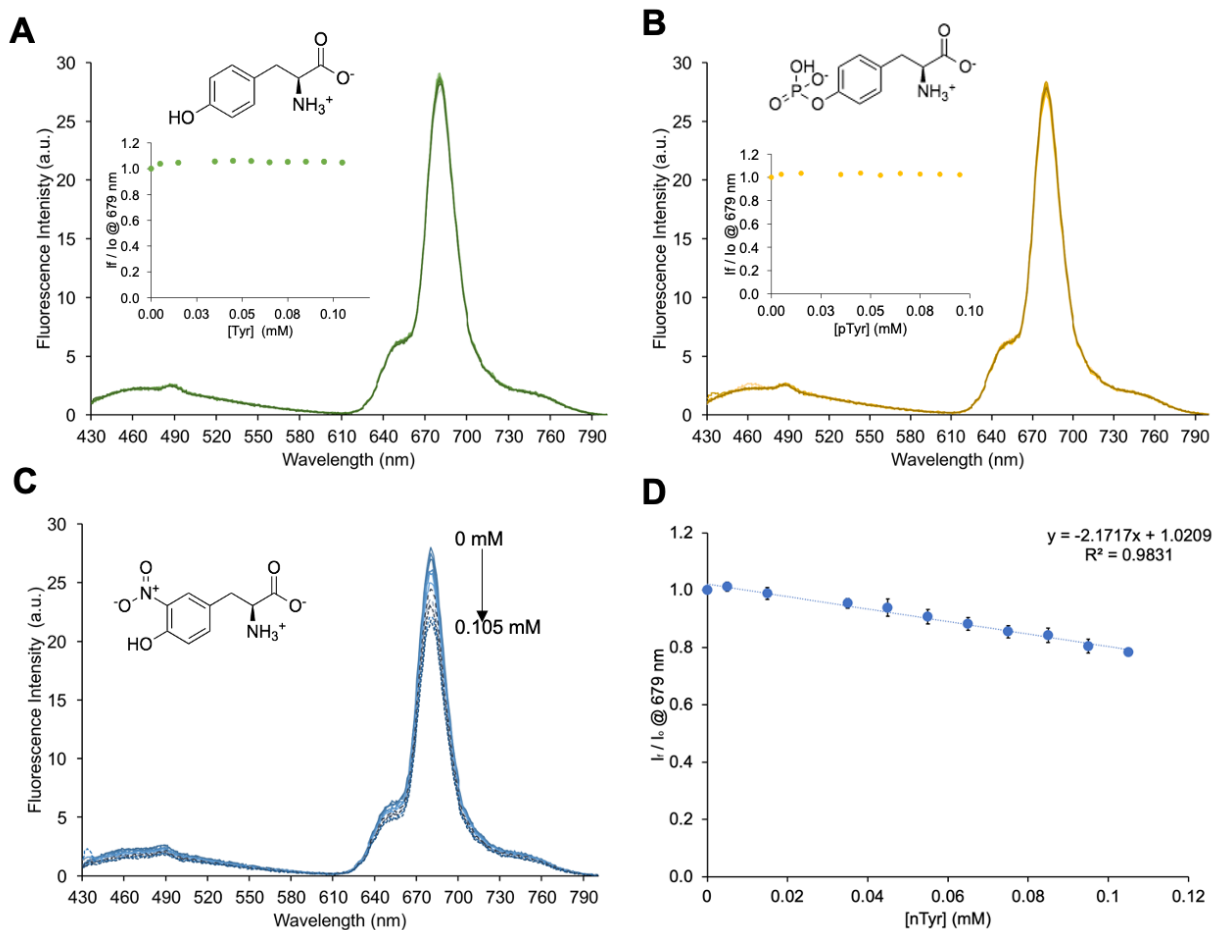

Figure 2.2. Fluorescence emission spectra of CDs as a function of (A) Tyr, (B) pTyr, (C) nTyr concentrations; (D) Plot of I_f/I_o fluorescence emission @ 679 nm as a function of nTyr concentrations (insets show I_f/I_o fluorescence emission @ 679 nm; [CDs] = 0.0033 mg/mL; [amino acid] = 0 - 0.105 mM; MES Buffer, pH 6.8; 420 nm excitation wavelength).

As demonstrated in Figure 2.2C, the nTyr quenched the fluorescence emission intensity at 679 nm. The plot of fluorescence emission intensity at 679 nm, Figure 2.2D, indicated a decrease in the signal as the concentration of nTyr increased. The linear decrease observed with nTyr addition was fitted to a straight-line fit with a slope of -2.17 and an R^2 value of 0.98. The fluorescence quenching of ~ 22% was observed with nTyr whereas quenching was not observed with other amino acids tested. At a higher nTyr concentration (0.304 mM), 55% quenching was observed (Figure S2A-B). Other emission peaks, 480 nm and 650 nm, also decreased in the presence of nTyr, with similar quenching changes to the 679 nm band (Figure S3). The plot of I_{679}/I_{480} as a function of amino acid concentrations, indicated no change in the ratio (Figure S4) indicating that the nTyr quenched outer and inner core fluorescence equally. The limit of detection (LOD) and the limit of quantitation (LOQ) were determined from the plot of fluorescence intensity (679 nm) versus nTyr concentration (Figure 2.2D) to be 34 µM and 137 µM, respectively.

The fluorescent CDs were also tested in equine serum (10x diluted), artificial saliva (undiluted or diluted), and bovine serum albumin solution in order to determine if the assay was amenable to the biologically relevant matrices. In all the complex mixtures tested, the sensitivity for nTyr was not compromised and remained at ~45%, regardless of matrix used (Figure 2.3A). Additionally, the spiked undiluted artificial saliva samples with various nTyr concentrations were also tested and the sensor performance was similar to that in the buffer (Figure S5).
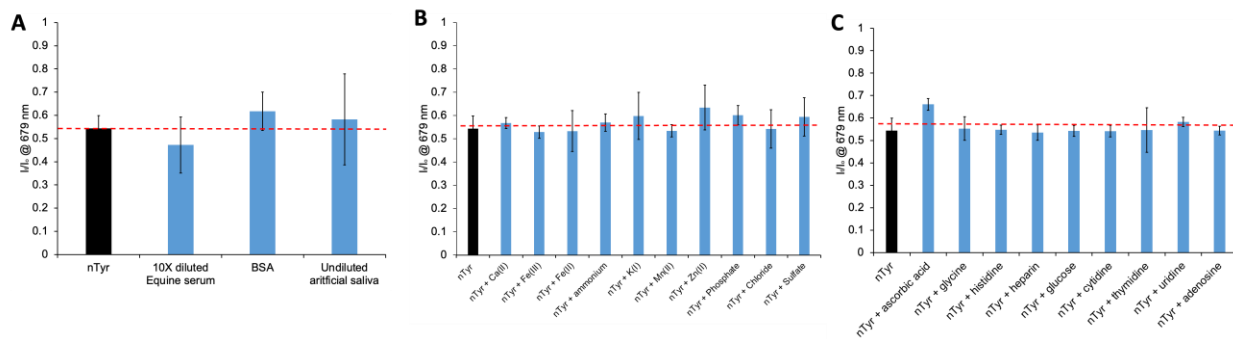
Figure 2.3. Selectivity test for detection of nTyr in a complex mixture or in the presence of interferents. The average of I_f/I_o at emission peak at 679 nm of CDs with nTyr in the presence of (A) various common biological matrices: equine serum (10x diluted), bovine serum albumin and undiluted artificial saliva ([BSA] = 1 mg/mL), (B) cations and anions, and (C) amino acids, nucleosides and other organics ([CDs] = 0.0033 mg/mL; [nTyr] = 0.3 mM; see Table S1 for concentrations of various interferents).

In addition, the interference studies were carried out in the copresence of all three Tyr-based amino acids (nTyr, pTyr, and Tyr at equimolar concentrations), and the nTyr detection was achieved without any loss of sensitivity (Figure S6). To further expand the utility of the CDs for nTyr detection, other interferences were also tested. For example, nTyr was detected even in the presence of various metal cations (Ca(II), K(I), Fe(II), Fe(III), Mn(II) and Zn(II)), organic anions and cations (ammonium, chloride, phosphate, and sulfate), and neutral organic compounds (amino acids (Gly and His), nucleosides (adenosine, cytidine, thymidine, and, uridine), ascorbic acid, glucose, and heparin (Figure 2.3B-C). The interference studies indicated that the CDs are ideally suited for detection of nTyr even in the presence of other biologically relevant molecules. The fluorescence emission of CDs was quenched to a small extent (~10% quenching) (Figure S7) in the presence of various interferents, without nTyr, indicating selectivity for nTyr.

To understand the quenching mechanism of nTyr addition, the Stern-Volmer plot was used (Figure S8) [39]. The Stern-Volmer plot was mostly linear, at low nTyr concentrations, but with a slight positive curvature, concave towards the y-axis, as the concentration of nTyr increased, pointing to the combination of the static and dynamic quenching. Dynamic quenching does not lead to a complex formation between fluorophore and a quencher, rather it affects the excited state of a fluorophore, rendering it non-emissive. The Trp, Tyr and Phe may induce both types of quenching. These amino acids induced dynamic quenching in the presence of silver nanoparticles, while the static quenching was observed with the green, fluorescent gold nanoparticles [40,41]. Stern-Volmer plot (Figure S8) shows the experimental data fitted to the Eq. S3 for both static and dynamic quenching [42], from which the static, K_s, and dynamic, K_d constant were determined to be 1000 M^{-1} and 2100 M^{-1}, respectively. The experimental data was also fitted to a model for a purely dynamic quenching, however, the fitting was not perfect due to the combination of static and quenching pathways. Hence, nTyr quenched CDs *via* both static and dynamic quenching mechanisms, with the latter being the more prominent pathway, due to its greater quenching constant. However, using the linear Benesi-Hildebrand plot, which assumes the static quenching [42-43], the binding constant, K_b, the number of binding sites, N, and R^2 values of 1.09 x $10^5\,M^{-1}$, 1.3 and 0.9955, respectively, were determined (Figure S9). The fluorescence lifetime is an important parameter to consider when evaluating the quenching mechanism and can often give an indication if the process is due to dynamic or static quenching. Unlike for static quenching, the lifetime of a fluorophore is likely to be changed in the presence of a quencher when dynamic quenching is taking place. The fluorescence lifetimes were measured before and after the addition of amino acids (Table S2). The long component, 3.72 ± 0.57 ns (lifetime 2), was associated with the blue fluorescence (core states) and the short component (lifetime 1) 0.57 ± 0.21 ns was linked

to the red fluorescence (molecular states) of CDs [47]. Slight changes in the lifetimes 1 and 2 were observed for Tyr and pTyr, however, no change in the blue or red fluorescence was evident. The increase in lifetime 2 for Tyr and pTyr is less significant due to the large error bars associated with duplicate measurements. Hence, the lifetime 2 change, alongside negligible fluorescence emission change, indicates that no quenching occurred with those amino acids. By contrast, the decrease in lifetimes 1 (0.35 ns ± 0.30) and 2 (3.05 ns ± 0.10) with nTyr as well as decrease in the blue and red fluorescence emission indicated that the mechanism of quenching may be dynamic rather than solely static, or combination thereof [24]. At low nTyr concentrations (<105 μM), the Stern-Volmer plot was linear (Figure S8B) which allowed for determination of quenching rate constant, k_q, by using the lifetime value [48]. Using the Eq. S2, the k_q value was determined to be 472 x 10^{10} L mol^{-1} s^{-1}, which is on the order of diffusion-controlled value. The change in lifetimes was also observed during fluorescence enhancement of CDs with Phe, which was indicative of dynamic quenching [49]. The static quenching typically leads to a shifted spectrum in emission and/or absorption. If the fluorescence decrease of CDs is caused mostly by dynamic quenching, then a decrease in lifetime is expected [50]. The dynamic quenching with nTyr was further supported by the absence of changes in the UV-vis spectrum of CDs with nTyr, as nTyr affected the excited state of CDs rather than the ground state [51]. When the excited state of CDs returns to the ground state by the collision between the quencher, the dynamic quenching takes place with the mechanism of energy transfer or the mechanism of charge transfer [51]. Based on the fluorescence emission and UV-Visible absorbance data, both static and dynamic quenching mechanisms take place with nTyr.

The excitation at 420 nm did not lead to any emission due to Tyr, pTyr or nTyr alone, and these amino acids did not contribute to the fluorescence emission observed (Figure S10). However,

when ~270 nm excitation wavelength was used, then the fluorescence emission was observed at ~300 nm for Tyr and pTyr alone (Figure S11 A-B). This was indicative of the fluorescent nature of Tyr and pTyr. By contrast, the nTyr did not exhibit any fluorescence even after excitation at 277 or 374 nm (Figure S11 C-D). The excitation of CDs alone at 271 nm, resulted in a low emission and a significant emission peak at 447 nm, and a small peak at 679 nm (Figure S12C), which was in stark contrast to the excitation at 420 nm, indicating excitation dependent fluorescence emission profile (Figure S12A). Using the 270 nm as an excitation, Tyr and pTyr did not quench the CDs (Figure S13), but nTyr did (Figure S14). Again, the data indicated that the excitation at either 277 nm or 420 nm resulted in the quenching of the CDs fluorescence. When 650 nm excitation was used, nTyr did not result in significant quenching of emission at 680 nm, which was indicative of the importance of absorbance of nTyr in the quenching mechanism (Figure S15).

In addition to fluorescence spectroscopy, UV-vis analysis was also used to evaluate photophysical changes upon amino acid titrations. The UV-vis absorbance spectra of the CDs following the addition of amino acids was predominated with amino acid bands. Compared to other compounds, the nTyr exhibited three distinct peaks seen at 232, 279 and 376 nm (with a shoulder at 420 nm), resulting in a yellow-coloured solution (Figure S16A). The absorbance band in the visible range, 250 - 450 nm, of nTyr was dependent on the solution pH [44-45]. At acidic pH, the absorbance maximum was located at ~ 370 nm and at alkaline pH, the peak shifted to 440 nm (Figure S16A). The pH-dependent shift of nTyr may be ascribed to the ionization of the phenol group which causes the large red shift in absorptivity. Hence, nTyr was predominantly present as a phenol, and a small contribution of phenolate anion, at the pH used (6.8). Notably, all amino acids tested had the peaks below 320 nm due to the *n*-π and π-π* electronic transitions of amino acids, but only nTyr absorbance overlapped with the emission of CDs at 480 nm [46]. Hence, the

overlap of nTyr absorbance with the emission band of CDs at 480 nm may contribute to the quenching mechanism observed at the specific emission wavelength. This overlap was absent for the Tyr or pTyr amino acids, which did not quench CDs.

In order to understand the surface interactions between the CDs and amino acids, zeta potential measurements were obtained (Table S3). The CDs had an overall negative net charge (-26.0 mV ± 5.83) ascribed to the negatively charged groups on the surface, such as deprotonated carboxylic acids and thiols. However, the positive charges were also reported on CDs, ascribed to the functional groups such as protonated amines [35,36,47]. The addition of nTyr, Tyr and pTyr amino acids resulted in a less negative zeta potential values, -22.4 mV ± 5.23, -24.2 ± 3.79 and -25.4 mV ± 0.54, respectively. While the greatest decrease in negative charge was observed with nTyr, compared to other amino acids, the electrostatic interactions may not solely contribute to the quenching mechanism, since both Tyr and nTyr are predominantly neutral at pH 6.8.

2.2.3 Role of pH on the interactions between CDs and amino acids

Given the relationship between solution pH and pK_a, and the ionizable nature of amino acids and CDs, it is important to understand how pH may affect quenching. The CDs have different functional groups which include -OH, -COOH, and $-NH_2$ on the surface which could form a series of energy levels in surface states, as a function of ionization [52], but remain fluorescent at various pH values tested. The pKa values of an amino acid are highly dependent on the post-translational modifications. For example, the pKa of the phenolic hydroxyl group of Tyr is ~10, but decreases dramatically to ~7.0 following the nitration to generate nTyr [49]. By changing the pH from 6.8 to 3, the net charge of the tested amino acids remains unchanged, but at pH 10, Tyr and nTyr both have a negative charge of -2, while pTyr has a negative charge of -3 (Figure S16B). Hence, if the electrostatic interactions solely govern the effects of amino acid on CDs fluorescence, then it

would be expected that Tyr and nTyr both being neutral at pH 6.8 would produce identical effects. However, this was not the case. The charge of amino acid may not be the major contributing factor in the fluorescence quenching mechanism. At pH 3, no quenching by Tyr or pTyr was observed, and only a small decrease was seen with nTyr, as shown in Figure 4A. The quenching by nTyr was evident at pH 10 (Figure 4B). Figure 4C shows that the quenching increases with the increase in pH, with the greatest quenching (38%) at pH 10; however, this trend is not observed for Tyr or pTyr (Figure S17). The pH-dependent trend cannot be ascribed to ionic interactions or H-bonding, solely, rather photophysical properties of the nTyr may contribute to its quenching efficiency.
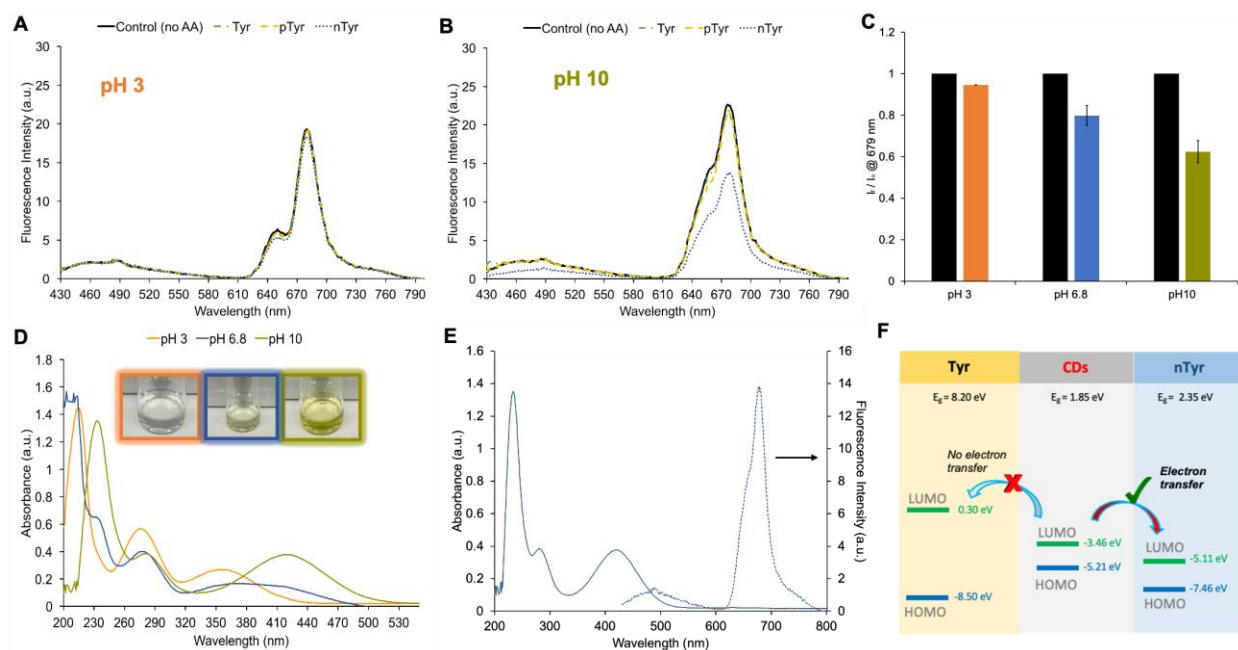

Figure 2.4. Fluorescence emission spectra of CDs in MES buffer at (A) pH 3 and (B) pH 10 after the addition of Tyr, pTyr and nTyr; (C) Plot of I_f/I_o @ 679 nm as a function of pH and in the absence (back bar) and presence (coloured bars) of nTyr; (D) UV-vis spectra of nTyr at various pH values; (E) UV-vis spectrum of nTyr (pH 10) and emission spectrum of CDs (pH 10); (F) Energy levels and energy gaps for CDs, Tyr and nTyr (pH 10), and the schematic illustration of

electron transfer quenching mechanism ([CDs] = 0.0033 mg/mL; [amino acid] = 0.105 mM; 420 nm excitation wavelength).

To understand and characterize the photophysical properties of nTyr at various pH values, the UV-vis spectra were collected (Figure 2.4D). At pH 3, the solution was colourless which suggested the presence of a non-ionized phenol hydroxyl group [49]. However, as pH increased to 10, a prominent yellow colour developed due to a new peak at 420 nm, which was associated with the presence of a phenolate anion [49]. The absorbance at 420 nm is significant as it was the excitation wavelength used to excite CDs in all the measurements, and nTyr absorbance overlaps with the CDs emission at 480 nm (Figure 2.4E). The greater the absorbance at 420 nm, the greater the overlap with fluorescence emission of CDs (at 480 nm) and greater the observed quenching of the CD. Data indicate that the quenching mechanism was due to the energy transfer between CDs and nTyr. In addition, the quenching was not due to the collision between CDs and nTyr, which would produce the non-fluorescent ground state complex as was observed for CDs with aspartic acid [24]. For example, the intermolecular charge transfer (ICT) between surface groups of CDs and aspartic acid was mediated by H-bonding. The selective quenching by nTyr may be ascribed to the fluorescence resonance energy transfer (FRET) between the CDs (energy donor) and nTyr (energy acceptor), as was reported for the quenching mechanism of CDs by nitrophenol [52,53,54,55]. The CDs are well known to exhibit fluorescence emission from S to ground state due to the core and also undergo Intersystem charge transfer (or intersystem crossing) from S to T state leading to fluorescence associated with the surface states [56]. In this case, the nTyr may serve as an S1 or T1 state quencher. One possible mechanism of quenching is the quenching of the triplet (T) state resulting in a non-emissive transition to a ground state. The quenching data indicate

that both fluorescence emission transitions, from S (core-blue) and T (surface states-red) are quenched by nTyr. Although in nTyr, the two lowest triplet states (T1 and T2) are close in energy with S1, the intersystem crossing probability remains low due to the El-Sayed rule and a small crossing region [57]. Recent evaluations of excited-state potential energies of anionic 3-nitrotyrosine showed that intersystem crossing from the S1 to the T1 or T2 states is unlikely [57]. Since nTyr is non-emissive it may serve as the "molecular ruler" as the energy transfer is innately dependent on the distance between donor and acceptor, which is subject to the inverse sixth-power distance dependence within a point dipole−dipole approximation of both the donor and acceptor molecules [57]. Tyr, which is colourless, did not lead to quenching of quantum dots [52]. Hence, similarly in this work, the colourless solutions of Tyr and pTyr did not absorb at 420 nm (Figure S16B), and hence no overlap with the CDs emission and no quenching was observed. The FRET may explain the quenching of emission at 480 nm by nTyr, but it does not explain the quenching of emission at 679 nm, due to the lack of overlap between donor emission and acceptor absorbance. Rather, a photoinduced electron transfer from the excited state of CDs to nTyr may be responsible for the fluorescence quenching at 679 nm [55]. To further investigate this mechanism of quenching, the electrochemical method, cyclic voltammetry (CV), was used. The CV of the CDs was characterized by several anodic peaks in the -0.2 - 1.2 V potential range, and a single cathodic peak at -1.25 V (Figure S18). Overall, CDs exhibited irreversible oxidation. The HOMO and LUMO energy levels of CDs were calculated from CV measurements, as previously reported, and HOMO was determined from the optical energy band gap, E_g [60, 62, 63]. Using the longest absorbance onset of 460 nm of CDs, the E_g was determined to be 2.69 eV, and the HOMO was calculated to be -6.15 eV. From the CV, the LUMO was calculated to be -3.46 eV. The HOMO and LUMO levels observed for dual fluorescing CDs were similar to those synthesized from

chloroform and o-phenylendiamine (HOMO and LUMO values at -6.3 eV and -3.82 eV, respectively) [58]. When the longest absorbance edge at 679 nm was used, the E_g and HOMO were found to be 1.75 eV and -5.21 eV, respectively (Figure 2.4F). The HOMO and LUMO levels of Tyr were reported to be ~ -8.5 and ~0.3 eV, respectively, with an energy gap of 8.20 eV, and were similar to pTyr (Figure 2.4F) [61]. By contrast the E_g gap reported for nTyr was 4.61 eV, and much smaller than the other amino acids [60,61]. Specifically, the HOMO and LUMO levels of nTyr were determined computationally to be -6.8 and -2.23 eV, respectively [62]. In all cases, the LUMO level of CDs was lower than the LUMO levels of amino acids, indicating that the excited electrons from LUMO of CDs may not be easily transferred to the LUMO of amino acid. However, the UV-vis spectra of nTyr clearly showed stronger quenching when nTyr existed in predominantly deprotonated form. Using the UV-vis measurements, the experimental E_g gap was determined for nTyr at pH 3, 6.8, and 10 (calculated from the absorbance onset) to be 2.85, 2.52, and 2.35 eV, respectively. An increase of the solution pH resulted in the decrease of the band gap. Hence, the deprotonated nTyr had a smaller energy gap than the neutral nTyr. With regards to the HOMO and LUMO of deprotonated nTyr, both orbitals were delocalized on the phenolic ring and nitro group in the anionic nTyr [63]. A noticeable charge transfer was reported between the phenolate oxygen to nitro group of anionic nTyr when excitation at 400 nm was used. Hence, for deprotonated nTyr, the LUMO level may be much lower than for nTyr. The electrochemical method was used to determine oxidation potential of nTyr at various pH values (Figure S19). At pH 10, it was experimentally determined that the HOMO and LUMO levels were at -7.46 and -5.11 eV, respectively (Figure 2.4F). Hence, the excited electrons from the LUMO level of CDs are more likely to transfer to the LUMO of anionic nTyr, an electron acceptor, resulting in electron transfer, and nonradiative deactivation, i.e. quenching. This is not possible with other amino acids tested.

In conclusion, both energy transfer and nonradiative deactivation by electron transfer were likely mechanisms which contributed to the quenching (combination of static and dynamic) of CDs fluorescence by nTyr. The outer core fluorescence was sensitive to the nonradiative deactivation by energy transfer while the inner core fluorescence was sensitive to the energy transfer.

The CD selectivity for nTyr was due to the overlapping electronic transitions between the analyte and a probe which allowed for quenching via energy transfer and electron transfer to take place. Since the electronic transitions of Tyr and pTyr were not favourable, no overlap with CDs emission band or LUMO level was possible, hence no quenching was observed. The dramatic differences in the photophysical properties of various Tyr analogues is what resulted in the selectivity observed with CDs.

The optical methods for detection of nTyr based on nanomaterials have been previously reported (Table S4). For example, nanomolar detection of nTyr was achieved by using fluorescence assays based on the binuclear Pt-2-pyrazinecarboxylic acid (pca)-Bipyridine (bpy) complex doped in sol-gel matrix [16] or hybrid material (AuNCs@ZIF-8) synthesized by encapsulating gold nanoclusters (AuNCs) into the zeolitic imidazolate framework (ZIF-8) [15]. Application of CDs for nTyr detection is scarce [29]. The bio-inspired molecularly imprinted polymer was used as a receptor for nTyr, while the green emitting carbon dots (CDs) were used as signal transducer [29]. In the present study, CDs served as a receptor for nTyr as well as the signal transducer, which has not been demonstrated before. In addition, the current assay provided the LOD value (34 μM) which was within the biological range for nTyr detection (10 - 60 μM) in diseased samples [4-5]. The dual-purpose CDs are beneficial as they reduce a need for extra

reagents or supplies while providing a measurable signal and selectivity for nTyr, over other congeners.

2.4 Conclusion

The dual-fluorescing CDs were sensitive to nTyr rather than other biological analogues, such as Tyr or pTyr. The quenching phenomena by nTyr was ascribed to a combination of the nonradiative energy and electron transfer mechanisms. This study showcases the application of CDs as fluorescent sensors capable of differentiating post-translational modifications of amino acids. Such sensors may be applied for detection and monitoring of disease-related biomarkers by synthetically tailoring the chemical composition of CDs, and their photophysical properties. The CDs with a single fluorescence emission which overlaps more efficiently with the absorbance of a biomarker will likely result in a highly sensitive probe. In addition, the specific hydrogen bonding or ionic interactions between the surface of CDs with a biomarker will improve selectivity over other similar congeners or interferants.

2.5 Acknowledgements

2.6 References

[1] M.P. Kummer, M. Hermes, A. Delekarte, T. Hammerschmidt, S. Kumar, D. Terwel,... M.T. Heneka, Nitration of tyrosine 10 critically enhances amyloid β aggregation and plaque formation, Neuron. 71 (2011) 833-844.

[2] M.H. Shishehbor, R.J. Aviles, M.L. Brennan, X. Fu, M. Goormastic, G.L. Pearce, ... S.L. Hazen, Association of nitrotyrosine levels with cardiovascular disease and modulation by statin therapy, Jama. 289 (2003) 1675-1680.

[3] R. Radi, Protein tyrosine nitration: biochemical mechanisms and structural basis of functional effects, Acc. Chem. Res. 46 (2013) 550-559.

[4] T. Hanazawa, S.A. Kharitonov, P.J. Barnes, Increased nitrotyrosine in exhaled breath condensate of patients with asthma, Am. J. Respir. Crit. 162 (2000) 1273-1276.

[5] Y. Zhang, M. Li, X. Gao, Y. Chen, T. Liu, Nanotechnology in cancer diagnosis: Progress, challenges and opportunities. J. Hema. Onc. 12 (2019) 1-13.

[6] T. Hunter, Tyrosine phosphorylation: thirty years and counting, Curr. Opin. Cell Biol. 21 (2009) 140-146.

[7] K.E. Tifft, K.A. Bradbury, K.L. Wilson, Tyrosine phosphorylation of nuclear-membrane protein emerin by Src, Abl and other kinases, J. Cell Sci. 122 (2009) 3780-3790.

[8] U. Groselj, S. Murko, M.Z. Tansek, J. Kovac, A.T. Bakija, B.R. Lampret, T. Battelino, Comparison of tandem mass spectrometry and amino acid analyzer for phenylalanine and tyrosine monitoring—implications for clinical management of patients with hyperphenylalaninemia, Clin. Biochem. 48 (2015) 14-18.

[9] D.I. Sanchez-Machado, B. Chavira-Willys, J. López-Cervantes, High-performance liquid chromatography with fluorescence detection for quantitation of tryptophan and tyrosine in a shrimp waste protein concentrate, J. Chromatogr. B. 863 (2008) 88-93.

[10] W. Gu, M. Wang, X. Mao, Y. Wang, L. Li, W. Xia, A facile sensitive l-tyrosine electrochemical sensor based on a coupled CuO/Cu 2 O nanoparticles and multi-walled carbon nanotubes nanocomposite film, Anal. Methods. *7* (2015) 1313-1320.

[11] Q. Wu, A. Fang, H. Li, Y. Zhang, S. Yao, Enzymatic-induced upconversion photoinduced electron transfer for sensing tyrosine in human serum, Biosens. Bioelectron. 77 (2016) 957-962.

[12] B.E.A. Basheir, A.A. Elbashir, Spectrophotometric methods for the determination of L-tyrosine in pharmaceutical formulations, Chem. Express. 8 (2015) 95-101.

[13] S. Roy, An insight of binding interaction between Tryptophan, Tyrosine and Phenylalanine separately with green gold nanoparticles by fluorescence quenching method, Optik. 138 (2017) 280-288.

[14] S. Roy, T.K. Das,Study of interaction between tryptophan, tyrosine, and phenylalanine separately with silver nanoparticles by fluorescence quenching method, J. Appl. Spectrosc. 82 (2015) 598-606.

[15] R. Jalili, M. Dastborhan, S. Chenaghlou, A. Khataee, Incorporating of gold nanoclusters into metal-organic frameworks for highly sensitive detection of 3-nitrotyrosine as an oxidative stress biomarker, J. Photochem. Photobiol. A. 391 (2020) 112370.

[16] T.V. de Medeiros, J. Manioudakis, F. Noun, J.R. Macairan, F. Victoria, R. Naccache, Microwave-assisted synthesis of carbon dots and their applications, J. Mater. Chem. C. 7 (2019) 7175-7195.

[17] F.R. Baptista, S.A. Belhout, S. Giordani, S.J. Quinn, Recent developments in carbon nanomaterial sensors, Chem. Soc. Rev. 44 (2015) 4433-4453.

[18] H.M. Nassef, M. Hagar, Z. Malek, A.M. Othman, Uptake of tyrosine amino acid on nano-graphene oxide, Materials, 11 (2018) 68.

[19] Z. Wang, C. Xu, Y. Lu, X. Chen, H. Yuan, G. Wei, J. Chen, Fluorescence sensor array based on amino acid derived carbon dots for pattern-based detection of toxic metal ions, Sens. Actuators B-Chem. 241 (2017) 1324-1330.

[20] F. Yarur, J.R. Macairan, R. Naccache, Ratiometric detection of heavy metal ions using fluorescent carbon dots, Environ. Sci. Nano. 6 (2019) 1121-1130.

[21] H. Dai, Y. Shi, Y. Wang, Y. Sun, J. Hu, P. Ni, Z. Li, A carbon dot based biosensor for melamine detection by fluorescence resonance energy transfer, Sens. Actuators B-Chem. 202 (2014) 201-208.

[22] K. Wang, Q. Ji, J. Xu, H. Li, D. Zhang, X. Liu, ... H. Fan, Highly sensitive and selective detection of amoxicillin using carbon quantum dots derived from beet, J. Fluoresc. 28 (2018), 759-765.

[23] P. Chauhan, J. Saini, S. Chaudhary, K.K. Bhasin, Sustainable synthesis of carbon dots from agarose waste and prospective application in sensing of l-aspartic acid, Mater. Res. Bull. 134 (2021) 111113.

[24] J. Jana, M. Ganguly, T. Pal, T, Intriguing cysteine induced improvement of the emissive property of carbon dots with sensing applications, Phys. Chem. Chem. Phys. 17 (2015) 2394-2403.

[25] J.Z. Huo, X.S. Li, J.D. An, Y. Li, G.X. Du, X.X. Wu, ... B. Ding, Photo-luminescent chiral carbon-dot@ Eu (D-cam) nanocomposites for selectively luminescence sensing of L-phenylalanine, J. Mol. Struct. 1201 (2020) 127214.

[26] S. Lu, Z. Li, X. Fu, Z. Xie, M. Zheng, (2021), Carbon dots-based fluorescence and UV–vis absorption dual-modal sensors for Ag+ and l-cysteine detection, Dyes Pigm. 187 (2021) 109126.

[27] J. Nebu, K.S. Anu, J.A. Devi, R.S. Aparna, A.O. Aswathy, G.M. Lekha, G. Sony, Pottasium triiodide enhanced turn-off sensing of tyrosine in carbon dot platform, Microchem. J. 146 (2019) 12-19.

[28] R. Jalili, M. Amjadi, Bio-inspired molecularly imprinted polymer–green emitting carbon dot composite for selective and sensitive detection of 3-nitrotyrosine as a biomarker, Sens. Actuators B-Chem. 255 (2018) 1072-1078.

[29] J. Manioudakis, F. Victoria, C.A. Thompson, L. Brown, M. Movsum, R. Lucifero, R. Naccache, Effects of nitrogen-doping on the photophysical properties of carbon dots, J. Mater. Chem. C. *7* (2019) 853-862.

[30] Y. Wang, A. Hu, Carbon quantum dots: synthesis, properties and applications, J. Mater. Chem. C. 2 (2014) 6921-6939.

[31] L. Pan, S. Sun, L. Zhang, K. Jiang, H. Lin, Near-infrared emissive carbon dots for two-photon fluorescence bioimaging, Nanoscale. 8 (2016) 17350-17356.

[32] D. Qu, M. Zheng, P. Du, Y. Zhou, L. Zhang, D. Li, ... Z. Sun, (2013). Highly luminescent S, N co-doped graphene quantum dots with broad visible absorption bands for visible light photocatalysts, Nanoscale. 5 (2013) 12272-12277.

[33] S. Zhu, Y. Song, X. Zhao, J. Shao, J. Zhang, B. Yang, The photoluminescence mechanism in carbon dots (graphene quantum dots, carbon nanodots, and polymer dots): current state and future perspective, Nano Res. 8 (2015) 355-381.

[34] J.R. Macairan, D.B. Jaunky, A. Piekny, R. Naccache, Intracellular ratiometric temperature sensing using fluorescent carbon dots, Nanoscale Adv. 1 (2019) 105-113.

[35] J.R. Macairan, I. Zhang, A. Clermont-Paquette, R. Naccache, D. Maysinger, Ratiometric pH Sensing in Living Cells Using Carbon Dots, Part. Part. Syst. Charact. *37* (2020) 1900430.

[36] Z.H. Wen, X.B. Yin, Excitation-independent carbon dots, from photoluminescence mechanism to single-color application, RSC Adv. 6 (2016) 27829-27835.

[37] J.A. Schmidt, S. Rinaldi, A. Scalbert, P. Ferrari, D. Achaintre, M.J. Gunter,...R.C. Travis, Plasma concentrations and intakes of amino acids in male meat-eaters, fish-eaters, vegetarians and vegans: a cross-sectional analysis in the EPIC-Oxford cohort, Eur. J. Clin. Nutr. 70 (2016) 306-312.

[38] K.P. Kuijpers, C. Bottecchia, D. Cambié, K. Drummen, N.J. König, T. Noël, A Fully Automated Continuous-Flow Platform for Fluorescence Quenching Studies and Stern–Volmer Analysis, Angew. Chem. Int. Ed. 57 (2018) 11278-11282.

[39] S. Roy, T.K. Das, Study of interaction between tryptophan, tyrosine, and phenylalanine separately with silver nanoparticles by fluorescence quenching method, J. Appl. Spectrosc. 82 (2015) 598-606.

[40] S. Roy, An insight of binding interaction between Tryptophan, Tyrosine and Phenylalanine separately with green gold nanoparticles by fluorescence quenching method, Optik. 138 (2017) 280-288.

[41] R. Dwivedi, D.P. Singh, B.S. Chauhan, S. Srikrishna, A.K. Panday, L.H. Choudhury, V.P. Singh, Intracellular application and logic gate behavior of a 'turn off-on-off'type probe for selective detection of Al3+ and F− ions in pure aqueous medium. Sens. Actuators B-Chem. 258 (2018) 881-894.

[42] U.P. Raghavendra, M. Basanagouda, A.H. Sidrai, J. Thipperudrappa, Spectroscopic investigations on the interaction of biologically active 4-aryloxymethyl coumarins with TiO2 nanoparticles, J. Mol. Liq. 222 (2016) 601-608.

[43] A. Van Der Vliet, J.P. Eiserich, H. Kaur, C.E. Cross, B. Halliwell, [16] Nitrotyrosine as biomarker for reactive nitrogen species, Meth. Enzymol. 269 (1996) 175-184.

[44] R. Radi, G. Peluffo, M.N. Alvarez, M. Naviliat, A. Cayota, Unraveling peroxynitrite formation in biological systems, Free Radic. Biol. Med. 30 (2001) 463-488.

[45] J. Jiang, D. Abramavicius, B.M. Bulheller, J.D. Hirst, S. Mukamel, Ultraviolet spectroscopy of protein backbone transitions in aqueous solution: Combined QM and MM simulations, J. Phys. Chem. B. 114 (2010) 8270-8277.

[46] F. Yarur, J.R. Macairan, R. Naccache, Ratiometric detection of heavy metal ions using fluorescent carbon dots, Environ. Sci. Nano. 6 (2019) 1121-1130.

[47] J.Z. Huo, X.S. Li, J.D. An, Y. Li, G.X. Du, X.X. Wu,... B. Ding, Photo-luminescent chiral carbon-dot@ Eu (D-cam) nanocomposites for selectively luminescence sensing of L-phenylalanine, J. Mol. Struct. 1201 (2020) 127214.

[48] Y. Wang, Q. Yue, Y. Hu, C. Liu, L. Tao, C. Zhang . Synthesis of N-doped carbon dots and application in vanillin detection based on collisional quenching. RSC Advances 9 (2019) 40222-4022.

[49] C. Batthyány, S. Bartesaghi, M. Mastrogiovanni, A. Lima, V. Demicheli, R. Radi, Tyrosine-nitrated proteins: proteomic and bioanalytical aspects, Antioxid. Redox Signal. 26 (2017) 313-328.

[50] Y. Liu, X. Tang, M. Deng, Y. Cao, Y., Li, Y., Zheng, H., ... & Qiu, F. . Nitrogen doped graphene quantum dots as a fluorescent probe for mercury (II) ions. *Microchimica Acta*, *186*(3) (2019), 1-8.

[51] F. Zu, F. Yan, Z. Bai, J. Xu, Y. Wang, Y. Huang, X. Zhou, The quenching of the fluorescence of carbon dots: a review on mechanisms and applications. Microchim. Acta. 184 (2017) 1899-1914.

[52] H. Soni, P.S. Pamidimukkala, Green synthesis of N, S co-doped carbon quantum dots from triflic acid treated palm shell waste and their application in nitrophenol sensing, Mater. Res. Bull. 108 (2018) 250-254.

[53] F. Zu, F. Yan, Z. Bai, J. Xu, Y. Wang, Y. Huang, X. Zhou, The quenching of the fluorescence of carbon dots: a review on mechanisms and applications, Microchim. Acta. 184 (2017) 1899-1914.

[54] O. Klep, Y. Bandera, S.H. Foulger, Temperature responsive nanoparticles: poloxamers as a modulator of Förster resonance energy transfer (FRET), Nanoscale. 10 (2018) 9401-9409.

[55] Y. Li, N. Cai, M. Wang, W. Na, F. Shi, X. Su, Fluorometric detection of tyrosine and cysteine using graphene quantum dots, RSC Adv. 6 (2016) 33197-33204.

[56] S. Das, L. Ngashangva, P. Goswami, Carbon dots: an emerging smart material for analytical applications. Micromachines 12 (2021) 84.

[57] L. Tang, C. Fang, C. Nitration of tyrosine channels photoenergy through a conical intersection in water. J. Phys. Chem. B. 123 (2019) 4915-4928.

[58] R. Jalili, M. Amjadi, Bio-inspired molecularly imprinted polymer–green emitting carbon dot composite for selective and sensitive detection of 3-nitrotyrosine as a biomarker, Sens. Actuators B-Chem, 255 (2018) 1072-1078.

[59] P.I. Djurovich, E.I. Mayo, S.R. Forrest, M.E. Thompson, Measurement of the lowest unoccupied molecular orbital energies of molecular organic semiconductors, Org. Electron. 10 (2009) 515–520.

[60] B. Ju, Y. Wang, Y.M. Zhang, T. Zhang, Z. Liu, M. Li, S. Xiao-An Zhang, Photostable and low-toxic yellow-green carbon dots for highly selective detection of explosive 2,4,6-TRINITROPHENOL based on the dual electron transfer mechanism, ACS Appl. Mater. Inter. 10 (2018) 13040–13047.

[61] N.O. Eddy, Experimental and theoretical studies on some amino acids and their potential activity as inhibitors for the corrosion of mild steel, part 2, J. Adv. Res. 2 (2011) 35-47.

[62] Y. Zhang, Z. Dong, J. Han, Z. Wei, Improved pharmacological properties of nitrotyrosine drug via fluorination: A theoretical study, Comput. Biol. Chem. 89 (2020) 107395.

[63] A. Erkoç, F. Erkoç, A. Sepici-Dinçel, Quantum chemical investigation of nitrotyrosine (3-nitro-l-tyrosine) and 8-nitroguanine, Amino Acids. 38 (2009) 319–327.

Chapter 3 - Copper (II) and Iron (III)-catalyzed nitration of tyrosine and role of CDs

3.1 Introduction

Post-translational modifications like nitration are frequently observed in diseased states. Nitration of tyrosine (Tyr) residues of protein is a covalent modification that introduces a nitro group ($-NO_2$) to the ortho carbon of the phenolic ring of Tyr and is a sign of nitrosative stress. As a result, an overall net negative charge is introduced to the nitrated Tyr at the physiological pH, causing changes to the protein in its chemical environment [1]. A change in tyrosine's pKa, from ~10 to ~7, impairs its ability to form hydrogen bonds when it is nitrated (Figure 3.1) [2]. The function of the protein is impacted because of the structural change, leading to the loss of protein activity. This becomes detrimental and is a sign of oxidative stress, which plays an important role in nitrotyrosine (nTyr) formation in neurodegenerative diseases such as Alzheimer's Disease (AD), Parkinson's disease (PD), amyotrophic lateral sclerosis (ALS), Huntington's disease (HD) and Prion disease [3].
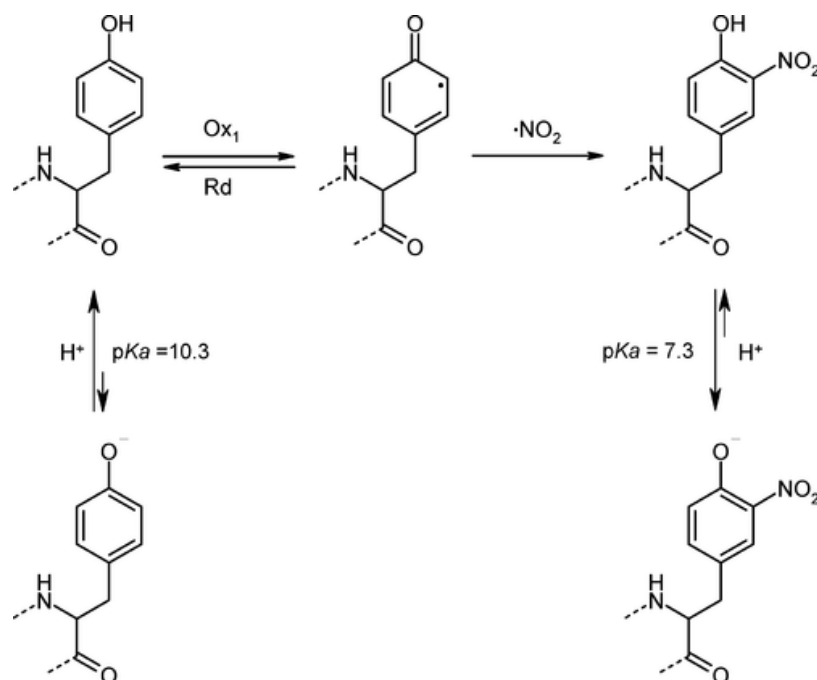
Figure 3.1. General mechanism of Tyr nitration and ionization [4].

Studies have reported a 2-10 fold and 1.5-2 fold increase of protein Tyr nitration and a free

Tyr nitration, respectively, depending on the disease and tissue [5]. The nitration of Tyr residues

generates a stable product. In biological systems, nitration of Tyr residues is a free radical process

and is selective [6]. Although tyrosine amino acids make up most of the proteins (3-4%), not all

sites are nitrated [6,7]. The best well-known mechanism for tyrosine nitration involves a one-step

oxidation of tyrosine to form tyrosyl radical, which then through a diffusion-controlled reaction

with nitrogen dioxide ($^\bullet$NO$_2$) produces nitrotyrosine [7,8]. It is mediated by reactive nitrogen

species such as peroxynitrite anion (ONOO–) and nitrogen dioxide ($^\bullet$NO$_2$). These are the

secondary products of $^\bullet$NO metabolism in the presence of oxidants such as superoxide radicals

($O_2{^{\bullet-}}$), hydrogen peroxide (H_2O_2), and transition metal centers [8].

Transition metals act as cofactors and are important parts of living organisms that allow

for biological processes to occur [9]. Specially, Cu(II) and Fe(III) ions, the most abundant metals,

in humans catalyze nitration reactions through peroxynitrite (ONOO$^-$) formation due to their

70

ability to carry out redox reactions [9]. Specifically, Cu(II) promotes the generation of free radicals that cause oxidative damage to cells [10]. Cu(II) plays a role in neurodegenerative diseases. Very high levels of Cu(II) (400% higher) have been observed in brains with AD compared to healthy brains, with a high concentration of 0.4 mM [11]. In addition, nitration of Tyr in biological settings is also driven by Fe(III) ions iron through its ability to reduce (active) molecular oxygen and to catalyze the conversion of superoxide and hydrogen peroxide to free radical species [12]. The average body of an adult human contains ~3-4 g of iron and 65% of it is bound to hemoglobin, an oxygen carrying protein [13]. Ten percent is a constituent of myoglobin, cytochromes, and iron-containing enzymes, and the rest is bound to the iron storage proteins [14]. The higher levels of iron in tissues such as the heart could serve as a biological base for iron toxicity on tissue damage as a result of free radicals, including the formation of nitrotyrosine [14]. Using transition metals in protein tyrosine nitration increases the yield of the reaction [9].

Hence, understanding how Cu(II) and Fe(III) metal ions catalyze nitration of free Tyr to form nTyr is of interest. Although there are many methods of detecting nTyr [5], these methods do not provide a real time monitoring of Tyr nitration, which will be beneficial in providing early detection of diseased states. In this chapter, the nitration reaction was monitored *in vitro* in order to synthesize nTyr in the presence of sodium nitrite and hydrogen peroxide, compare Cu(II) versus Fe(III) catalysis, and potentially use carbon dots (CDs) synthesized from formamide and glutathione to monitor and detect nTyr formation. The ultimate goal is to develop nanomaterials capable of detecting biological relevant modifications in real time, for development of biomedical assays.

3.2. Experimental Section

3.2.1. Materials and methods

3.2.1.1. Chemicals and reagents

3-Nitro-L-Tyrosine, 98% was purchased from Alfa Aesar and was dissolved in DI water to a final concentration of 6 mM. L-tyrosine was purchased from Sigma Aldrich and was dissolved in DI water to a final concentration of 2 mM. Carbon dots (CDs) were obtained from Naccache lab at Concordia University and were dissolved in DI water to final concentrations of 0.1 mg/mL and 5 mg/mL [15]. Copper (II) Perchlorate was purchased from Alfa Aesar (USA) and was dissolved in DI water to a final concentration of 5 mM. Copper (II) Nitrate 2.5 hydrate was purchased from J.T. Baker and was dissolved in DI water to a final concentration of 5 mM. Copper (II) Sulfate was purchased from Caledon and was dissolved in DI water to a final concentration of 5 mM. Iron (III) Perchlorate was purchased from Alfa Aesar and was dissolved in DI water to a final concentration of 10 mM. Sodium nitrite ($NaNO_2$) was kindly donated by Dr. Steven Rafferty's lab at Trent University and it was dissolved in DI water to a final concentration of 5 mM. Hydrogen peroxide (H_2O_2), 3%, was purchased from Delon Laboratories.

3.2.1.2. Methods

3.2.1.1. UV-vis absorbance spectroscopy

The UV-vis absorbance spectra (200 - 800 nm) were recorded using UV-2550 UV-vis spectrophotometer (Shimadzu and Cary 60) in a 1 cm quartz cuvette at a fast speed, 1 sampling interval and 2-nm bandwidth. The total volume of the sample was 3000 μL.

3.2.1.2. Fluorescence spectroscopy

The fluorescence spectra of the samples were recorded using the Varian Cary Eclipse Fluorescence Spectrophotometer. The fluorescence emission spectra (430 - 800 nm) were obtained

at an excitation wavelength of 420 nm using 1 cm quartz cuvette at a scan rate of 600 nm/min, 1 nm data interval and 5 nm excitation slit. The emission slit was adjusted to 10 nm. The total volume of the sample was 3000 µL.

3.2.2. Nitration reactions

3.2.2.1. Cu(II) catalyzed nitration reactions

The reaction mixture was composed of 0.25 mM Tyr, 0.25 mM Cu(II) Perchlorate 2.5 hydrate, 0.5 mM H_2O_2 and 1 mM $NaNO_2$ in DI water. The reaction was stirred for 0 - 72 h at room temperature, unless otherwise mentioned. UV-vis measurements were taken at 0h, 24h, and 72h. As a control, 0.25 mM Tyr in DI water was used. After the measurements were taken, 150 µL of 0.1 mg/mL CDs was added to the mixture (final concentration of 0.003 mg/mL) and UV-vis and fluorescence measurements were taken.

3.2.2.2. Fe(III) catalyzed nitration reactions

The reaction mixture was composed of 0.25 mM Tyr, 0.25 mM Fe(III) Perchlorate 2.5 hydrate, 0.5 mM H_2O_2 and 1 mM $NaNO_2$ in DI water. The reaction was stirred for 72 h at room temperature, unless otherwise mentioned. As a control, 0.25 mM Tyr in DI water was used. UV-vis measurements taken at 0 and 72h. After the measurements were taken, 150 µL of 0.1 mg/mL CDs was added to the mixture (final concentration of 0.003 mg/mL) and UV-vis and fluorescence measurements were taken.

3.2.2.3. Testing CDs as inhibitors of nitration reaction

In order to see if CDs inhibit Cu(II) or Fe(III) catalyzed nitration reaction, 1 µL of 5 mg/mL CDs was added to the reaction mixture (final concentration of 0.001 mg/mL) and UV-vis and fluorescence measurements were taken at 0 and 72h. As controls, 0.25 mM Tyr in DI water without

CDs, 0.25 mM Tyr in DI water with the addition of 1 µL of 5 mg/mL (final concentration of 0.001 mg/mL) CDs and nitration reaction without CDs were used.

3.3. Results and Discussion

In order to monitor nitration reaction and confirm nTyr formation, UV-vis absorbance was compared for Tyr and nTyr (Figure 3.1). While Tyr does not have an absorbance band in the visible range, nTyr has a characteristic band in the 300-470 nm range, which could be used for monitoring formation of nTyr from Tyr. In addition, Tyr is a colourless solution in DI water whereas nTyr is yellow. Firstly, UV-vis spectra of Tyr and nTyr in water were tested to evaluate their electronic transitions. For nTyr, there were three distinct peaks at 216 nm (2.871 a.u.), 280 nm (1.091 a.u.) and 355 nm (0.495 a.u.). For Tyr, there were two distinct peaks at 223 nm (1.674 a.u.) and 274 nm (0.297 a.u.). These photophysical trends were similar to the literature reports [16]. Unique peak of nTyr at 355 nm was used to monitor the course of the nitration reaction. The extinction coefficient (ε) of nTyr at 355 nm was calculated to be 1980 M^{-1} cm^{-1} using Beer-Lambert's Law ($A = \varepsilon bc$) with a path length of 1 cm. This was consistent with literature value reporting ~2200 M^{-1} cm^{-1} at ~ 380 nm for nitrotyrosine containing analogs [16]. The extinction coefficient of nTyr was used in conjunction with Beer-Lambert's Law to calculate the yields of nitration reactions.
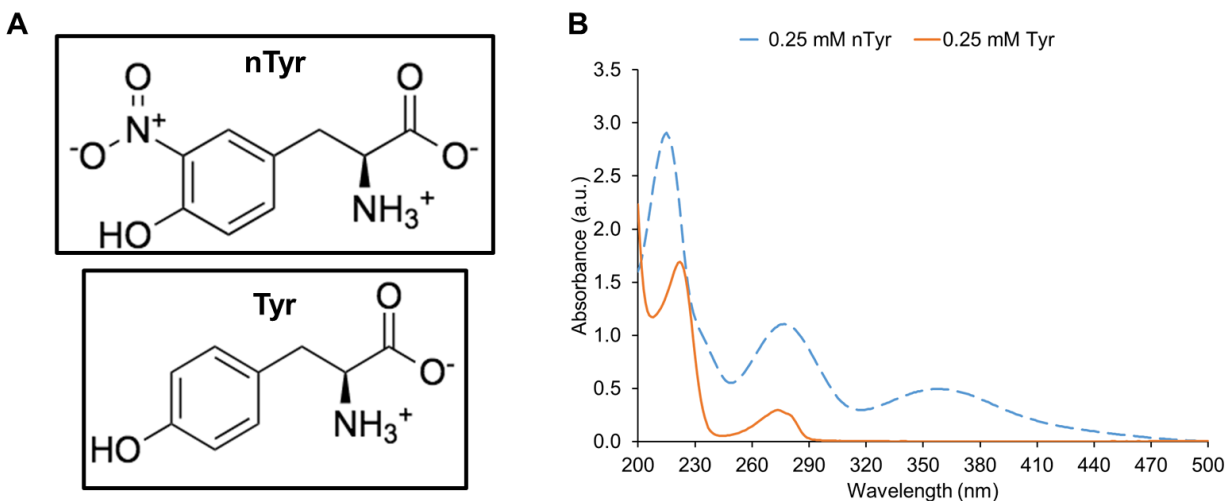
Figure 3.2. (A) Chemical structures of nTyr and Tyr and (B) UV-vis absorbance of 0.25 mM nTyr and 0.25 mM Tyr in water.

3.3.1. Cu(II)-catalyzed nitration reaction of Tyr into nTyr and role of CDs

Cu(II) is widely used in the catalysis of important cellular functions. It is used by many enzymes in oxidation reactions, such as superoxide by superoxide dismutase and catechols by tyrosinase [10]. An excess of Cu(II) in the body is detrimental as it is able to catalyze the generation of toxic reactive oxygen species. Due to the biological relevance of Cu(II) in a biological setting, the nitration of Tyr was performed using Cu(II) catalyst. The nitration reaction was carried out in the presence of various Cu(II) salts in order to investigate the role of counter anion on the reaction yield. The reaction was optimized using various Cu(II) concentrations, reaction time and temperature.

Cu(II) salts tested as catalysts include the following: Cu(II) Sulfate Pentahydrate, Cu(II) Nitrate 2.5 hydrate and Cu(II) Perchlorate (Table 3.1). The reaction yield increased with reaction time (0 - 72h). The concentration of nTyr produced at 72 h was between 0.067 - 0.075 mM (27-30% in yield), depending on the Cu(II) salt used. To improve the reaction yield, heat (45°C) or increase in Cu(II) was used (Table 3.2), however only 1.2x and 1.1x increase in yield was

observed, respectively. Hence, the optimal reaction conditions were identified to be using Copper (II) Perchlorate, room temperature and 72 h with a yield of ~30%.

Table 3.1. Yield (%) of nTyr produced as a function of three different Cu(II) salts (DI water, t = 24h, 48h, 72h; [Tyr] = 0.25 mM, [Cu(II)] = 0.25 mM; [H₂O₂] = 0.5 mM; [NaNO₂] = 1 mM; single measurements; % yield was calculated based on the absorbance at 355 nm, and ε value for nTyr standard).

	Time (h)	Cu(II) Sulfate Pentahydrate	Cu(II) Nitrate 2.5 hydrate	Cu(II) Perchlorate
	24	19	22	21
Yield (%)	48	23	24	26
	72	27	27	30

Table 3.2. Yield (%) of nTyr produced using various conditions and Cu(II) Sulfate Pentahydrate (DI water, t =24h, 48h; [Tyr] = 0.25 mM, [Cu(II)] = 0.25 mM; [H_2O_2] = 0.5 mM; [$NaNO_2$] = 1 mM; single measurements; %yield was calculated based on the absorbance at 355 nm, and ε value for nTyr standard).

	Time (h)	0.25 mM Cu(II) Sulfate Pentahydrate	0.25 mM Cu(II) Sulfate Pentahydrate + Heat (45 °C)	0.5 mM Cu(II) Sulfate Pentahydrate
Yield (%)	24	18	30	22
	48	23	29	26

The representative UV-vis spectra of Tyr and nTyr (synthesized using the optimal condition) are shown in Figure 3.3. After 72h, the absorbance increases for the nitration reaction of Tyr compared to the control of Tyr alone and there is a noticeable colour change. Specifically, at 355 nm, a peak is forming for the nitration reaction with an absorbance of 0.173 a.u. but is absent for the control. The peak at 355 nm shows that Tyr is converting into nTyr and it was calculated to have a %yield of 30% at 72h.
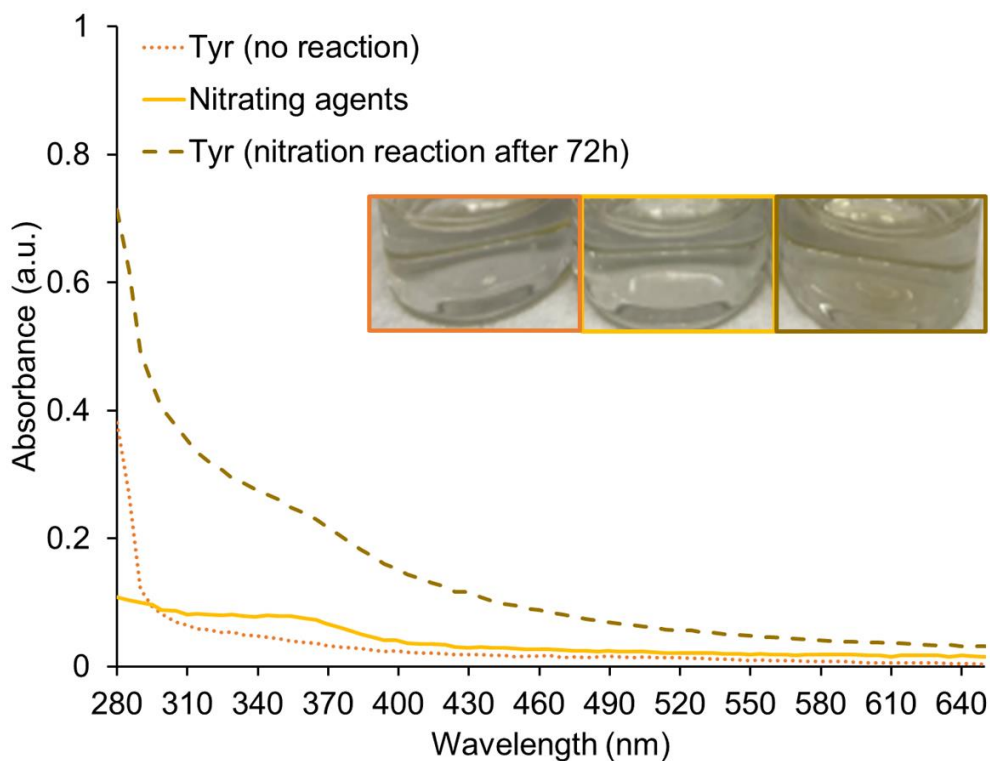
Figure 3.3. (A) UV-vis absorbance of 0.25 mM Tyr (Tyr control), nitrating agents (without Tyr), and nitration reaction (with Tyr) with Cu(II) used as a catalyst (DI water, t = 72h, [Tyr] = 0.25 mM; [Cu(II) perchlorate] = 0.25 mM; [H_2O_2] = 0.5 mM; [$NaNO_2$] = 1 mM).

Chapter 2 showed that if nTyr was present in solution, then the fluorescence of the CDs is quenched and the amount of quenching is used to estimate the concentration of nTyr in solution. In order to use CDs as indicators of nTyr present in solution following a nitration reaction, ideally, nitrating agents should not affect the fluorescence of CDs. The fluorescence of CDs was monitored in the presence of various reagents present in the nitration reaction (Figure 3.4A). In the absence of any reagents, emission bands at ~490 nm and ~680 nm with a shoulder at ~650 nm were observed. Cu(II) and hydrogen peroxide greatly quenched the fluorescence of the CDs whereas sodium nitrite increased the fluorescence of the CDs as seen by the increase in intensity at ~680

nm. CDs synthesized by the carbonization of poly-ethylenimine (PEI) with microwave irradiation found that Cu(II) quenched CDs through a non-radiative electron transfer process with a limit of detection of 6.7 nM in the linear range of 0.01–2 μM [17]. Various studies have observed that CDs synthesized from different materials are quenched in the presence of Cu(II) and thus, are used as sensors [18-21]. However, other studies show that Cu(II) does not quench CDs [22]. This shows that the chemical make-up of the CDs is important in how it interacts with Cu(II). Although the CDs used in this work were quenched in the presence of hydrogen peroxide, CDs synthesized using L-penicillamine via a single-step process have been used as sensors for hydrogen peroxide in combination with hemoglobin through a "on/off/on" sensing mechanism, in which CDs are quenched after the addition of hemoglobin (Hb) through $\pi-\pi$ interaction between the heme units of Hb and the aromatic ring system of CDs but is recovered by the addition of hydrogen peroxide due to the breakdown of Hb [23]. Another work shows that CDs synthesized by citric acid and ethylenediamine and then modified by 2-(diphenylphosphino)ethylamine quenched the fluorescence through a photo-induced electron transfer; however, in the presence of hydrogen peroxide, the fluorescence was recovered [24]. CDs have been used to detect nitrite through the inner filter effect between CDs (made from 3-aminophenol and ethanol) and *S*-nitrosothiol compound, which was the product of the nitrite–thiol chemical reaction [25]. CDs synthesized by the carbonization and polymerization of acriflavine quenched in the presence of nitrite through a combination of static and dynamic quenching in which the phenylamine groups on the surface interact with nitrite to form diazonium [26]. Although most studies have shown that CDs are quenched by the addition of nitrites, one particular study using PEG6000 coated carbon nanoparticles (PCNs) showed that in the presence of NO_2^- ions, fluorescence increased due to the hydrogen bonding of nitrite ions with the molecules causing them to aggregate and increasing the

surface area of light passivation [27]. Understanding how the nitrating agents interact with CDs was beneficial.

Since CDs were quenched with several reaction reagents, the possible interference of CDs as inhibitors was tested next (Figure 3.4C). At 355 nm, nitration of 0.25 mM Tyr resulted in similar absorbance in the presence and absence of CDs, leading to similar yields. The fluorescence of CDs present in the nitration reaction of Tyr were completely quenched (~90%) before and after the reaction at t = 72h. Although the nitration reaction of Tyr quenched the fluorescence of the CDs, they clearly did not act as inhibitors of the reaction, and hence, CDs were next used as indicators of Tyr nitration.
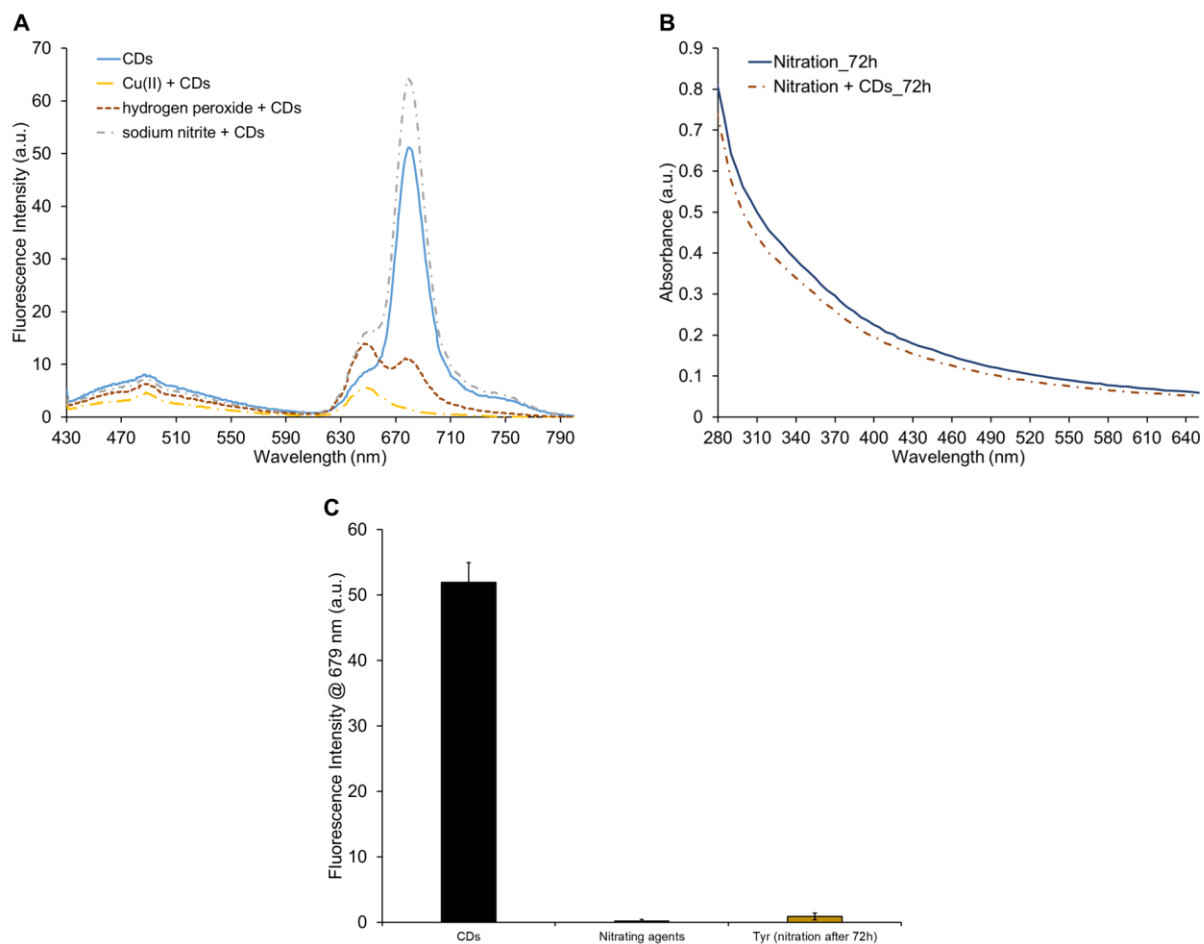
Figure 3.4. (A) Fluorescence emission spectrum of CDs with controls of nitration reaction at t = 0h; [CDs] = 0.003 mg/mL; λ_{ex} = 420 nm. (B) Plot of emission peak at 679 nm of Cu(II) catalyzed nitration reaction at 72 h after adding CDs as indicators; error bars indicate standard deviation; [CDs] = 0.003 mg/mL; λ_{ex} = 420 nm. (C) UV-vis absorbance of nitration reaction (with Tyr) with Cu(II) perchlorate used as a catalyst in the presence and absence of CDs as inhibitors (DI water, t = 0 h and 72 h; [Tyr] = 0.25 mM; [Cu(II) perchlorate] = 0.25 mM; [H_2O_2] = 0.5 mM; [$NaNO_2$] = 1 mM; [CDs] = 0.001 mg/mL; λ_{ex} = 420 nm; single measurement).

Lastly, CDs were used as indicators of Tyr nitration reaction and were added at 72h. To monitor nitration of Tyr into nTyr, the fluorescence emission of CDs at 679 nm was monitored (Figure 3.3B). The results show that CDs are significantly quenched (~95%) by both the nitrating agents and the nitration reaction and are unable to differentiate nTyr formation. This makes them unsuitable for use in detecting the Cu(II) catalyzed nitration of Tyr.

3.3.2. Fe(III)-catalyzed nitration reaction of Tyr into nTyr and role of CDs

Fe(III) is a useful component in hemoproteins and metalloproteins [13]. It can catalyze the conversion of superoxide and hydrogen peroxide to free radical species, making it harmful to cells. Due to the biological relevance of Fe(III), the nitration of Tyr was also performed using Fe(III) catalyst. The UV-vis spectrum of the nitration reaction catalyzed by Fe(III) at 72h shows a peak at 355 nm with 0.72 a.u. whereas there is no distinct peak for Tyr (no reaction) (Figure 3.5A). The nitrating agents also absorb at 355 nm (0.18 a.u.) and this was taken into account when calculating the yield for nTyr. The peak at 355 nm shows that Tyr is converting into nTyr and it was calculated to have a %yield of ~80% at 72h.

To understand the role of CDs on Fe(III) catalyzed nitration of Tyr, the fluorescence of CDs was monitored in the presence of various reagents present in the nitration reaction (Figure 3.5B). In the absence of any reagents, emission bands at ~490 nm and ~680 nm with a shoulder at ~650 nm were observed. Fe(III) and hydrogen peroxide greatly quenched the fluorescence of the CDs at emission peaks of 650 nm and 680 nm whereas sodium nitrite increased its fluorescence. The same CDs used in the system were studied with metal ions and it was found that Fe(III) in the nM range quenched the fluorescence through static quenching as confirmed by lifetime measurements [28]. This is similar to another study where CDs made from papaya were quenched by Fe(III) [29]. However, one particular study shows that Fe(III) does not quench CDs synthesized

by nitrogen-doped CDs and rhodamine B isothiocyanate (RhB) [30]. As previously mentioned, hydrogen peroxide greatly quenched the fluorescence of CDs whereas sodium nitrite increased its fluorescence.

Since CDs were quenched with several reaction reagents, the possible interference with nitration reaction by CDs was tested next (Figure 3.5C). At 355 nm, nitration of 0.25 mM Tyr in the presence of CDs resulted in a slightly lower absorbance than in the absence of CDs (85%), producing a slightly lower yield (75%). The fluorescence of CDs was monitored when CDs were co-present in the nitration reaction. Figure 3.5D shows significant quenching (~95%) after the reaction at t = 72h, compared to CDs in the absence of reaction. The CDs did not significantly inhibit Tyr nitration, and hence, they were next used as indicators of Tyr nitration.
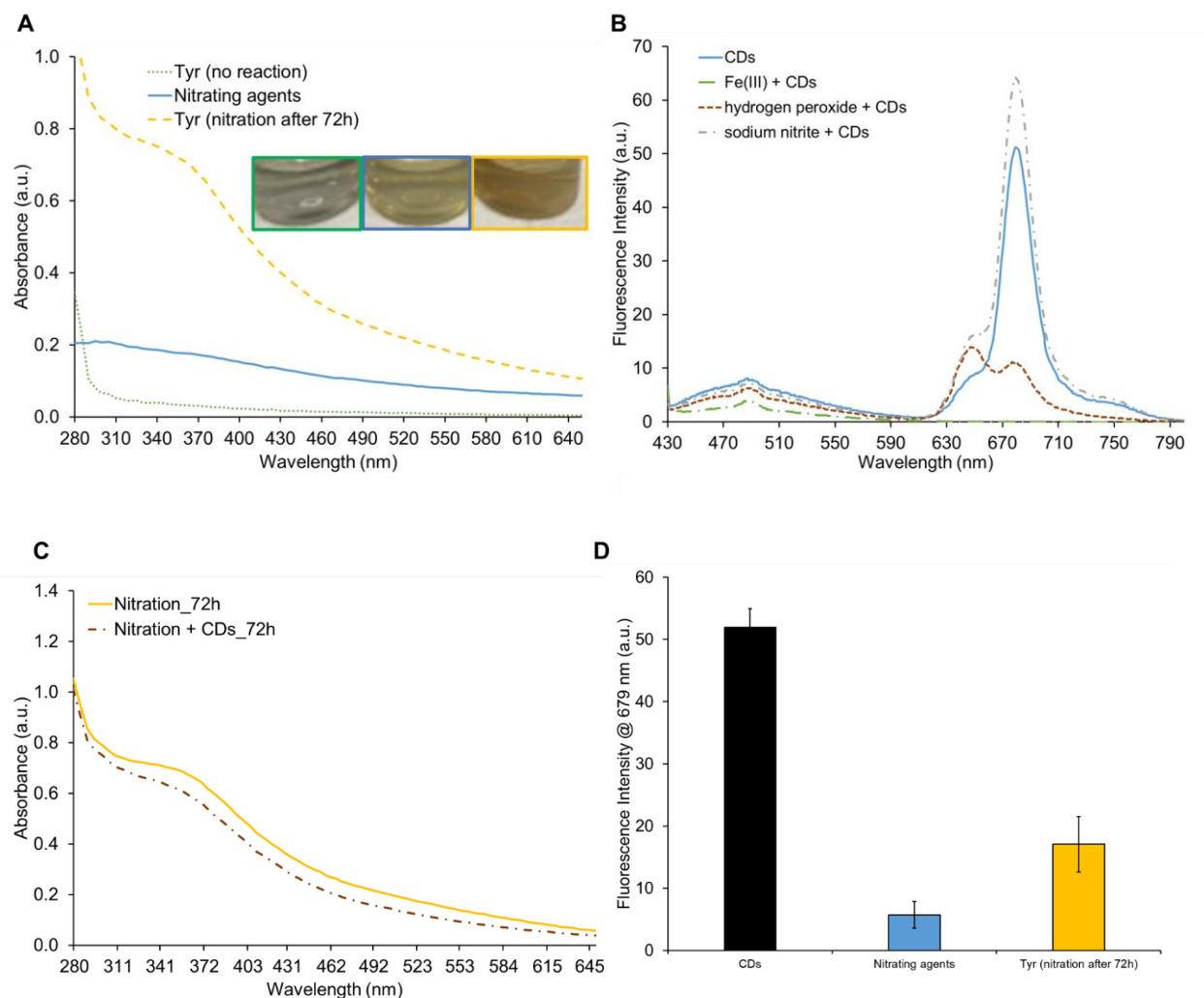
Figure 3.5. (A) UV-vis absorbance of 0.25 mM Tyr (Tyr control), nitrating agents (without Tyr), and nitration reaction (with Tyr) with Fe(III) used as a catalyst. (B) Fluorescence emission spectrum of CDs with controls of nitration reaction; [CDs] = 0.003 mg/mL; λ_{ex} = 420 nm. (C) Plot of emission peak at 679 nm of Fe(III) catalyzed nitration reaction at 72 h after adding CDs as indicators; error bars indicate standard deviation; [CDs] = 0.003 mg/mL; λ_{ex} = 420 nm. (D) UV-vis absorbance of nitration reaction (with Tyr) with Cu(II) perchlorate used as a catalyst in the presence and absence of CDs as inhibitors (DI water, t = 0 h and 72 h; [Tyr] = 0.25 mM; [Fe(III) perchlorate] = 0.25 mM; [H_2O_2] = 0.5 mM; [$NaNO_2$] = 1 mM; [CDs] = 0.001 mg/mL; single measurement).

84

To detect the presence of nTyr, the CDs were added as indicators after the reaction (t=72h) and their fluorescence emission monitored at 679 nm (Figure 3.5D). The results show that the samples significantly quench the fluorescence of the CDs (greater than 70%). Based on the calibration curve from Chapter 2, if nTyr was present at 0.36 mM it would lead to 70% quenching. However, the 100% theoretical yield of nTyr was calculated to be 0.000284 g or 0.25 mM (based on the starting material Tyr = 0.25 mM). Hence, if all Tyr was converted to nTyr, only 48% of quenching would be expected. However, the 70% of quenching observed cannot be described solely to nTyr formation, but rather to the quenching by nitration agents as well. Thus, CDs were not suitable as indicators of nTyr formation.

In this chapter, both Cu(II) and Fe(III)-catalyzed nitration reactions were carried out to mimic the biological relevance, specifically the ability of these transition metals to produce reactive species, which are detrimental and are implicated in neurodegenerative diseases. Based on the literature, the proposed mechanism for Cu(II) catalyzed nitration of Tyr involves a Fenton-like reaction in which hydroxyl radicals ($\bullet$OH) and/or Cu(II) bound $^{\bullet}$OH (Cu(II)–$^{\bullet}$OH) are generated downstream from LCu(II) (Figure 3.6) [31]. After the radicals are generated, they are scavenged by NO_2^- and tyrosine to form $^{\bullet}NO_2$ and tyrosine radicals (Tyr$^{\bullet}$), leading to tyrosine nitration [31]. It is also likely that LCu(II) is reduced to LCu(I) which subsequently reacts with $^{\bullet}NO_2$ to form Cu(II)(ONOO$^-$) species which can in turn nitrate Tyr. Similarly, the proposed mechanism of Fe(III) catalyzed nitration of Tyr involves the oxidation of Fe(III) by HO_2- to Fe(II) and superoxide anion radical (reaction 3). Next, the Fe(II) catalyzes formation of $^{\bullet}NO_2$ from nitrite (reaction 5) which subsequently reacts with tyrosine radical to form nTyr (reaction 12).
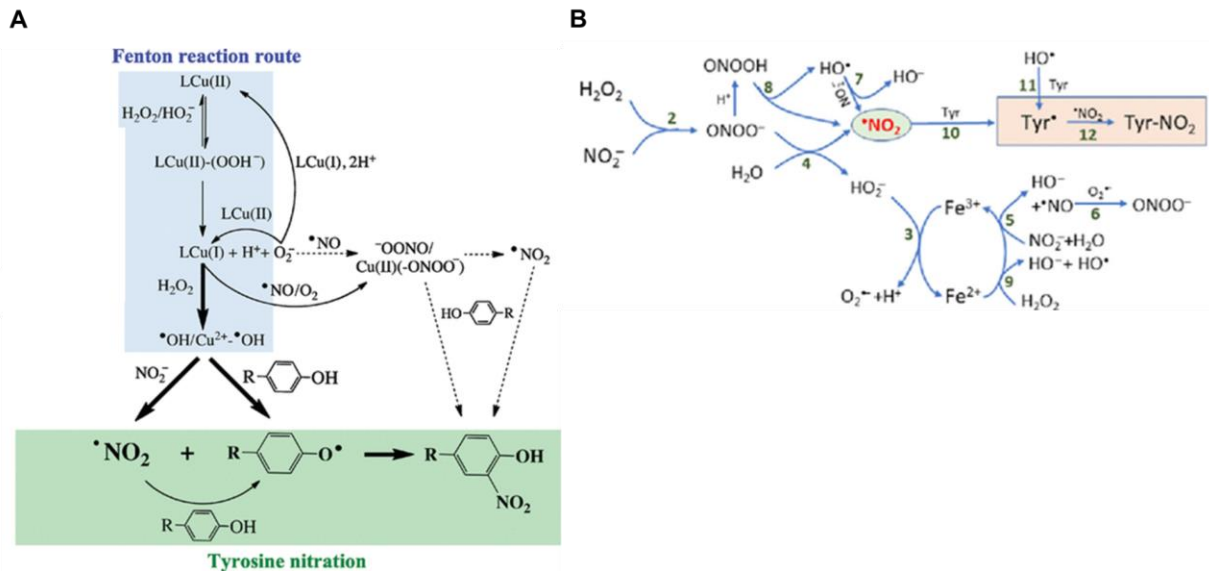
Figure 3.6. Proposed mechanism for (A) Cu(II) [31] and (B) Fe(III) [12] catalyzed nitration of Tyr.

Although both catalysts are relevant in a biological setting, Fe(III) perchlorate catalyzed nitration of Tyr produced the greatest yield of 81% ± 3% compared to Cu(II) perchlorate catalyzed reaction producing only a yield of 20% ± 8% (Figure 3.7). Cu(II) catalyzed nitration reaction of free amino acid, Tyr, produced a greater yield compared to Cu(II)-catalyzed nitration of the peptide, Angiotensin I, which only resulted in 10% nitration level when optimized conditions were used (CuCl$_2$ = 0.25 mM, H$_2$O$_2$ = 0.5 mM, NO$_2^-$ = 1 mM) [31]. Similarly, the role of iron in nitrating Tyr residues of BSA was studied and nitration was confirmed through Western blotting with antibodies specific to 3-nitrotyrosine [14]. It was found that nitration of BSA at Tyr residues were carried out in the presence of hydrogen peroxide and sodium nitrite [14]. In conclusion, although both catalysts play an important role in biological settings, the current work shows that Fe(III) catalyzed nitration was more efficient than Cu(II) catalyzed nitration reaction of Tyr.
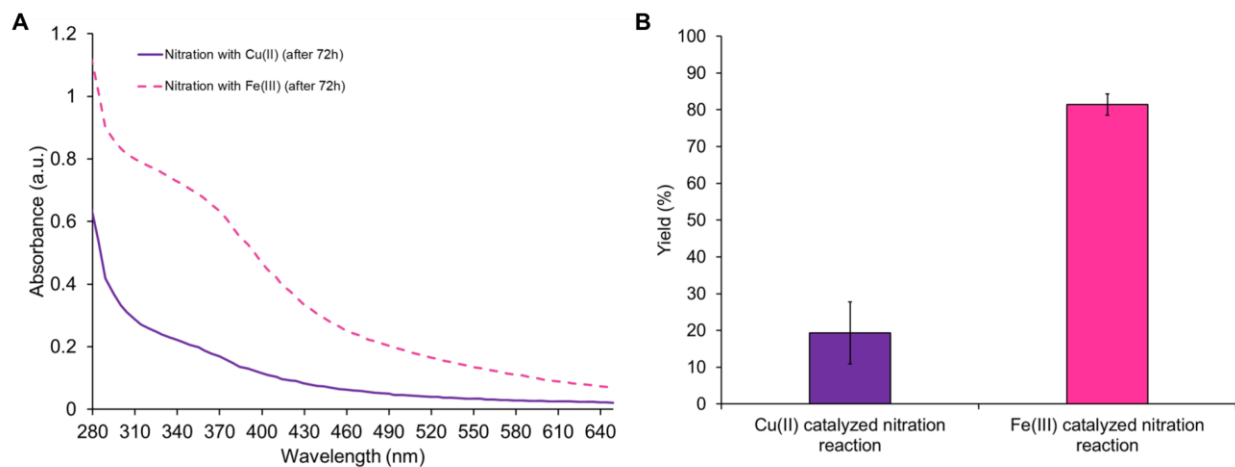
Figure 3.7. (A) UV-vis absorbance of nitration reaction with Fe(III) or Cu(II) used as a catalyst. (B) Plot of yield of Fe(III) and Cu(II) catalyzed nitration reaction; error bars indicate standard deviation from triplicate measurements (DI water, t = 72h, [Tyr] = 0.25 mM; [Fe(III) perchlorate] = 0.25 mM; [Cu(II) perchlorate] = 0.25 mM; $[H_2O_2]$ = 0.5 mM; $[NaNO_2]$ = 1 mM).

In addition, the role of CDs on nitration reactions were studied in order to potentially use CDs to detect nTyr formation. Importantly, CDs did not interfere with the nitration reaction of Tyr when using Cu(II) or Fe(III) as catalysts. Although CDs did not interfere with the nitration reaction, it is of interest to see whether they could act as catalysts of nitration. CDs made from other precursors have shown to catalyze various reactions [32] like methanol oxidation [33], oxygen reduction [34], dopamine reduction [35] and the transesterification of canola oil [36-37]. About 1 weight percent (wt%) of CDs loading (synthesized from glycine and citric acid) was needed to achieve ≥ 97% at 150 °C for the transesterification of canola oil to biodiesel [36]. This unique ability for CDs to act as catalysts is due to their high surface area-to-volume ratio and the ability to add different functional groups on their surface [38]. It is unknown whether the CDs used in this system, which were made from glutathione and formamide, catalyze any reactions. In this

inhibitor system, a very low concentration of CDs (0.001 and 0.003 mg/mL) were used and hence, it is very likely that CDs did not catalyze the nitration of Tyr. Additional experiments should be conducted to investigate whether CDs can catalyze nitration reactions in the absence of metal ions. The CDs were also not ideal as sensing probes for the detection of nTyr, due to their fluorescence quenching by nitration agents.

3.4. Conclusions

In summary, the nitration of free amino acid Tyr was carried out successfully using Cu(II) or Fe(III) as catalysts in the presence of hydrogen peroxide and sodium nitrite to mimic the biological setting. Furthermore, the role of CDs in the nitration of Tyr was tested using optimal conditions. Data indicate that CDs did not interfere with either Cu(II) or Fe(III) catalyzed nitration reactions, producing similar yields of nTyr in the presence and absence of CDs. Nitration reagents quenched the fluorescence of CDs, indicating that CDs cannot be used as indicators of Tyr nitration.

3.5 References

[1] Yeo, W. S., Lee, S. J., Lee, J. R., & Kim, K. P. (2008). Nitrosative protein tyrosine modifications: biochemistry and functional significance. *BMB reports*, *41*(3), 194-203.

[2] Zhan, X., Wang, X., & Desiderio, D. M. (2015). Mass spectrometry analysis of nitrotyrosine-containing proteins. *Mass spectrometry reviews*, *34*(4), 423-448.

[3] Bandookwala, M., & Sengupta, P. (2020). 3-Nitrotyrosine: a versatile oxidative stress biomarker for major neurodegenerative diseases. *International Journal of Neuroscience*, *130*(10), 1047-1062.

[4] Radi, R. (2013). Protein tyrosine nitration: biochemical mechanisms and structural basis of functional effects. *Accounts of chemical research*, *46*(2), 550-559.

[5] Greenacre, S. A., & Ischiropoulos, H. (2001). Tyrosine nitration: localisation, quantification, consequences for protein function and signal transduction. *Free radical research*, *34*(6), 541-581.

[6] Batthyány, C., Bartesaghi, S., Mastrogiovanni, M., Lima, A., Demicheli, V., & Radi, R. (2017). Tyrosine-nitrated proteins: proteomic and bioanalytical aspects. *Antioxidants & redox signaling*, *26*(7), 313-328.

[7] Bartesaghi, S., Ferrer-Sueta, G., Peluffo, G., Valez, V., Zhang, H., Kalyanaraman, B., & Radi, R. (2007). Protein tyrosine nitration in hydrophilic and hydrophobic environments. *Amino acids*, *32*(4), 501-515.

[8] Radi, R. (2004). Nitric oxide, oxidants, and protein tyrosine nitration. *Proceedings of the National Academy of Sciences*, *101*(12), 4003-4008.

[9] Campolo, N., Bartesaghi, S., & Radi, R. (2014). Metal-catalyzed protein tyrosine nitration in biological systems. *Redox Report*, *19*(6), 221-231.

[10] Reddy, P. V., Rama Rao, K. V., & Norenberg, M. D. (2008). The mitochondrial permeability transition, and oxidative and nitrosative stress in the mechanism of copper toxicity in cultured neurons and astrocytes. *Laboratory investigation*, *88*(8), 816-830.

[11] Geng, J., Li, M., Wu, L., Ren, J., & Qu, X. (2012). Liberation of copper from amyloid plaques: making a risk factor useful for Alzheimer's disease treatment. *Journal of medicinal chemistry*, *55*(21), 9146-9155.

[12] Peng, R., Wang, L., Yu, P., Carrier, A. J., Oakes, K. D., & Zhang, X. (2021). Exacerbated Protein Oxidation and Tyrosine Nitration through Nitrite-Enhanced Fenton Chemistry. *Journal of Agricultural and Food Chemistry*, *70*(1), 353-359.

[13] Fraga, C. G., & Oteiza, P. I. (2002). Iron toxicity and antioxidant nutrients. *Toxicology*, *180*(1), 23-32.

[14] Bian, K., Gao, Z., Weisbrodt, N., & Murad, F. (2003). The nature of heme/iron-induced protein tyrosine nitration. *Proceedings of the National Academy of Sciences*, *100*(10), 5712-5717.

[15] Yarur, F., Macairan, J. R., & Naccache, R. (2019). Ratiometric detection of heavy metal ions using fluorescent carbon dots. *Environmental Science: Nano*, *6*(4), 1121-1130.

[16] De Filippis, V., Frasson, R., & Fontana, A. (2006). 3-Nitrotyrosine as a spectroscopic probe for investigating protein–protein interactions. *Protein science*, *15*(5), 976-986.

[17] Wang, J., Li, R. S., Zhang, H. Z., Wang, N., Zhang, Z., & Huang, C. Z. (2017). Highly fluorescent carbon dots as selective and visual probes for sensing copper ions in living cells via an electron transfer process. *Biosensors and Bioelectronics*, *97*, 157-163.

[18] Chen, J., Li, Y., Lv, K., Zhong, W., Wang, H., Wu, Z., ... & Jiang, J. (2016). Cyclam-functionalized carbon dots sensor for sensitive and selective detection of copper (II) ion and sulfide anion in aqueous media and its imaging in live cells. *Sensors and Actuators B: Chemical*, *224*, 298-306.

[19] Ye, Z., Tang, R., Wu, H., Wang, B., Tan, M., & Yuan, J. (2014). Preparation of europium complex-conjugated carbon dots for ratiometric fluorescence detection of copper (II) ions. *New Journal of Chemistry*, *38*(12), 5721-5726.

[20] Rao, H., Liu, W., Lu, Z., Wang, Y., Ge, H., Zou, P., ... & Wang, Y. (2016). Silica-coated carbon dots conjugated to CdTe quantum dots: a ratiometric fluorescent probe for copper (II). *Microchimica Acta*, *183*(2), 581-588.

[21] Gedda, G., Lee, C. Y., Lin, Y. C., & Wu, H. F. (2016). Green synthesis of carbon dots from prawn shells for highly selective and sensitive detection of copper ions. *Sensors and Actuators B: Chemical*, *224*, 396-403.

[22] Teng, X., Ma, C., Ge, C., Yan, M., Yang, J., Zhang, Y., ... & Bi, H. (2014). Green synthesis of nitrogen-doped carbon dots from konjac flour with "off–on" fluorescence by Fe 3+ and L-lysine for bioimaging. *Journal of Materials Chemistry B*, *2*(29), 4631-4639.

[23] Bhunia, S. K., Dolai, S., Sun, H., & Jelinek, R. (2018). "On/off/on" hydrogen-peroxide sensor with hemoglobin-functionalized carbon dots. *Sensors and Actuators B: Chemical*, *270*, 223-230.

[24] Lan, M., Di, Y., Zhu, X., Ng, T. W., Xia, J., Liu, W., ... & Zhang, W. (2015). A carbon dot-based fluorescence turn-on sensor for hydrogen peroxide with a photo-induced electron transfer mechanism. *Chemical Communications*, *51*(85), 15574-15577.

[25] Yue, X., Zhou, Z., Wu, Y., Jie, M., Li, Y., Guo, H., & Bai, Y. (2020). A green carbon dots-based fluorescent sensor for selective and visual detection of nitrite triggered by the nitrite–thiol reaction. *New Journal of Chemistry*, *44*(20), 8503-8511.

[26] Rong, M., Wang, D., Li, Y., Zhang, Y., Huang, H., Liu, R., & Deng, X. (2021). Green-emitting carbon dots as fluorescent probe for nitrite detection. *Journal of Analysis and Testing*, *5*(1), 51-59.

[27] Menon, S., Vikraman, A. E., Jesny, S., & Girish Kumar, K. (2016). "Turn on" fluorescence determination of nitrite using green synthesized carbon nanoparticles. *Journal of fluorescence*, *26*(1), 129-134.

[28] Yarur, F., Macairan, J. R., & Naccache, R. (2019). Ratiometric detection of heavy metal ions using fluorescent carbon dots. *Environmental Science: Nano*, *6*(4), 1121-1130.

[29] Yang, R., Guo, X., Jia, L., Zhang, Y., Zhao, Z., & Lonshakov, F. (2017). Green preparation of carbon dots with mangosteen pulp for the selective detection of Fe3+ ions and cell imaging. *Applied Surface Science*, *423*, 426-432.

[30] Liu, L., Chen, L., Liang, J., Liu, L., & Han, H. (2016). A novel ratiometric probe based on nitrogen-doped carbon dots and rhodamine B isothiocyanate for detection of Fe3+ in aqueous solution. *Journal of Analytical Methods in Chemistry*, *2016*.

[31] Qiao, L., Lu, Y., Liu, B., & Girault, H. H. (2011). Copper-catalyzed tyrosine nitration. *Journal of the American Chemical Society*, *133*(49), 19823-19831.

[32] Manjupriya, R., & Roopan, S. M. (2021). Carbon dots-based catalyst for various organic transformations. *Journal of Materials Science*, *56*(31), 17369-17410.

[33] Yang, S., Zhang, F., Gao, C., Xia, J., Lu, L., & Wang, Z. (2017). A sandwich-like PtCo-graphene/carbon dots/graphene catalyst for efficient methanol oxidation. *Journal of Electroanalytical Chemistry*, *802*, 27-32.

[34] Zhang, P., Wei, J. S., Chen, X. B., & Xiong, H. M. (2019). Heteroatom-doped carbon dots based catalysts for oxygen reduction reactions. *Journal of colloid and interface science*, *537*, 716-724.

[35] Vazquez-Gonzalez, M., Liao, W. C., Cazelles, R., Wang, S., Yu, X., Gutkin, V., & Willner, I. (2017). Mimicking horseradish peroxidase functions using Cu2+-modified carbon nitride nanoparticles or Cu2+-modified carbon dots as heterogeneous catalysts. *ACS nano*, *11*(3), 3247-3253.

[36] Macina, A., de Medeiros, T. V., & Naccache, R. (2019). A carbon dot-catalyzed transesterification reaction for the production of biodiesel. *Journal of Materials Chemistry A*, *7*(41), 23794-23802.

[37] de Medeiros, T. V., Macina, A., & Naccache, R. (2020). Graphitic carbon nitrides: Efficient heterogeneous catalysts for biodiesel production. *Nano Energy*, *78*, 105306.

[38] Chahal, S., Macairan, J. R., Yousefi, N., Tufenkji, N., & Naccache, R. (2021). Green synthesis of carbon dots and their applications. *RSC advances*, *11*(41), 25354-25363.

Chapter 4 - Conclusion and Future Work

4.1 Conclusions

This thesis outlined the importance of studying amino acids, specifically tyrosine (Tyr) and its analogues, phosphotyrosine (pTyr) and nitrotyrosine (nTyr) and the use of nanomaterials, specifically carbon dots (CDs), to detect them in Chapter 1. For example, many biologically relevant transformations include chemical modifications of amino acids. Of interest to this work was nitration of Tyr to yield nTyr. Measuring the nitration reaction and formation of nTyr is of interest. Although there are many methods to detect Tyr and its analogues, these methods are often time-consuming, involve expensive instruments and involve tedious procedures. The use of nanomaterials in sensing applications has greatly influenced the sensitivity of detecting nTyr. Hence, the fluorescent nanomaterials were used in the design and development of a sensor for nTyr.

Chapter 2 outlined the role of CDs on Tyr and its analogues. Firstly, the CDs, which were synthesized by a microwave-mediated one-step reaction with glutathione and formamide, were characterized by ultraviolet visible (UV-vis) spectroscopy, fluorescence spectroscopy, transmission electron microscopy (TEM), Fourier-transform infrared spectroscopy (FT-IR) and powder X-ray diffraction (XRD). Compared to other nanomaterials, water-soluble CDs exhibited dual fluorescence which made them attractive for sensor applications. Then, the CDs were tested with Tyr and its analogues and it was found that they showed selectivity towards nTyr only and not Tyr and pTyr. The selection of fluorescent CDs towards nTyr was carried out using a turn-off mechanism in which the fluorescence of the CDs were quenched in the presence of nTyr in a concentration dependent manner. The mechanism of quenching was related to both the fluorescence resonance energy transfer (FRET) between the CDs (energy donor) and nTyr (energy

acceptor) and also photoinduced electron transfer from the excited state of CDs to nTyr. The LOD was 34 µM and LOQ was 137 µM in the linear range of 0.005 to 0.105 mM. Moreover, interference studies indicate that the CDs are ideally suited for detection of nTyr even in the presence of other biologically relevant molecules and in biological fluids like artificial saliva. The fluorescence CD-based assay may be used in a more complex mixture to mimic the biological fluids and makes it suitable for use in sensing applications to detect diseases related to nTyr.

To investigate the quenching mechanism of the fluorescence-CD-based assay, pH studies were conducted and life-time measurements and zeta potentials were obtained (Naccache Lab). As pH is changed, the overall charge of the amino acid changes. Although this was the case, the trends associated with the CD's ability to detect nTyr were not dependent on the overall charge change as an acidic, basic or neutral pH did not change the ability of the CD's to detect Tyr and pTyr. However, greater sensitivity to detect nTyr was observed at a basic pH of 10 compared to pH 6.8 and at pH 3, CDs were not able to detect nTyr. This greater sensitivity observed at a basic pH is due to a greater overlap of the absorbance of nTyr at a basic pH compared to pH 6.8 and not due to the changes in overall net charge at different pHs. Thus, electrostatic interactions do not contribute to the quenching of CDs by nTyr but are due to the overlap of the absorbance of nTyr and the emission at 460 nm. This is known as fluorescence resonance energy transfer (FRET) between the CDs (energy donor) and nTyr (energy acceptor). The mechanism of quenching is attributed to both static and dynamic quenching and was analyzed using Stern-Volmer plots and Benesi-Hilderbrand plots. In addition to FRET, photoinduced electron transfer from the excited state of CDs to nTyr was observed at 679 nm. Hence, this work provided a better understanding of the mechanism of quenching that is used in this fluorescence- CD-based assay.

In addition to using CDs to detect nTyr (as in Chapter 2), CDs were also used as indicators of an important biological transformation, nitration of Tyr, to generate nTyr *in vitro*, as described in Chapter 3. For this purpose, CDs were used either as 1) end-point indicators (at the end of the nitration reaction) or 2) real-time indicators (during nitration reaction). Two different metal catalysts were used for Tyr nitration: Cu(II) and Fe(III) metal ions, due to their biological relevance. It was found that Fe(III) catalyzed nitration reaction in the presence of hydrogen peroxide and sodium nitrite at room temperature produced a higher yield of ~80% compared to Cu(II), which only produced a yield of only ~20%. When using CDs as end-point indicators of nTyr formation, CDs fluorescence was dramatically quenched. However, the quenching was due to nitrating agents, Cu(II), Fe(II), hydrogen peroxide and sodium nitrite. Hence, CDs were not suitable end-point indicators of nitration reaction. When used as real-time indicators of nitration, it was found that CDs did not inhibit the nitration reaction. However, the quenching of CD fluorescence was due to nitrating agents as well. The quenching due to reagents present made it challenging to distinguish the quenching that is solely attributed to the presence of nTyr.

In conclusion, this thesis provided a deeper understanding on how fluorescent CDs, made from glutathione and formamide, interact with amino acids and nitrating agents, and could subsequently be used as biosensors to detect amino acids related to diseases.

4.2 Future Work

This thesis provided the framework of using CDs to detect amino acids related to diseases and provided insight into the use of CDs to monitor biologically relevant transformations like nitration. The CDs that were used in this work were selective to nTyr. Understanding the quenching of CDs by nTyr helps to design CDs that are sensitive to other amino acids used in this study. Both Tyr and pTyr do not absorb in the 420 nm range but do absorb around 200-300 nm. In order for CDs

to be sensitive to Tyr and pTyr, CDs that are emissive in this range should be used. For example, CDs, synthesized by a one-step hydrothermal method from cellobiose and doped with nitrogen, excite at 230 nm and 320 nm and were used to detect temperature and phosalone, an insecticide [1]. These CDs could be tested to see if they are selective to Tyr and pTyr. Additionally, the surfaces of CDs can be modified by including aptamers selective for Tyr or pTyr. Aptamers can be conjugated to CDs in order to provide greater sensitivity. For example, fluorescent and carboxyl-modified CDs, synthesized by the hydrothermal method, were connected by amino-modified aptamers on the surfaces to form the carbon dot–aptamer complexes that were used to detect *Salmonella typhimurium* [2]. Similarly, CDs made from citric acid monohydrate and diethylene triamine through the hydrothermal method were modified with dopamine aptamer and were then used to detect dopamine through a static quenching mechanism [3]. Moreover, a fluorometric aptamer-based assay using CDs (made from citric acid monohydrate and diethylene triamine through the hydrothermal method) and graphene oxide were used to detect adenosine triphosphate (ATP) through FRET quenching mechanism [4]. Other than using aptamers to detect Tyr and pTyr, the use of intermolecular interactions between CDs and AAs can be investigated. Since pTyr has a negatively charged phosphate group, CDs containing positive groups could be synthesized and be used for pTyr detection through their electrostatic interaction. For example, carbon quantum dots (C-dots), synthesized by a one-step hydrothermal method from o-aminophenol, was used to detect heparin. The detection was due to the electrostatic interactions and hydrogen bonding between the positively charged surface amino groups with the sulfate and carboxyl groups in heparin. These positively charged CDs can be used to detect pTyr.

Although the CDs used in this work were not able to monitor nitration of Tyr, further improvements can be made to produce desirable outcomes. CDs have the potential to be used as

indicators of reaction. One specific study used red CDs, synthesized through a hydrothermal treatment of *o*-phenylenediamine and urea as indicators of titration [5]. These CDs are unique as they have an acidichromism feature, which allows them to change colours depending on the pH and are used as indicators of titration in alkali samples [5]. Firstly, CDs can be easily modified either through a covalent or non-covalent modification [6]. When synthesizing CDs to indicate nTyr formation, they should not have any surface functional group that chelate metals such as Cu(II) and Fe(III); they should not be common chelators of metal ions and they should be insensitive to nitrating agents. When analyzing carbon dot-based sensors for heavy metal sensing, it was found that coordination and chelation are common strategies used [7]. According to the hard and soft acid and bases principle, transitional metals including Fe(II), Co(II), Ni(II), Cu(II), Zn(II), and Pb(II) trend toward binding borderline ligands like $-CO-NH-$, $>N=H$, $-C_6H_4NH_2$ and hard heavy metals of Mg(II), Sr(II), Mn(II), Al(III), Cr(III), Fe(III), U(II) have priority to bind with coordinating groups of $-OH$, $-F$, $-Cl$, $-PO_4^{3-}$, $-OOCR$, $-OR$, $-NH_2$, $-SO_3H$, $>PO_4$, and $-NH_2R$ [8]. Based on this, when choosing the functional groups of CDs, they should not have any of the above groups and should perhaps have an hydrophobic terminal group and alkyl chains. This will prevent any interaction with heavy metals such as Cu(II) and Fe(III).

In addition to using CDs as indicators, the role of CDs as catalysts of nitration can be investigated. CDs are unique in their ability to catalyze various chemical reactions. Specifically, the CDs used in this work were able to catalyze the transesterification of canola oil to biodiesel [7]. The biodiesel conversions were high ($\geq 97\%$ at 150 °C) with 1 wt% catalyst loading [7]. Other CDs have been used to catalyze water-splitting, aldehyde–alcohol condensation reaction, and CO_2 reduction. Selectively synthesizing CDs that are able to catalyze nitration of Tyr would be useful. The CDs, synthesized from citric acid through the hydrothermal method and doped with cobalt

and nitrogen, could be used for Tyr nitration due to their catalytic property of accelerating the decomposition of H_2O_2 and to increase the number of hydroxyl radicals [10]. This allowed nTyr to inhibit CDs through an electric transfer process and resulted in a decline in CL intensity [10]. This system can be used both as a sensor for nTyr formation and a catalyst of nitration.

In conclusion, CDs serve as valuable tools for detecting amino acids. This thesis investigated the different roles of CDs as sensors of Tyr and its analogues, as end-point and real time indicators of Tyr nitration. Further research should be carried out in order to optimize the ability of CDs to be used in point-of care testing.

4.3 References

[1] X. Liao, X., Chen, C., Wang, P., Zhou, R., Zhao, X., Fan, H., & Huang, Z. (2022). Carbon dots derived from cellobiose for temperature and phosalone detection. *Materials Research Bulletin*, *151*, 111790.
[2] Wang, R., Xu, Y., Zhang, T., & Jiang, Y. (2015). Rapid and sensitive detection of Salmonella typhimurium using aptamer-conjugated carbon dots as fluorescence probe. *Analytical Methods*, *7*(5), 1701-1706.
[3] Zu, F., Yan, F., Bai, Z., Xu, J., Wang, Y., Huang, Y., & Zhou, X. (2017). The quenching of the fluorescence of carbon dots: a review on mechanisms and applications. *Microchimica Acta*, *184*(7), 1899-1914.
[4] Cheng, X., Cen, Y., Xu, G., Wei, F., Shi, M., Xu, X., ... & Hu, Q. (2018). Aptamer based fluorometric determination of ATP by exploiting the FRET between carbon dots and graphene oxide. *Microchimica Acta*, *185*(2), 1-8.
[5] Zhu, Z., Liu, C., Song, X. M., Mao, Q., & Ma, T. (2021). Carbon dots as an indicator of acid–base titration and a fluorescent probe for endoplasm reticulum imaging. *ACS Applied Bio Materials*, *4*(4), 3623-3629.
[6] Yan, F., Jiang, Y., Sun, X., Bai, Z., Zhang, Y., & Zhou, X. (2018). Surface modification and chemical functionalization of carbon dots: a review. *Microchimica Acta*, *185*(9), 1-34.
[7] Li, P., & Li, S. F. (2021). Recent advances in fluorescence probes based on carbon dots for sensing and speciation of heavy metals. *Nanophotonics*, *10*(2), 877-908.
[8] Bjørklund, G., Crisponi, G., Nurchi, V. M., Cappai, R., Buha Djordjevic, A., & Aaseth, J. (2019). A review on coordination properties of thiol-containing chelating agents towards mercury, cadmium, and lead. *Molecules*, *24*(18), 3247.

[9] Macina, A., de Medeiros, T. V., & Naccache, R. (2019). A carbon dot-catalyzed transesterification reaction for the production of biodiesel. *Journal of Materials Chemistry A*, *7*(41), 23794-23802.

[10] Delnavaz, E., & Amjadi, M. (2021). A chemiluminescence probe enhanced by cobalt and nitrogen-doped carbon dots for the determination of a nitrosative stress biomarker. *Microchimica Acta*, *188*(8), 1-8.

Appendices

Appendix A – Chapter 2 – Supplementary Information (SI) from manuscript

Materials and Methods

Chemicals and reagents

L-tyrosine was purchased from Sigma Aldrich. O-phospho-L-tyrosine was purchased from TCI America. 3-nitro-L-tyrosine, 98%, was purchased from Alfa Aesar. 2-(N-morpholino)ethanesulfonic acid (MES) hydrate was purchased from Fisher BioReagents. Sodium chloride (NaCl) and calcium chloride dihydrate were purchased from BioShop. Ethylenediamine tetraacetic acid (EDTA) free acid, ferrous sulfate, and manganese chloride were purchased from Caledon Laboratories Chemicals. Formamide ($\geq$99.5%) and reduced L-glutathione ($\geq$98.0%) were purchased from Thermo Scientific. Sodium hydroxide (NaOH) was purchased from Caledon Laboratories Chemicals. Acetone and ethanol were purchased from Fischer Scientific. Iron (III) perchlorate was obtained from Alfa Aesar. Adenosine, 99%, was purchased from Fisher Scientific. Potassium chloride was purchased from EMD Millipore. Zinc chloride, anhydrous, 98+% was purchased from Alfa Aesar. Potassium phosphate, monobasic was purchased from MP Biomedicals, LLC. HyClone Donor equine serum was kindly provided by Dr. Janet Yee (Trent University, (Cytiva, Cat# SH30074.03)). Ammonium sulfate was purchased from Amresco. L-ascorbic acid was purchased from BDH (USA). Glucose was purchased from Nicoya. L-histidine was purchased from Acros Organics. Glycine was purchased from invitrogen. Thymidine, 99+% and Uridine, 99% were purchased from Fischer Scientific. Cytidine was purchased from TCI America. BSA (bovine serum albumin), $\geq$ 96%, pH 5.2 and heparin sodium salt from porcine intestinal mucosa were purchased from Sigma Aldrich. Artificial saliva was purchased from Pickering Laboratories. Acetonitrile (ACN) was purchased from Honeywell Riedel-de-Haën™

and tetrabutylammonium hexafluorophosphate (TBAF) was purchased from TCI America. All electrodes were purchased from CHInstruments (USA).

Stern-Volmer plot

The Stern-Volmer analysis was conducted to understand the rate at which a substance can quench the excited state of a fluorophore [1]. The fluorescence emission data may be analyzed according to the Stern–Volmer quenching Eq. S1-S3:

$I_o/I = 1 + K_S[Q]$ (Eq. S1) for static quenching

$I_o/I = \tau_o/\tau = 1 + K_D[Q]$ (Eq. S2) for dynamic quenching

$I_o/I = 1 + (K_S + K_D)[Q] + K_SK_D[Q]^2$ (Eq. S3) for both static and dynamic quenching

$$\frac{I_0}{I} = e^{K[Q]}$$ (Eq. S4)

where I_o and I are the steady state fluorescence emission intensities of CDs at 679 nm (the excitation wavelength of 420 nm) before and after the addition of quencher, nTyr, and K_D is a product of $\tau_o kq$, where τ_o is the lifetime in the absence of Q, and the kq is the quenching rate constant. The Eq S4 corresponds to a completely static quenching mechanism.

The LOD value was calculated based on the following equation = average of a blank+3* standard deviation of a blank. The value of y was used in the linear regression plot to solve for x (concentration of LOD). The LOQ value was calculated based on the following equation = average of a blank+10* standard deviation of a blank. The value of y was used in the linear regression plot to solve for x (concentration of LOQ).

Benesi-Hilderbrand plot

The value of the binding constant, K_b, was calculated from the Benesi-Hildebrand plot of $\log(I_o - I/I)$ versus $\log[nTyr]$, based on the Eq. S4, which assumes the static quenching (Figure S6) [2-3]:

$\log[(I_o - I)/I] = \log K_b + N\log[nTyr]$ (Eq. S4)

wherein, I_o and I are fluorescence intensities of CDs at 679 nm in the absence and presence of nTyr; K_b is the binding constant; [nTyr] is the concentration of nTyr, and N is the number of binding sites for the CDs.

Experimental determination of HOMO and LUMO levels

The HOMO and LUMO energy levels of CDs were calculated as previously reported, by using Eq. S5 - S7, wherein E_{red} corresponds to the onset reduction potential of -0.93 V; however, the HOMO could not be calculated from the CV, due to the irreversible nature of oxidation of CDs [4]. Hence, to determine HOMO level, the optical energy band gap, E_g, was calculated from the longest absorbance onset of 460 nm from the UV-vis spectrum of CDs, to be 2.69 eV. The λ_{onset} corresponds to the onset of the longest absorbance wavelength and was used to calculate the optical band gap energy and LUMO level [5,6]. Using the energy gap, the HOMO was calculated to be -6.15 eV. From the onset of the E_{red} at -0.93 V, the LUMO was calculated to be -3.46 eV. When the longest absorbance edge at 679 nm was used to determine the E_g and HOMO, it was found that E_g was 1.75 eV and HOMO was -5.21 eV.

$E_g = hc/\lambda_{onset}$ (Eq. S5)

$E_{LUMO} = -e[E_{red} + 4.4]$ (Eq. S6)

$E_{LUMO} = E_{HOMO} + E_g$ (Eq. S7)
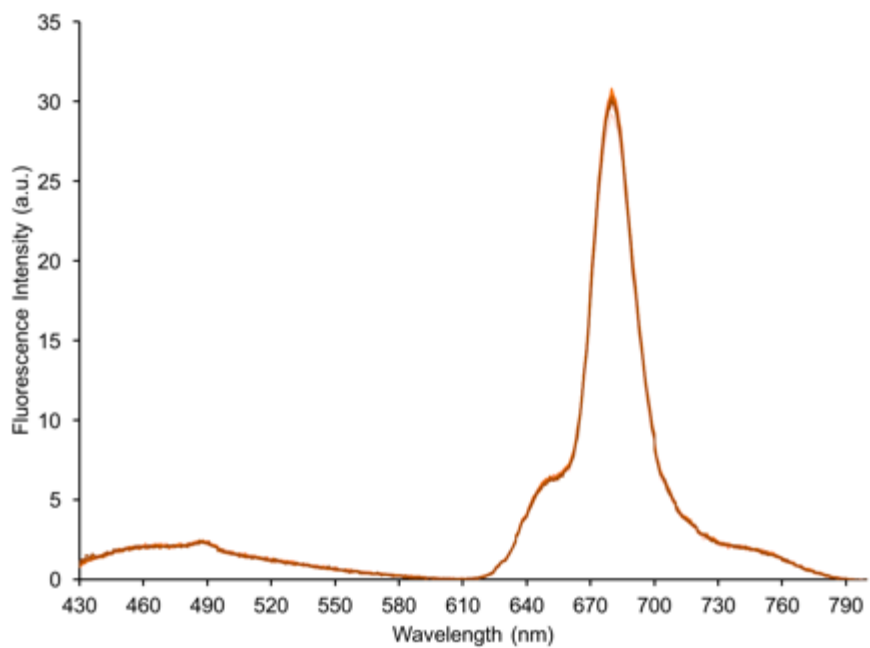
Figure S1. The fluorescence emission spectra of CDs collected at time intervals between t = 0 and 1h ([CDs] = 0.0033 mg/mL; MES Buffer, pH 6.8).
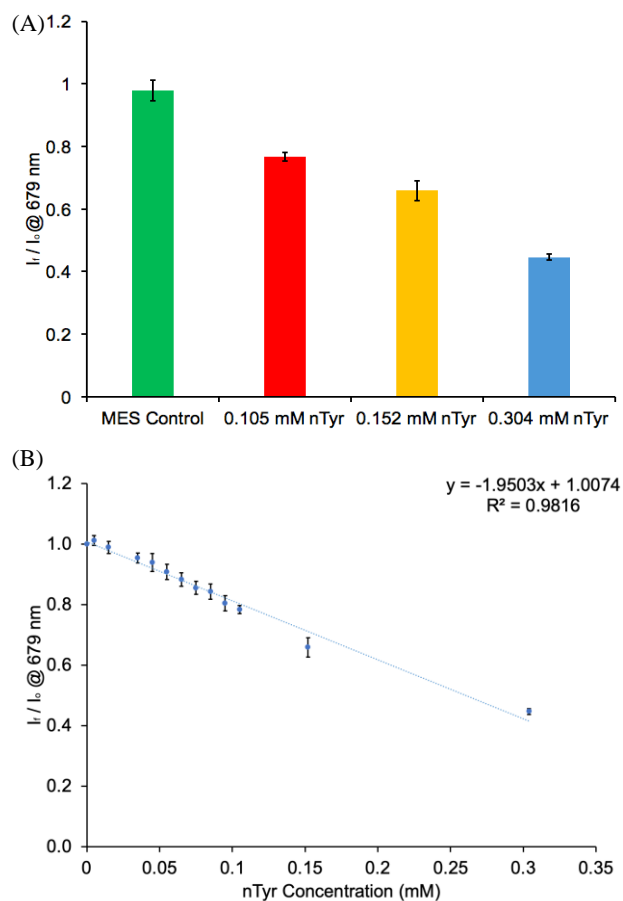
Figure S2. (A) The average of I_f/I_o at emission peak at 679 nm of CDs at different nTyr concentrations ([CDs] = 0.0033 mg/mL; [nTyr] = 0.105, 0.152, 0.304 mM; MES buffer pH 6.8); (B) Plot of I_f/I_o at emission peak at 679 nm of CDs as a function of nTyr concentration ([CDs] = 0.0033 mg/mL, MES buffer pH 6.8).
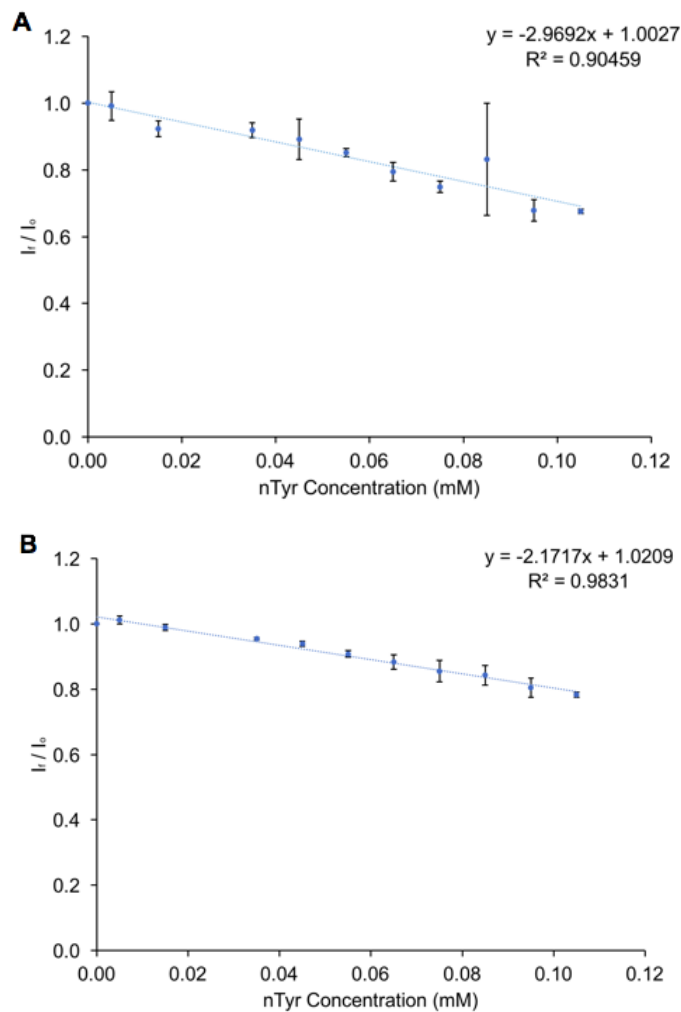
Figure S3: The I_f/I_o at (A) 480 nm and (B) 650 nm of CD as a function of nTyr concentration (data taken from Figure 2C) ([CDs] = 0.0033 mg/mL; [nTyr] = 0 - 0.105 mM; MES Buffer, pH 6.8).
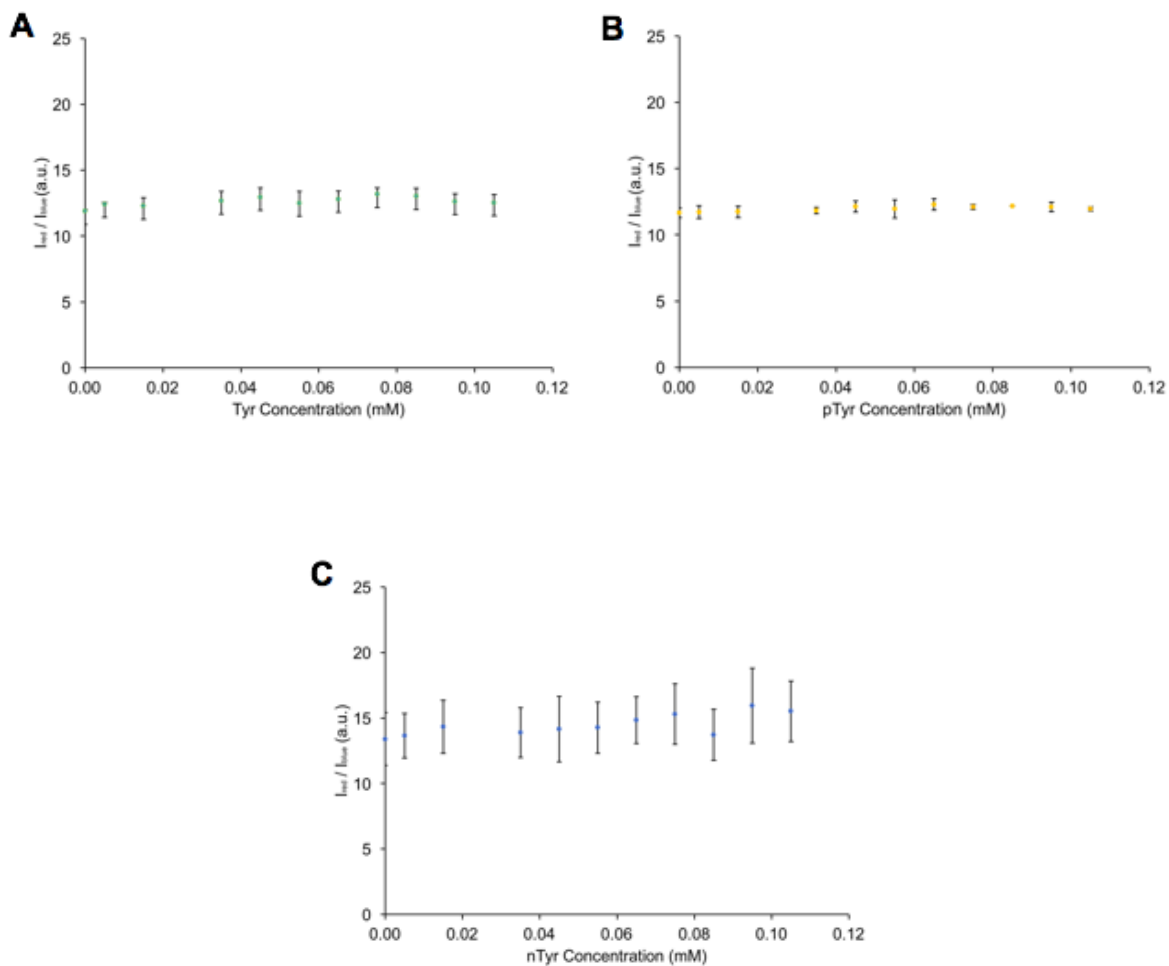
Figure S4: The I_{red}/I_{blue} for (A) Tyr and (B) pTyr (error bars represent duplicate measurements), (C) nTyr titrations ([CDs] = 0.0033 mg/mL; [amino acid] = 0 - 0.105 mM; MES Buffer, pH 6.8).
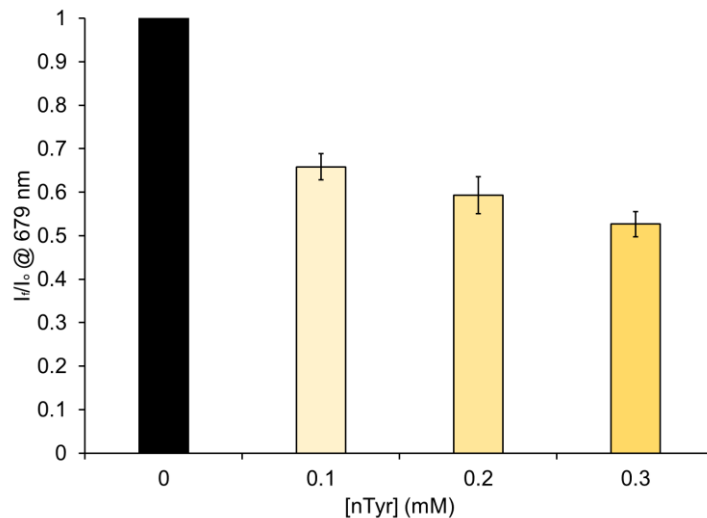
Figure S5: The average of I_f/I_o at emission peak at 679 nm of CDs with nTyr in undiluted artificial saliva ([CDs] = 0.0033 mg/mL).
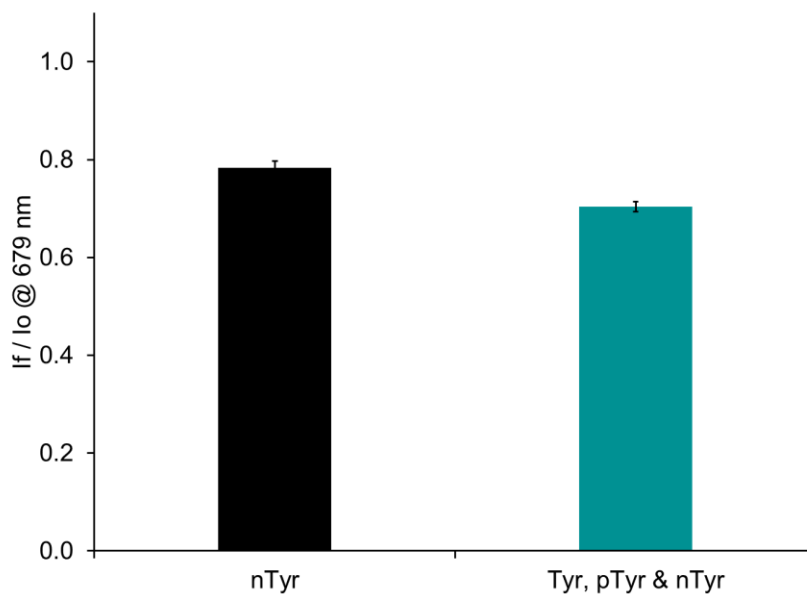
Figure S6: The average of I_f/I_o at emission peak at 679 nm of CDs with equimolar mixture of Tyr, pTyr and nTyr ([CDs] = 0.0033 mg/mL; [nTyr] = [Tyr] = [pTyr] = 0.105 mM).
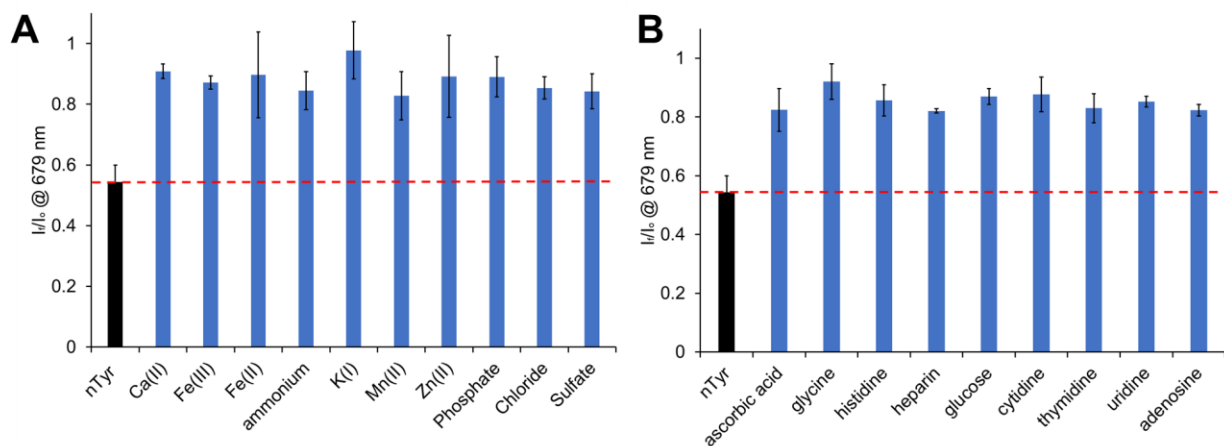
Figure S7: The average of I_f/I_o at emission peak at 679 nm of CDs with nTyr compared to CDs in the presence of various common biological interference (A) cations and anions, and (B) amino acids, nucleosides and other organics ([CDs] = 0.0033 mg/mL; [nTyr] = 0.3 mM; see Table S3 for concentration of various interferents).
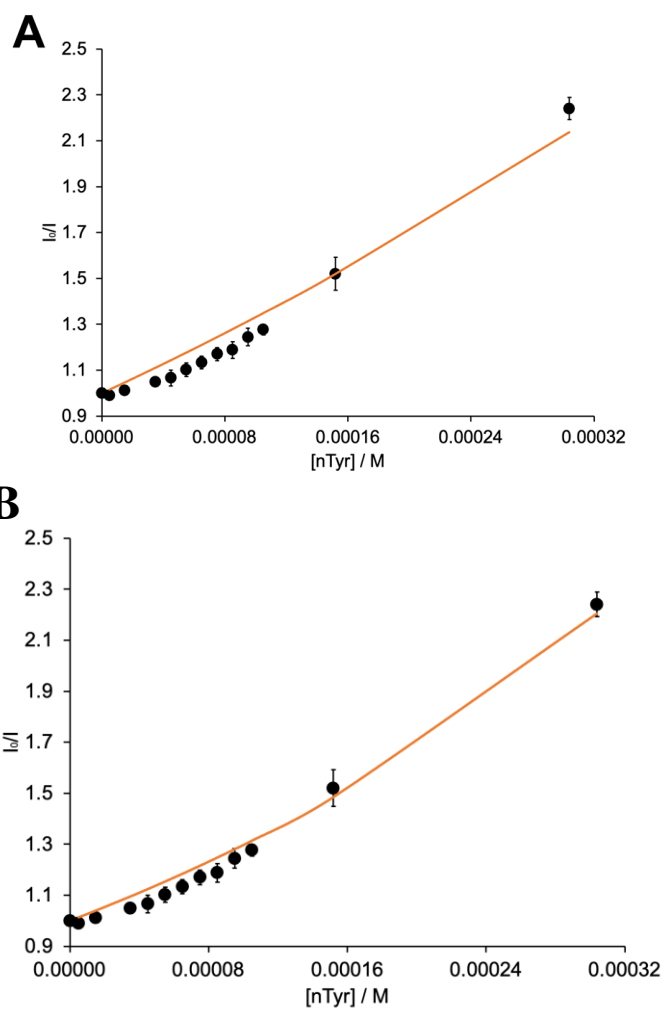
Figure S8. Stern-Volmer plots of CDs as a function of nTyr concentrations (A) experimental data fitted using Eq. S3 (assuming static and dynamic quenching), and (B) experimental data fitted to Eq. S4 (assuming purely static quenching) (emission intensity at 679 nm; [CD] = 0.0033 mg/mL; [nTyr] = 0 - 0.000305 M; MES Buffer, pH 6.8).
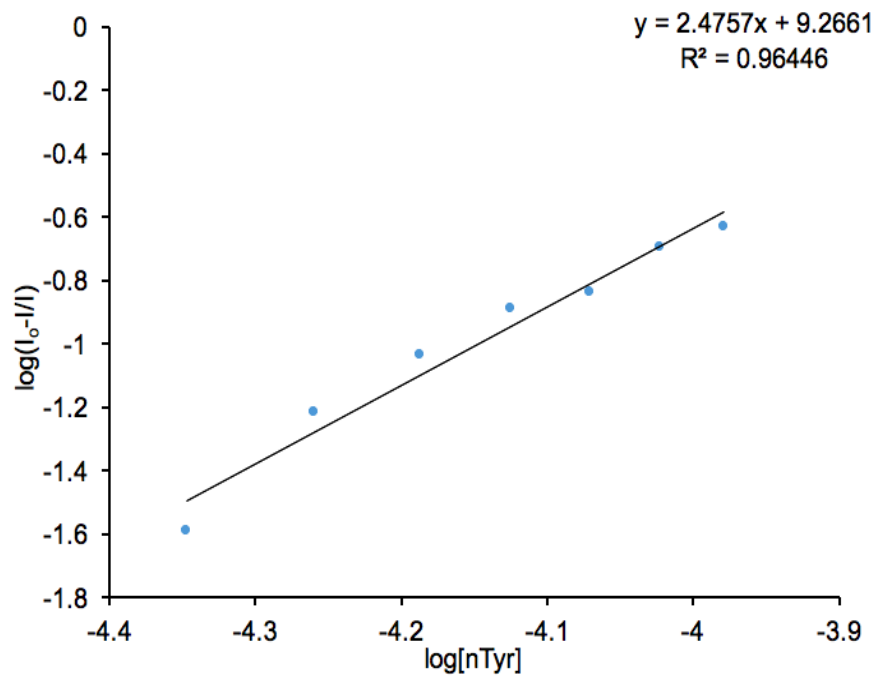
Figure S9. Benesi-Hildebrand plot of CDs as a function of nTyr concentration (emission intensity at 679 nm, [CD] = 0.0033 mg/mL; [nTyr] = 0 - 0.000105 M; MES Buffer, pH 6.8).
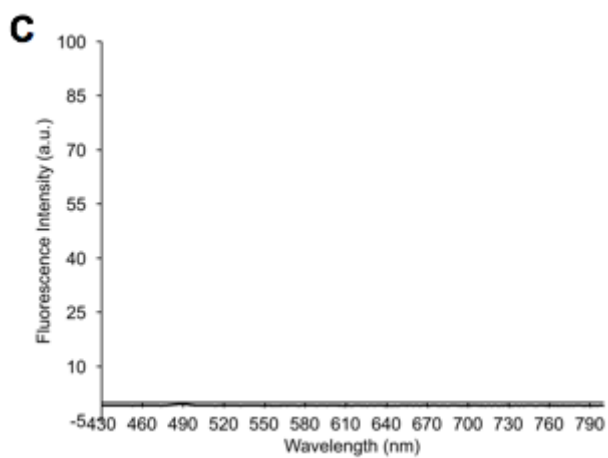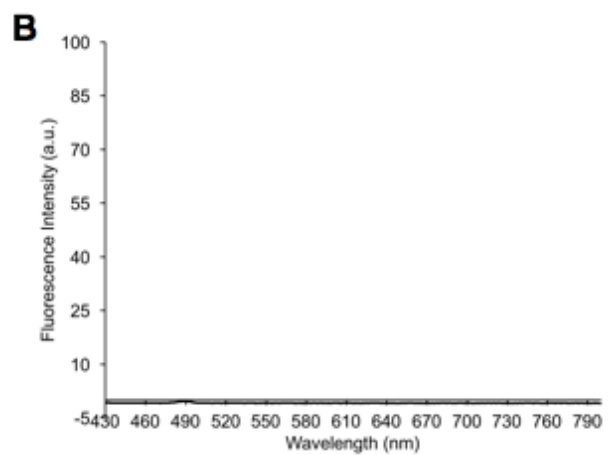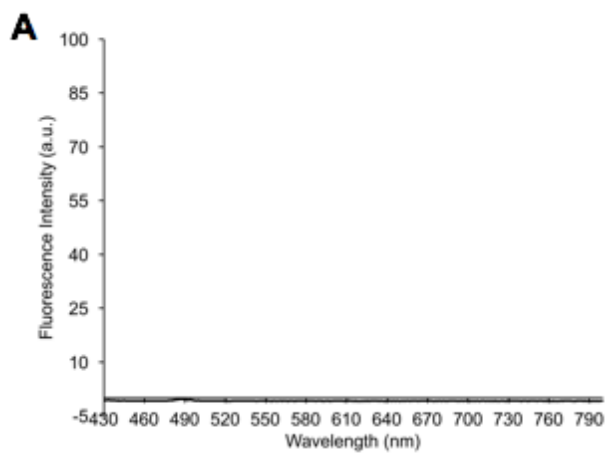
Figure S10: The fluorescence emission spectra of (A) Tyr and (B) pTyr, (C) nTyr ([amino acid] = 0.105 mM; MES Buffer, pH 6.8; excitation wavelength = 420 nm).
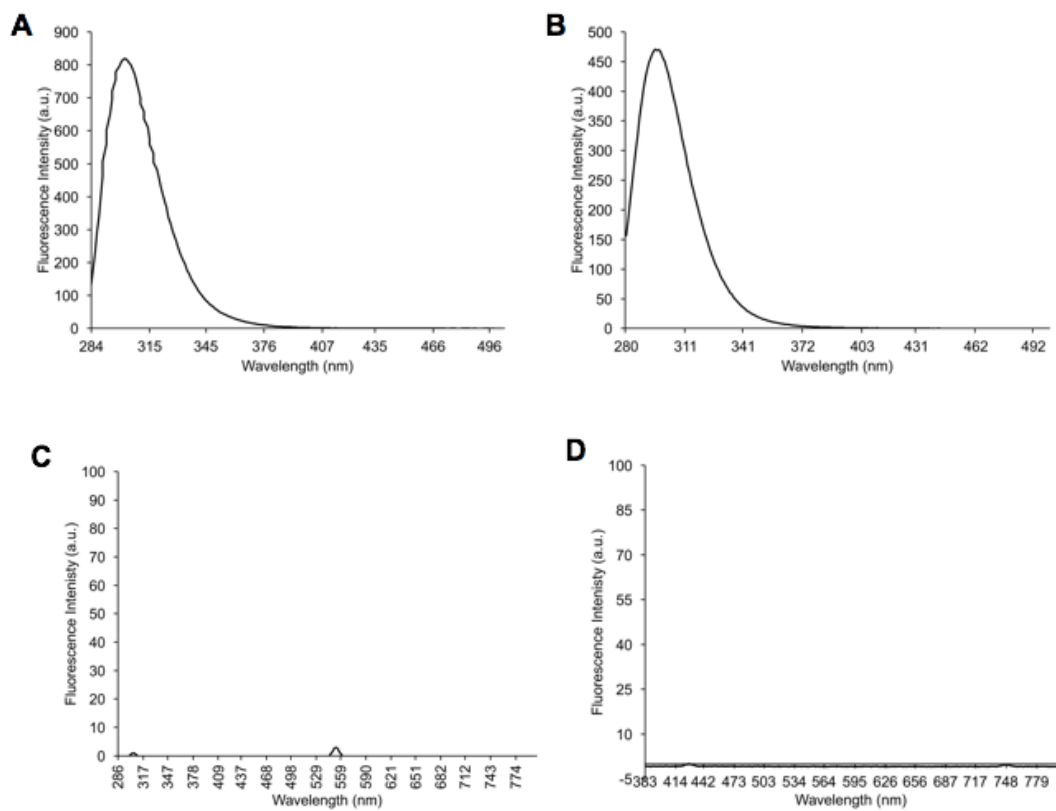
Figure S11: The fluorescence emission spectra of (A) Tyr (λ_{ex} = 274 nm), (B) pTyr (λ_{ex} = 271 nm), (C) nTyr (λ_{ex} = 277 nm) and (D) nTyr (λ_{ex} = 374 nm) ([amino acid] = 0.105 mM; MES Buffer, pH 6.8).
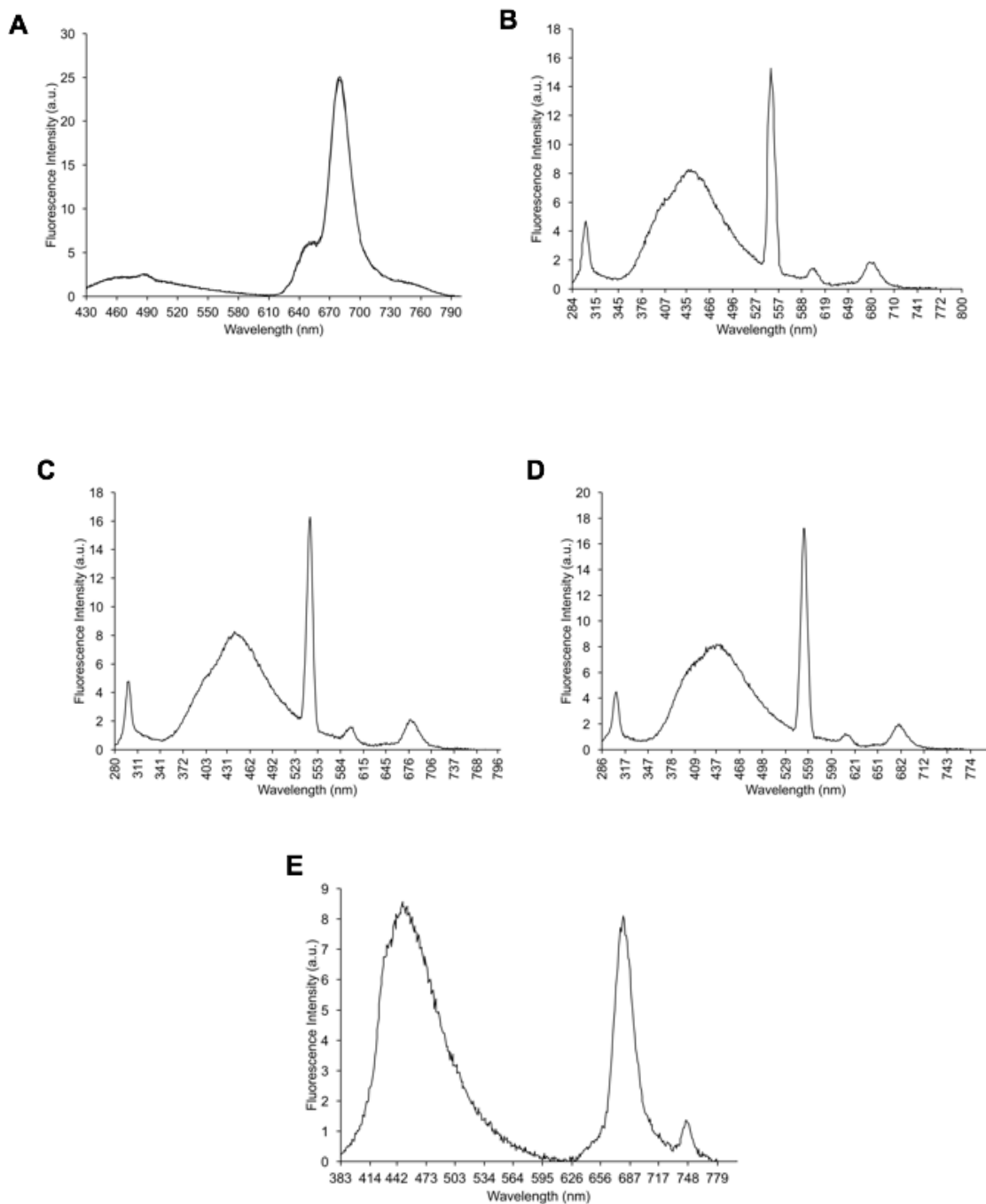
Figure S12: The fluorescence emission spectra of CDs (A) λ_{ex} = 420 nm, (B) λ_{ex} = 274 nm, (C) λ_{ex} = 271 nm, (D) λ_{ex} = 277 nm and (E) λ_{ex} = 374 nm ([CDs] = 0.0033 mg/mL; MES Buffer, pH 6.8).
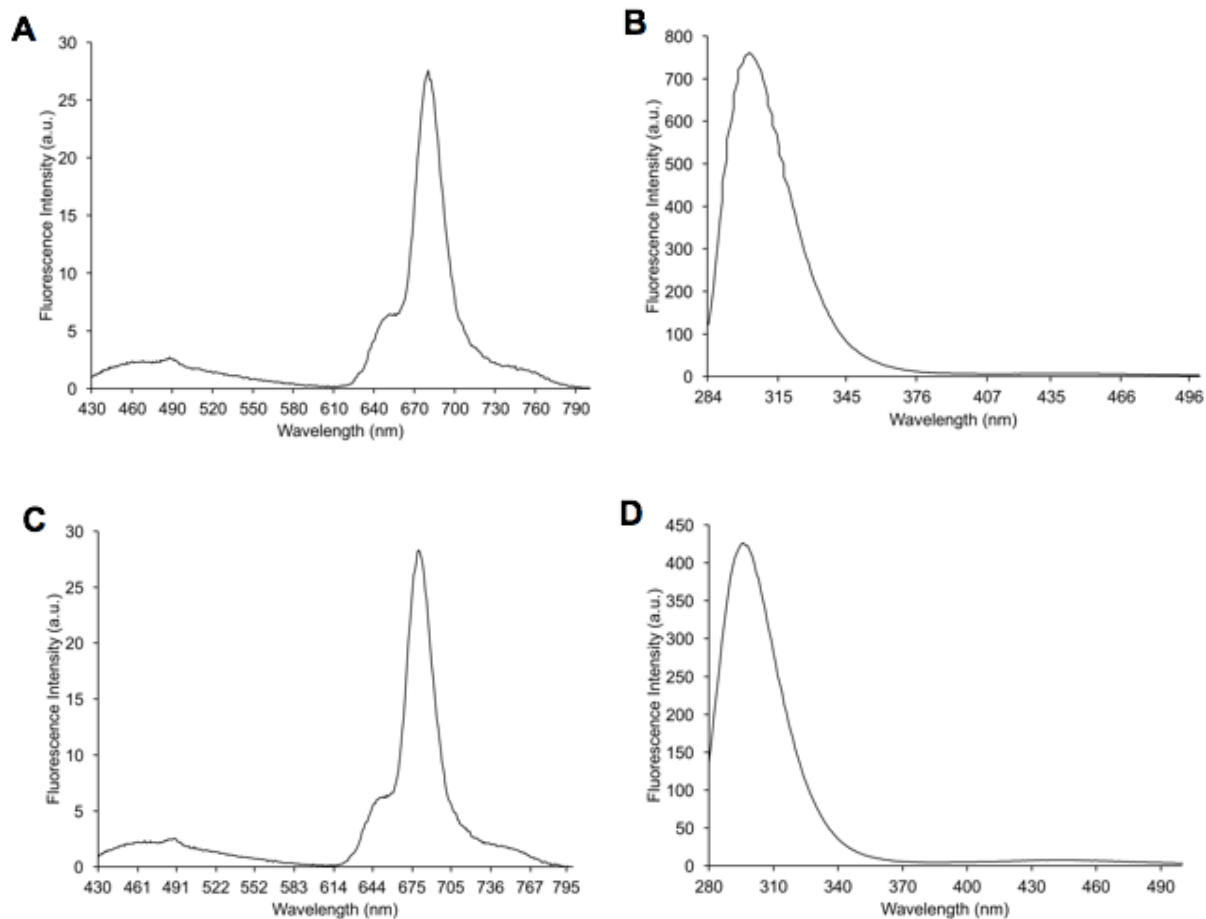
Figure S13: The fluorescence emission spectra of Tyr/CD (A) λ_{ex} = 420 nm, (B) λ_{ex} = 274 nm and pTyr/CD systems, (C) λ_{ex} = 420 nm, (D) λ_{ex} = 271 nm ([CDs] = 0.0033 mg/mL; [amino acid] = 0.105 mM; MES Buffer, pH 6.8).
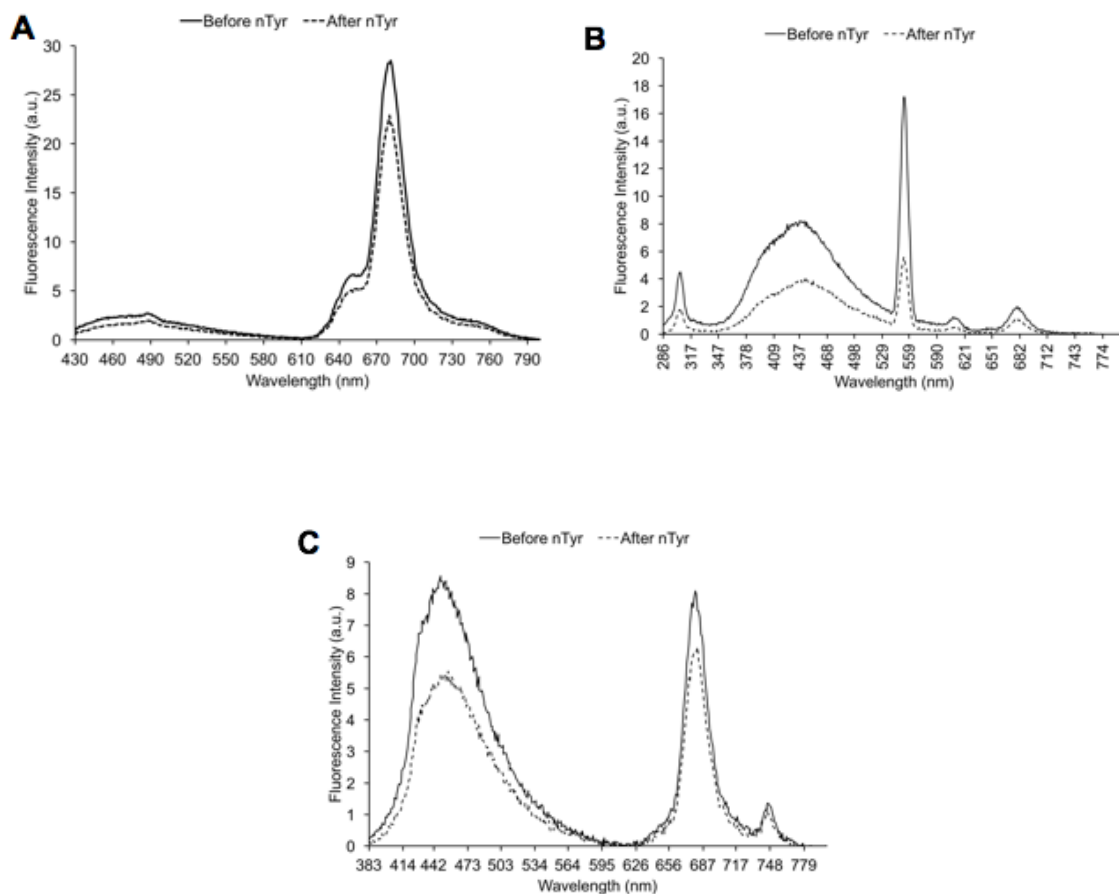
Figure S14: The fluorescence emission spectra of CDs before and after nTyr (A) λ_{ex} = 420 nm, (B) λ_{ex} = 277 nm and (C) λ_{ex} = 374 nm ([CDs] = 0.0033 mg/mL; [amino acid] = 0.105 mM; MES Buffer, pH 6.8).
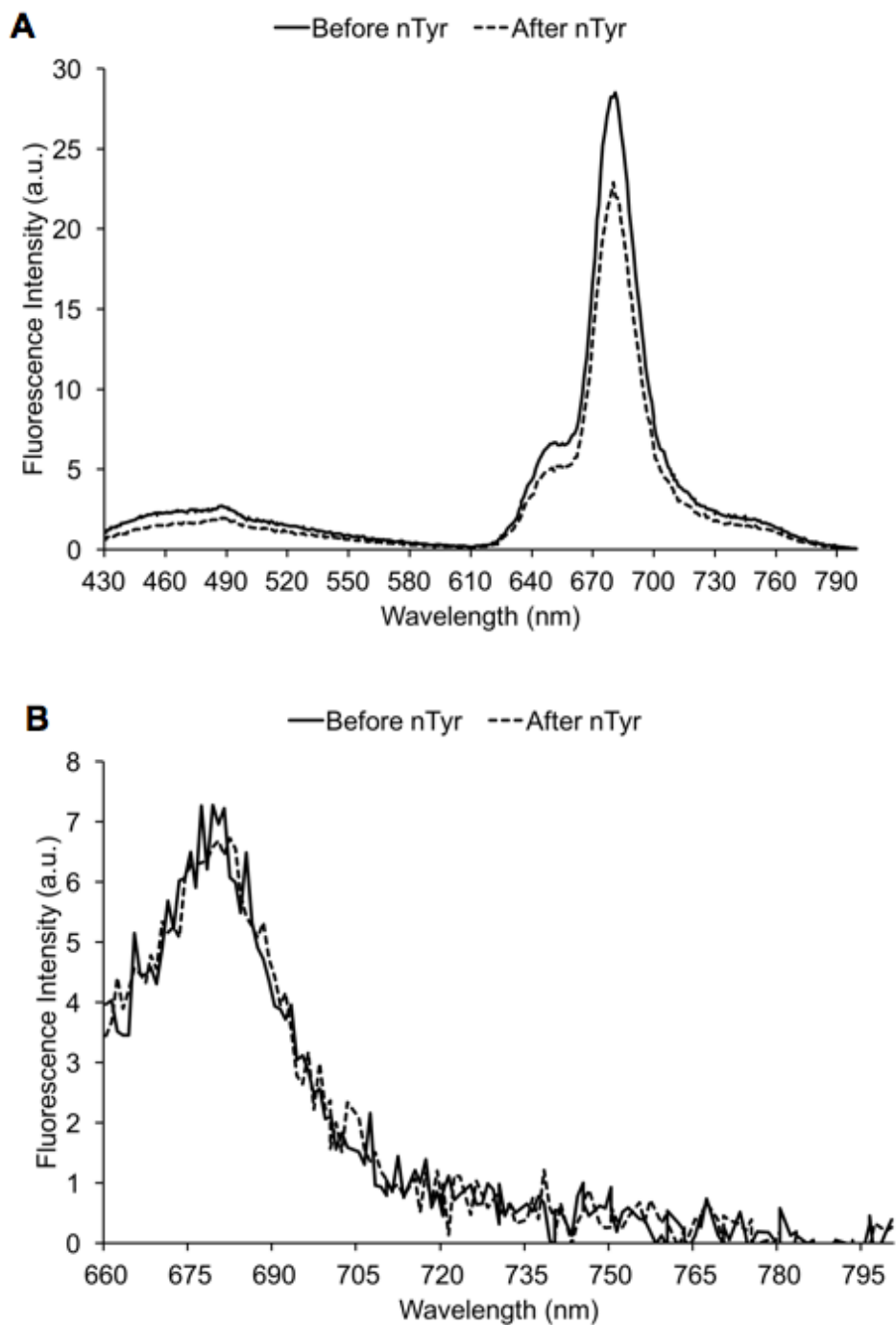
Figure S15: The fluorescence emission spectra of CDs before and after nTyr (A) λ_{ex} = 420 nm and (B) λ_{ex} = 650 nm, (([CDs] = 0.0033 mg/mL; [amino acid] = 0.105 mM; MES Buffer, pH 6.8).
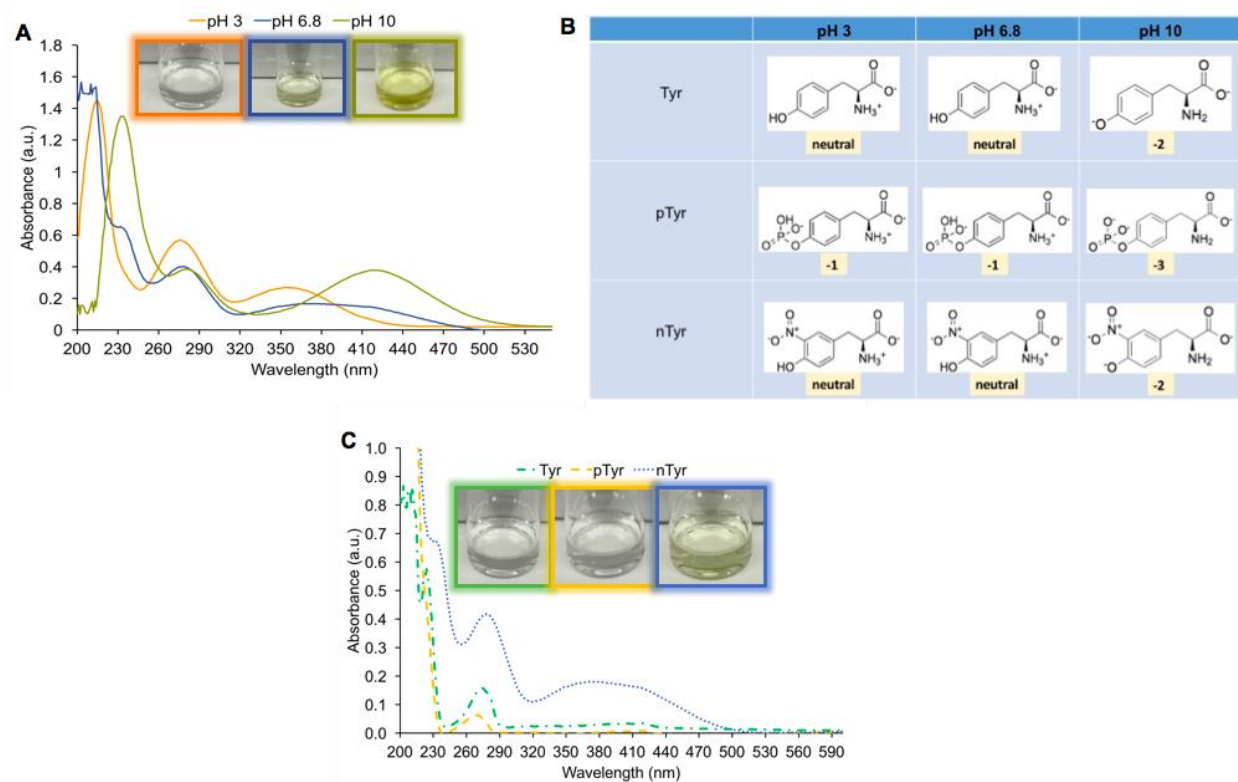
Figure S16. (A) UV-vis spectra of CDs at various pH solutions (pH 3, 6.8 and 10) after the addition of nTyr, (B) Structures of amino acids (Tyr, pTyr, and nTyr) at different pH values (pH 3, 6.8 and 10); (C) UV-vis spectra of CDs with Tyr, pTyr, and nTyr ([CDs] = 0.0033 mg/mL; [amino acid] = 0.105 mM; MES Buffer, pH 6.8).
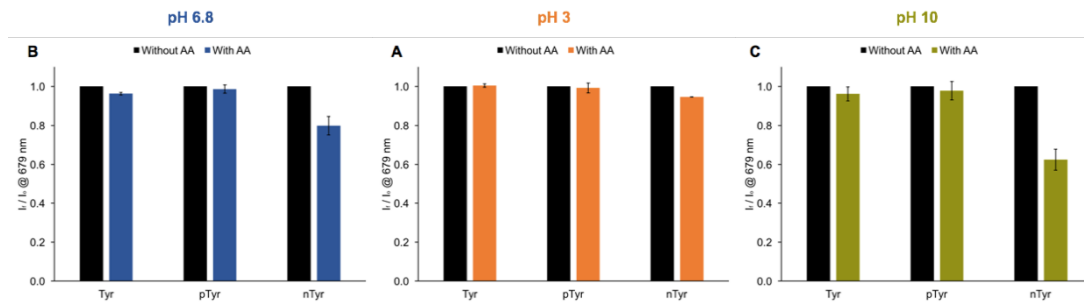
Figure S17. Average of I_f/I_o at 679 nm of samples in MES Buffer ([CDs] = 0.0033 mg/mL; [amino acid] = 0.105 mM).
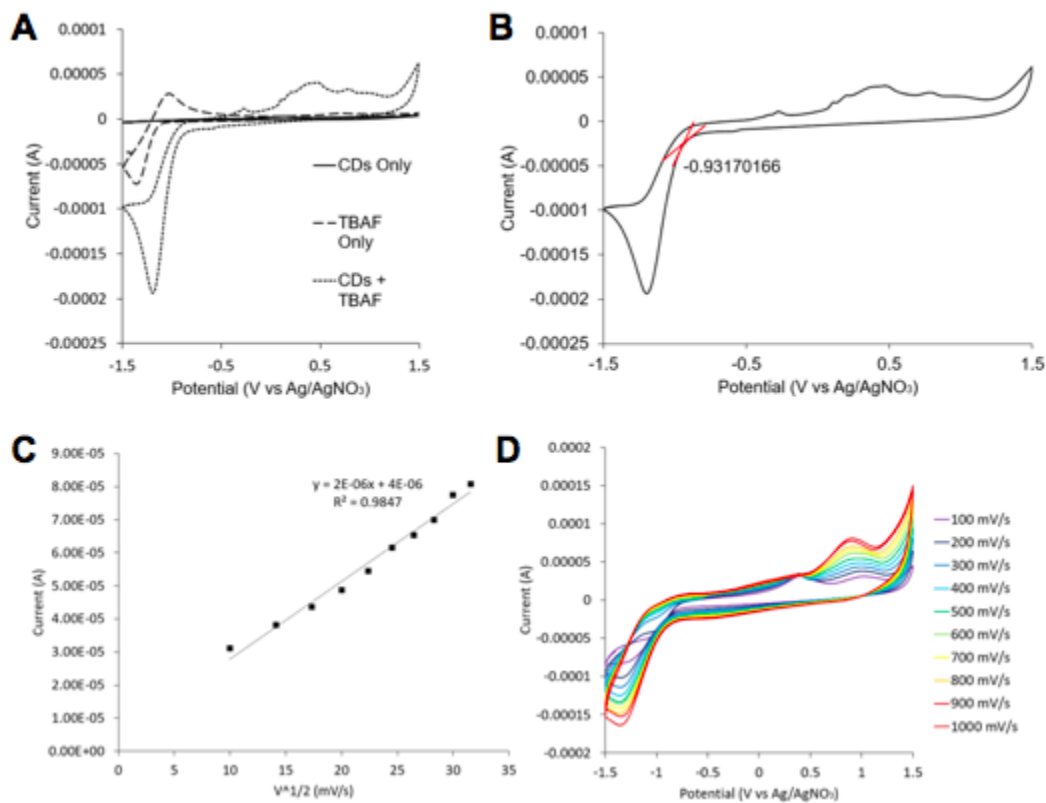
Figure S18: (A) Cyclic voltammogram of CDs only, TBAF only and CDs/TBAF (GCE as working electrode; Ag/AgNO$_3$ reference electrode; 0.1 M tetrabutylammonium fluoride (TBAF) as the electrolyte; [CD] = 0.0033 mg/mL; acetonitrile). (B) Single scan of CDs with TBAF with onset of reduction potential (E_{Red}). (C) Randles-Sevcik plot of the square root of scan rate. (D) Scan rate dependent analysis of CDs from 100 - 1000 mV/s.
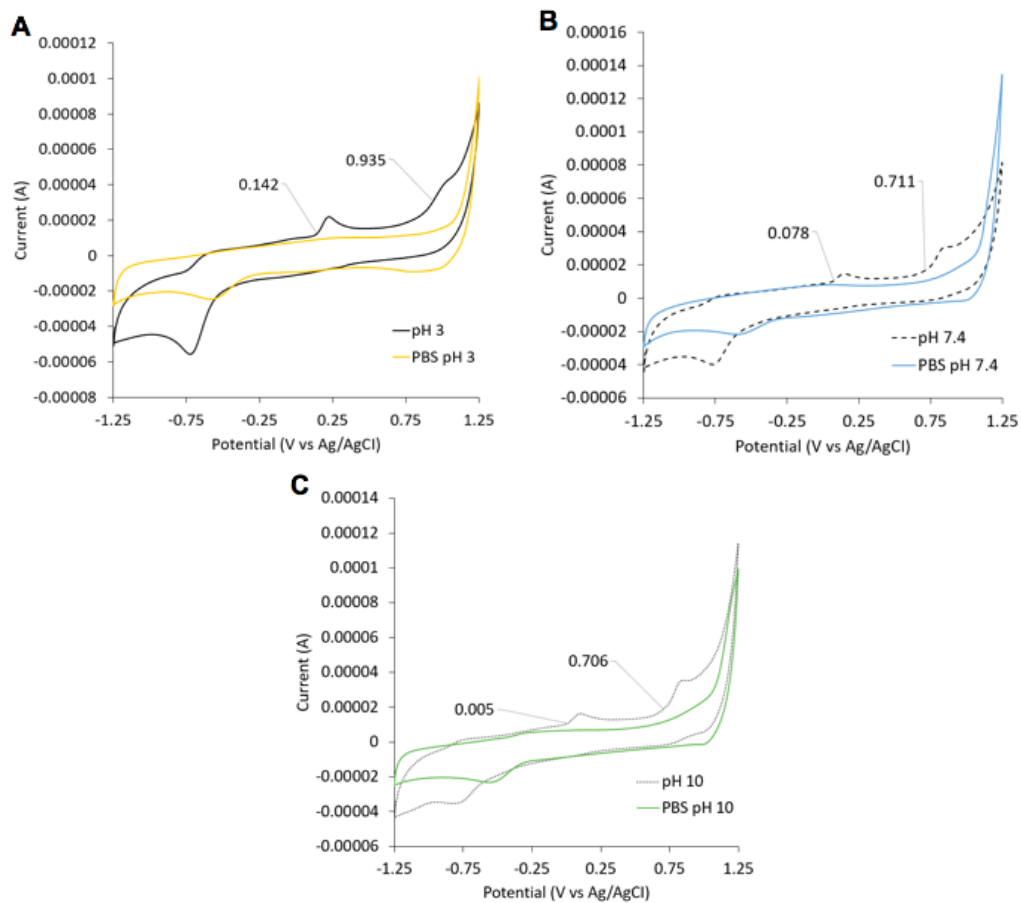
Figure S19: Cyclic voltammograms of nTyr solution at (A) pH 3 (B) pH 7.4, (C) pH 10 (GCE as working electrode; Ag/AgNO$_3$ reference electrode; PBS buffer was used as a control at each specific pH value tested [nTyr] = 1 mM).

Table S1: Selectivity studies for detection of nTyr in the presence of various interfering substances tested [7,8].

Coexisting concentrations (10^{-6} M)	Coexisting substances
0.5	adenosine, thymidine
0.6	cytidine
3.31	sulfate
5.20	uridine
5.30	Fe(III)
6.62	histidine, glycine
13.2	Fe(II), ammonium
33.1	Ca(II)
39.7	Chloride
53.0	phosphate
66.2	K(I), Mn(II), Zn(II)
7,929.6	glucose
10,000	ascorbic acid
337,012	glucose

Table S2. Fluorescence lifetimes of CDs after addition of amino acids ([CDs] = 0.0033 mg/mL; [amino acid] = 0.105 mM; in MES Buffer, pH 6.8).

Amino acid with CDs	Lifetime 1 (ns)	±	Lifetime 2 (ns)	±
MES Buffer, pH 6.8	0.57	0.21	3.72	0.57
Tyr	0.42	0.30	4.85	2.33
pTyr	0.53	0.51	4.41	1.57
nTyr	0.35	0.30	3.05	0.10

Table S3. Zeta potentials of CDs after addition of amino acids ([CDs] = 0.0033 mg/mL; [amino acid] = 0.105 mM; in MES Buffer, pH 6.8).

CDs	Zeta Potential (mV)	±
No amino acid	-26.0	5.87
+Tyr	-24.2	3.79
+pTyr	-25.4	0.54
+nTyr	-22.4	5.23

Table S4: An overview on recently reported nanomaterial-based spectroscopic methods for the determination of nTyr (free amino acid).

Method Used	Material	Linear range	Limit of Detection	Reference (from main manuscript)
Fluorescence spectroscopy	bio-inspired molecularly imprinted polymer as a receptor and green emitting carbon dots (CDs) as a signal transducer	0.050–1.85 μM	17 nM	[29]
Fluorescence spectroscopy	hybrid material (AuNCs@ZIF-8) synthesized by encapsulating gold nanoclusters (AuNCs) into the zeolitic imidazolate framework (ZIF-8)	5−200 nM	1.8 nM	[15]
Fluorescence spectroscopy	binuclear Pt-2-pyrazinecarboxylic acid (pca)-Bipyridine (bpy) complex doped in sol-gel matrix	0.795-18500 nM	0.47 nM	[16]
Fluorescence spectroscopy	Carbon dots synthesized from glutathione and formamide	20-105 μM	34 μM	Current work

References

1. K.P. Kuijpers, C. Bottecchia, D. Cambié, K. Drummen, N.J. König, T. Noël, A Fully Automated Continuous-Flow Platform for Fluorescence Quenching Studies and Stern–Volmer Analysis, Angew. Chem. Int. Ed. 57 (2018) 11278-11282.

2. R. Dwivedi, D.P. Singh, B.S. Chauhan, S. Srikrishna, A.K. Panday, L.H. Choudhury, V.P. Singh, Intracellular application and logic gate behavior of a 'turn off-on-off' type probe for selective detection of Al3+ and F− ions in pure aqueous medium, Sens. Actuators B-Chem. 258 (2018) 881-894.

3. U.P. Raghavendra, M. Basanagouda, A.H. Sidrai, J. Thipperudrappa, Spectroscopic investigations on the interaction of biologically active 4-aryloxymethyl coumarins with TiO2 nanoparticles, J. Mol. Liq. 222 (2016) 601-608.

4. B. Ju, Y. Wang, Y.M. Zhang, T. Zhang, Z. Liu, M. Li, S. Xiao-An Zhang, Photostable and low-toxic yellow-green carbon dots for highly selective detection of explosive 2,4,6-TRINITROPHENOL based on the dual electron transfer mechanism, ACS Appl. Mater. Inter. 10 (2018) 13040–13047.

5. Y. Li, N. Cai, M. Wang, W. Na, F. Shi, X. Su, Fluorometric detection of tyrosine and cysteine using graphene quantum dots, RSC Adv. 6 (2016) 33197-33204.

6. P.I. Djurovich, E.I. Mayo, S.R. Forrest, M.E. Thompson, Measurement of the lowest unoccupied molecular orbital energies of molecular organic semiconductors, Org. Electron. 10 (2009) 515–520.

7. S. Pang, Y. Zhang, C. Wu, C., S. Feng, Fluorescent carbon dots sensor for highly sensitive detection of guanine. Sens. Actuators B-Chem. 222 (2016) 857-863.

8. T.W. Traut, Physiological concentrations of purines and pyrimidines. Mol. Cell.

Biochem. 140 (1994) 1-22.

Appendix B – Permission for Article to be used in Thesis